Proliferation of Twinning in Metals: Application to Magnesium Alloys

Thesis by
Dingyi Sun

In Partial Fulfillment of the Requirements for the
degree of
Doctor of Philosophy

CALIFORNIA INSTITUTE OF TECHNOLOGY
Pasadena, California

2018
Defended July 5, 2017

Dingyi Sun
ORCID: 0000-0003-2109-7123

For my parents, to whom I owe everything

ACKNOWLEDGEMENTS

First, I would like to thank Professor Kaushik Bhattacharya for immediately accepting me into his group and treating me like a family member throughout. Kaushik, I still remember the advice you gave me about a month after I had been accepted as a Ph.D. student to treat the graduate experience as a marathon rather than a sprint and to pace myself rather than burn out from research. Even though I *definitely* took that advice a bit too far and ended up producing much less research than I should have, I am immensely grateful for the infinite patience you had for me. It has been a sincere privilege to have been part of your group, and I appreciate all that you've taught me — how to approach certain tasks in research, how to run a group, and even all the little things about daily life outside of just work.

Equally, I would like to thank my co-advisor, Professor Michael Ortiz, for taking me under his wing. Michael, I still remember being absolutely terrified when we met for the first time at visit day and you brought out a binder with my application right in front of me. Over the years however, your endless words of encouragement and unparalleled research wisdom have been integral to my success, and I am deeply indebted to you for having given me the time to discuss research every week.

I would also like to thank Professor Guruswami Ravichandran for being the kindest individual I've met at Caltech and always lifting me up even on days when I felt down (especially after group meeting presentations when I thought things had gone south, I always appreciated how you'd be the first up to give me a pat on the back). Likewise, I would also like to thank Professor Mauricio Ponga for having carried me through my years here by always providing exciting new projects to consider, even after you'd finished your postdoctoral position here and had gone onto a faculty position, and for also agreeing to return to Caltech just to serve on my committee.

Likewise, I am deeply indebted to our wonderful department staff — especially Jenni Campbell and Lydia Suarez — for always keeping me on a schedule. I know the faculty always acknowledge that they wouldn't be able to get anything done without their assistants, but it's also definitely true for us students that we wouldn't be able to live without you!

I am grateful for the support provided by the National Defense Science and Engineering Graduate Fellowship for having funded the majority of my research at Caltech, which allowed me to pursue a variety of different project directions before finally

settling on what would eventually become my thesis project. Likewise, I would also like to acknowledge support from the MEDE program for funding the final years of my thesis project, along with providing interesting insights in our weekly Tuesday meetings, allowing me to see alternative approaches to research on magnesium.

Additionally, I would like to thank the past and present members of our joint Kaushik-Ravi group meetings for having interesting discussions on a weekly basis on Wednesdays. As I have been here eons, this list is quite long, but includes: Andrew Richards, Bharat Penmecha, Ha Giang, Xin (Cindy) Wang, Srivatsan Hulikal, Lincoln Collins, Chun-Jen (Ren) Hsueh, Paul Plucinsky, Paul Mazur, Jin Yang, Ying Shi Teh, Victoria (Tori) Lee, Jacob Notbohm, Victoria Stolyar-Richmond, Kristen John, Mike Rauls, Charles (Stan) Wojnar, Zach Sternberger, Matt Newman, Christian Kettenbeil, Louisa Avellar, Kimberley Mac Donald, Tomoyuki Oniyama, Gal Shmuel, M. Zubaer Hossain, Likun Tan, Aaron Stebner, Pierluigi Cesano, Owen Kingstedt, Dipankar Ghosh, Arzhang Angoshtari, Nikhil Karanjgaokar, Swarnava Ghosh, Noy Cohen, Stella Brach, and many others.

Furthermore, I would like to thank all the friends I made over the years for making this an incredible experience. To my roommate, Reid Kawamoto, thanks for putting up with my laziness for four of my five years here. To my "four-one" crew — Nick Dou, Ishan Tembhekar, Kevin Rosenberg, Sean Symon — come on boys. To my fellow "A-team" member Will Schill, thanks for carrying me through all those research meetings. To my SOPS co-pilot Natalie Higgins, thank you for taking care of all the heavy lifting; you know I couldn't have gotten anything done with SOPS if it weren't for you. To Betty Wong and Wei-Lin Tan, thank you for introducing me to a whole new world of culinary experiences, and on the flip side, thank you Tess Saxton-Fox for helping organize our group camping trips and for introducing me to the beauty of the Californian wilderness. To all the innumerable volleyball folks, thank you for giving me a reason to exercise. Of course, thank you as well to the other members of MCE *and* GALCIT who entered in 2012; the first two years — especially the very first term — were a tough time for me, and I'm grateful that you all were there for and with me on this adventure.

Finally, and most importantly, I am infinitely indebted to my parents Shouheng Sun and Chengyi Chang. Thank you for always supporting me and for keeping me going in the right direction even when the going was tough. I may have thanked all of these individuals before you, but know that none of this would have been possible in the first place if you had not been there for me throughout my entire life.

ABSTRACT

In the search for new alloys with a great strength-to-weight ratio, magnesium has emerged at the forefront. With a strength rivaling that of steel and aluminum alloys — materials which are deployed widely in real world applications today — but only a fraction of the density, magnesium holds great promise in a variety of next-generation applications. Unfortunately, the widespread adoption of magnesium is hindered by the fact that it fails in a brittle fashion, which is undesirable when it comes to plastic deformation mechanisms. Consequently, one must design magnesium alloys to navigate around this shortcoming and fail in a more ductile fashion.

However, such designs are not possible without a thorough understanding of the underlying mechanisms of deformation in magnesium, which is somewhat contested at the moment. In addition to slip, which is one of the dominant mechanisms in metallic alloys, a mechanism known as twinning is also present, especially in hexagonal close-packed (HCP) materials such as magnesium. Twinning involves the reorientation of the material lattice about a planar discontinuity and has been shown as one of the preferred mechanisms by which magnesium accommodates out-of-plane deformation. Unfortunately, twinning is not particularly well-understood in magnesium, and needs to be addressed before progress can be made in materials design. In particular, though two specific modes of twinning have been acknowledged, various works in the literature have identified a host of additional modes, many of which have been cast aside as "anomalous" observations.

To this end, we introduce a new framework for predicting the modes by which a material can twin, for any given material. Focusing on magnesium, we begin our investigation by introducing a kinematic framework that predicts novel twin configurations, cataloging these twins modes by their planar normal and twinning shear. We then subject the predicted twin modes to a series of atomistic simulations, primarily in molecular statics but with supplementary calculations using density functional theory, giving us insight on both the energy of the twin interface and barriers to formation. We then perform a stress analysis and identify the twin modes which are most likely to be activated, thus finding the ones most likely to affect the yield surface of magnesium.

Over the course of our investigation, we show that many different modes actually participate on the yield surface of magnesium; the two classical modes which are

accepted by the community are confirmed, but many additional modes — some of which are close to modes which have been previously regarded as anomalies — are also observed. We also perform some extensional work, showing the flexibility of our framework in predicting twins in other materials and in other environments and highlighting the complicated nature of twinning, especially in HCP materials.

TABLE OF CONTENTS

Acknowledgements . . . iv
Abstract . . . vi
Table of Contents . . . viii
List of Illustrations . . . x
List of Tables . . . xiv
Nomenclature . . . 1
Chapter I: Introduction and Motivation . . . 3
1.1 The Initiative of Materials Design . . . 3
1.2 The Particular Interest in Magnesium . . . 4
1.3 An Introduction to Defects in Materials . . . 6
1.4 Twinning and Identification of Twinning Modes . . . 7
1.5 The Kinematic Approach . . . 9
1.6 Challenges Leading to this Investigation . . . 10
1.7 Alloying Effects . . . 11
1.8 Plan of Action . . . 12
Chapter II: Twin Kinematics . . . 17
2.1 Goals of the Twin Kinematic Framework . . . 17
2.2 Lattices . . . 17
2.3 Twinning . . . 21
2.4 Twin Kinematic Framework . . . 22
2.5 Implementation: Kinematic Framework . . . 25
2.6 Summary . . . 26
Chapter III: Results: Twin Kinematics . . . 27
3.1 Goals of this Chapter . . . 27
3.2 Examples . . . 27
3.3 Results for Magnesium . . . 33
3.4 Results for Additional Materials . . . 39
3.5 Summary . . . 43
Chapter IV: Twin Energetics . . . 47
4.1 Goals of the Energetics Calculations . . . 47
4.2 Background on Molecular Statics and Dynamics . . . 48
4.3 Interatomic Potential Training . . . 50
4.4 Twin Interface Energy . . . 51
4.5 The Method of Nudged Elastic Band . . . 51
4.6 Additional Concepts: Atomistics . . . 55
4.7 Implementation: LAMMPS . . . 55
4.8 Background on Density Functional Theory . . . 59
4.9 Additional Concepts: MacroDFT Formulation . . . 63
4.10 Implementation: MacroDFT . . . 65

4.11 Summary . . . 66
Chapter V: Results: Twin Energetics . . . 68
5.1 Goals of this Chapter . . . 68
5.2 Perfect Crystal Calibration . . . 68
5.3 Twin Interface Energy: Magnesium . . . 69
5.4 Twin Interface Energy for Magnesium in MacroDFT . . . 71
5.5 Twin Interface Energy: Additional Materials . . . 72
5.6 Barriers to Formation: Magnesium . . . 78
5.7 Summary . . . 83
Chapter VI: Yield Surface Construction . . . 87
6.1 Goals of the Yield Surface Construction . . . 87
6.2 Stress and Yield . . . 87
6.3 Forming the Yield Surface . . . 89
6.4 Procedure for Magnesium . . . 90
6.5 Implementation: Yield Surface Construction . . . 90
6.6 Summary . . . 91
Chapter VII: Results: Yield Surface Construction . . . 92
7.1 Goals of this Chapter . . . 92
7.2 Check: CRSS of the Tension Twin . . . 92
7.3 The Updated Magnesium Yield Surface . . . 92
7.4 Summary . . . 99
Chapter VIII: Conclusions and Future Work . . . 101
8.1 Conclusions of this Investigation . . . 101
8.2 Upcoming Work . . . 102
Bibliography . . . 105
Appendix A: Supplemental Material . . . 116
A.1 Additional Background: Twin Kinematics . . . 116
A.2 Twin Interface Change of Basis . . . 121
A.3 Treatment of Multilattices . . . 123
A.4 Additional Background: Molecular Statics and Molecular Dynamics 124
A.5 Additional Concepts: MacroDFT . . . 125
A.6 MacroDFT Size Effects . . . 126

LIST OF ILLUSTRATIONS

Number *Page*

1.1 General Ashby plot of strength against density for a variety of materials from [2]. . . . 3
1.2 Ashby plot of strength against density focusing on metals and metallic alloys from [4]. . . . 5
1.3 Ashby plot of strength against elongation focusing on the metals and metallic alloys from [4]. . . . 13
1.4 Schematic stress-strain plot for a generic material. . . . 14
1.5 Example illustration of a defect in a crystalline material. . . . 14
1.6 Example illustration of a twin. . . . 15
1.7 Mechanisms of deformation in HCP materials 15
1.8 Summary of Table 1.1 in visual form, with bars representing frequency of citations found in a search for non-classical twin modes in magnesium. 16
1.9 Schematic illustration of the Bragg condition. . . . 16
2.1 Schematic examples of Bravais lattices. . . . 18
2.2 Schematic examples of cubic lattices. . . . 18
2.3 Schematic examples of multilattices. . . . 19
2.4 Schematic of the hexagonal close packed lattice. . . . 19
2.5 Schematic examples of reciprocal lattices. . . . 20
2.6 Schematic illustration of a lattice that has undergone twinning, with lattice vectors and twinning elements labeled. . . . 21
3.1 Atomic visualization for the square lattice example, with blue points representing the perfect lattice, and solid points representing the final, twinned configuration. . . . 29
3.2 The unit and the super cell used in the calculation of the potential twinning modes of magnesium along with the choice of lattice vectors. 34
3.3 Histogram of the distribution of angles of computed twin modes for magnesium, using the skeletal lattice. . . . 35
3.4 Histogram of the distribution of shear magnitudes of computed twin modes for HCP magnesium with the skeletal lattice description, with histogram bin width of 0.1. . . . 36

3.5 Histogram of the distribution of angles of computed twin modes for magnesium, using the multilattice. 37
3.6 Histogram of the distribution of shear magnitudes of computed twin modes for HCP magnesium with the multilattice description, with histogram bin width of 0.1. 38
3.7 Histogram of the distribution of angles of computed twin modes for BCC materials. 40
3.8 Histogram of the distribution of shear magnitudes of computed twin modes for BCC materials, with histogram bin width of 0.1. 41
3.9 Histogram of the distribution of angles of computed twin modes for FCC materials. 42
3.10 Histogram of the distribution of shear magnitudes of computed twin modes for FCC materials, with histogram bin width of 0.1. 43
3.11 Smoothed histograms of angular distributions for various values of c/a. 44
3.12 Smoothed histograms of angular distributions for a larger range of c/a values using the skeletal lattice description. 45
3.13 Smoothed histograms of angular distributions for a larger range of c/a values using the multilattice description. 46
4.1 Schematic illustration of nudged elastic band replicas, with energy measurements along the reaction coordinate. 52
4.2 Schematic illustration of the goals of the nudged elastic band procedure in order to position replicas along a minimum energy path. 53
4.3 Schematic illustration of the computational cell used for energetics simulations with twins. 56
5.1 Scatterplot of the twin energies for magnesium, as detected using the modified MEAM potential [144]. Cutoffs chosen are $\gamma \leq 500$ mJ/m^2 and $s \leq 8$ to capture the energies of previously-observed twin modes. 70
5.2 Atomic configuration of a predicted irrational twin, with basal direction labeling, visualized within OVITO [151]. Note that only a part of the entire simulation box is visualized. 72
5.3 Scatterplot of the twin energies for iron (BCC), as detected using the interatomic potential developed in [152]. Cutoffs chosen are $\gamma \leq 1000$ mJ/m^2 and $s \leq 8$ illustrate the sparsity of low-energy twin modes relative to magnesium. 73

5.4 Scatterplot of the twin energies for copper (FCC), as detected using the interatomic potential developed in [154]. Cutoffs chosen are $\gamma \leq 1000$ mJ/m^2 and $s \leq 8$ illustrate the sparsity of low-energy twin modes relative to magnesium. 74
5.5 Scatterplot of the twin energies for magnesium with n weight percent aluminum, as detected using the EAM potential. Cutoffs chosen are $\gamma \leq 1000$ mJ/m^2 and $s \leq 8$ to capture the energies of previously-observed twin modes. 76
5.6 Scatterplot of the twin energies for titanium with n weight percent aluminum, as detected using the EAM potential. Cutoffs chosen are $\gamma \leq 1000$ mJ/m^2 and $s \leq 8$ to capture the energies of previously-observed twin modes. 77
5.7 Arrhenius plot of up to 1200 K for the 20 modes that are within the region $\gamma \leq 300$ mJ/m^2 and $s \leq 2$. 79
5.8 Arrhenius plot of up to 1200 K for the 20 modes that are within the region $\gamma \leq 300$ mJ/m^2 and $s \leq 2$, subjected to 0.1% tension. 80
5.9 Arrhenius plot of up to 1200 K for the 20 modes that are within the region $\gamma \leq 300$ mJ/m^2 and $s \leq 2$, subjected to 0.2% tension. 81
5.10 Arrhenius plot of up to 1200 K for the 20 modes that are within the region $\gamma \leq 300$ mJ/m^2 and $s \leq 2$, subjected to 0.5% tension. 81
5.11 Arrhenius plot of up to 1200 K for the 20 modes that are within the region $\gamma \leq 300$ mJ/m^2 and $s \leq 2$, subjected to 1% tension. 82
5.12 Arrhenius plot of up to 1200 K for the 20 modes that are within the region $\gamma \leq 300$ mJ/m^2 and $s \leq 2$, subjected to 1.5% tension. 82
5.13 Arrhenius plot of up to 1200 K for the 20 modes that are within the region $\gamma \leq 300$ mJ/m^2 and $s \leq 2$, subjected to 2% tension. 83
5.14 Arrhenius plot of up to 1200 K for the 20 modes that are within the region $\gamma \leq 300$ mJ/m^2 and $s \leq 2$, subjected to 0.1% compression. . . 83
5.15 Arrhenius plot of up to 1200 K for the 20 modes that are within the region $\gamma \leq 300$ mJ/m^2 and $s \leq 2$, subjected to 0.2% compression. . . 84
5.16 Arrhenius plot of up to 1200 K for the 20 modes that are within the region $\gamma \leq 300$ mJ/m^2 and $s \leq 2$, subjected to 0.5% compression. . . 84
5.17 Arrhenius plot of up to 1200 K for the 20 modes that are within the region $\gamma \leq 300$ mJ/m^2 and $s \leq 2$, subjected to 1% compression. . . . 85
5.18 Arrhenius plot of up to 1200 K for the 20 modes that are within the region $\gamma \leq 300$ mJ/m^2 and $s \leq 2$, subjected to 1.5% compression. . . 85

5.19 Arrhenius plot of up to 1200 K for the 20 modes that are within the region $\gamma \leq 300$ mJ/m^2 and $s \leq 2$, subjected to 2% compression. . . . 86
6.1 Schematic illustration of the maximum barrier state. 88
7.1 Representative slice of the magnesium yield surface which would be more indicative of a classical picture, with the classical tension twin mode dominating the yield surface, alongside traditional slip systems. Exact information on the tension twin is represented in Table 7.1 . . . 93
7.2 A representative slice of the magnesium yield surface in which an irrational twin modes dominates the yield surface. The exact identities of these twins are displayed in Table 7.1 94
7.3 Representative slices of the magnesium yield surface in which multiple twin modes now dominate the yield surface. The exact identities of these twins are displayed in Table 7.1 95
7.4 Plot of all twin configurations with twin boundary energy γ^{tw} under 500 mJ/m^2 and calculated shear magnitude $s < 8$ using the Modified MEAM potential by Wu *et al.* Red dashed line denotes the boundary of points which were subjected to further nudged elastic band and stress calculation. Orange points denote twin systems which were detected to play a role in the yield surface of magnesium. The tension (T) and compression (C) twins are also highlighted. 96
7.5 EBSD image from sample of magnesium subjected to impact at strain rate of $\dot{\varepsilon} = 10^3$ s^{-1}. Image reproduced with permission of Hazeli and Ramesh. 98
7.6 Reiterated plot of γ^{tw} vs. shear magnitude, with systems matched against the EBSD data now denoted with purple. The label by these points names the interface whose rotation was identified. 99
A.1 Plot of the energy per atom in eV as a function of the thickness of the twin region for the $(10\bar{1}2)$ classical variant. The different curves show energy results as the width of the computational cell is increased. The dashed line represents the cohesive energy E_0^{pc}. 127

LIST OF TABLES

Number *Page*

1.1 Table of previously-identified twin modes in various HCP materials. . 8

3.1 Tabulated values of shear magnitudes for several twin modes of interest, calculated using both the skeletal lattice and multilattice descriptions of HCP magnesium. 38

5.1 Relaxed lattice parameters and cohesive energy obtained from potential training. 68

5.2 Elastic constants calculated from the optimal parameters of Table 5.1. 69

5.3 Details on twelve example twin systems with $\gamma^{\text{tw}} \leq 325$ mJ/m^2 and $s \leq 4$. 71

5.4 Tabulation of γ^{tw} for several example low-energy twin modes, with results from MacroDFT compared to values previously found in literature. 71

5.5 Tabulation of twin interface energy for the tension (a) and compression (b) twins for changing weight percentages of aluminum in magnesium. 76

5.6 Tabulation of twin interface energy for the tension (a) and compression (b) twins for changing weight percentages of aluminum in titanium. . 77

5.7 Values of the stacking fault energy for magnesium and titanium with increasing weight-percentage aluminum, using the interatomic potentials developed in [156] for Mg-Al and [158] for Ti-Al. 78

5.8 Updated details on twelve example twin systems with $\gamma^{\text{tw}} \leq 325$ mJ/m^2 and $s \leq 4$ from Table 5.3, with information now including the barrier and attempt frequency. 79

6.1 Values of the critical resolved shear stress of magnesium slip systems 91

7.1 Details of the twin systems which were found to affect the yield surface of magnesium. The first column is an arbitrary label. System a is the classical tension twin while system b is the classical compression twin. The subscript I denotes an irrational index which has been rounded to a nearby integer. 94

LIST OF ALGORITHMS

2.1 Procedure for identifying possible and relevant twin modes in a given material of interest. 26
4.1 Procedure for identifying the minimum-energy lattice parameters for studying a material of interest. 57
4.2 Procedure for handling rational vs. irrational twin planes. 58
4.3 Procedure for computing the twin interface energy. 59
4.4 Procedure for computing the barriers to formation for the twins. . . 60
4.5 Modified Lanczos algorithm which is used within MacroDFT. . . . 66
4.6 Procedure for identifying the minimum-energy lattice parameters for studying a material of interest. 67
5.1 Modifications suitable for computing twinning energies for alloys. . 75
6.1 Procedure for taking stress information and identifying the relevant twin modes. 91

NOMENCLATURE

η_1. classical twinning element capturing the twinning shear.

η_2. classical twinning element capturing direction which remains undistorted.

$\gamma^{\mathbf{tw}}$. interface energy of a particular twin.

κ. twinning conjugacy solution branch.

λ_i. eigenvalues.

$\boldsymbol{\delta}$. identity matrix.

$\hat{\boldsymbol{n}}$. normal vector to the twin plane.

$\boldsymbol{\sigma}$. stress tensor.

$\boldsymbol{\sigma}^{\mathbf{vir}}$. virial stress.

$\boldsymbol{\sigma}_Y$. stress tensor at maximal barrier state.

$\boldsymbol{\varepsilon}$. strain tensor.

$\boldsymbol{C}$. right Cauchy-Green deformation tensor.

$\boldsymbol{e}^i$. reciprocal lattice vectors describing perfect crystal (reference material).

$\boldsymbol{e}_i$. direct lattice vectors describing perfect crystal (reference material).

$\boldsymbol{F}$. deformation gradient.

$\boldsymbol{f}_i$. direct lattice vectors describing twinned crystal through rotation.

$\boldsymbol{g}^i$. reciprocal lattice vectors describing perfect crystal (reference material).

$\boldsymbol{g}_i$. direct lattice vectors describing twinned crystal through simple shear.

$\boldsymbol{Q}$. rotation matrix.

$\boldsymbol{s}$. twinning shear vector.

$\mathcal{Y}$. elastic domain.

$\mathsf{E}^{\mathbf{tw}}$. energy of the twinned configuration.

$\mathsf{E}_0^{\mathbf{pc}}$. perfect crystal cohesive energy.

T. temperature.

μ_i^j. lattice equivalence metric.

ν_0. attempt frequency.

ω_i. acoustic tensor eigenvalues.

σ^i. resolved shear stress for i^{th} mode.

σ_Y^i. critical resolved shear stress for i^{th} mode.

τ^i. resolved shear stress for i^{th} mode.

θ. angle of rotation of rotation matrix.

a. lattice constant (lattice spacing).

$A_{\textbf{interface}}$. area of the twin interface.

c. lattice height constant (for HCP materials).

K. Arrhenius frequency.

K_1. classical twinning element capturing the twin plane normal.

K_2. classical twinning element capturing plane which remains undistorted.

k_B. Boltzmann constant (1.3806×10^{-23} J/K).

$n_{\textbf{atoms}}$. number of the atoms in a twin energy simulation.

s. magnitude of twinning shear.

(C)RSS. (critical) resolved shear stress.

(HR)TEM. (high resolution) transmission electron microscopy.

(M)EAM. (modified) embedded atom method.

BCC. body-centered cubic.

DFT. density functional theory.

EBSD. electron back-scattered diffraction.

FCC. face-centered cubic.

HCP. hexagonal close-packed.

LAMMPS. Large-scale Atomic/Molecular Massively Parallel Simulator.

MD. molecular dynamics.

MS. molecular statics.

NEB. nudged elastic band.

OVITO. Open Visualization Tool.

replica. an intermediate step lying between a beginning state and end state.

Chapter 1

INTRODUCTION AND MOTIVATION

1.1 The Initiative of Materials Design

From a broader perspective, our goal as engineers is to improve society; but in the scope of materials design, what exactly does improvement entail? While there are undoubtedly many aspects that can be changed in order to attain some notion of improvement, the one that we will concern ourselves with — for the duration of this work, at least — is the notion of maintaining or increasing a material's strength and ability to resist failure in extreme environments while decreasing its weight. Reference any Ashby plot (such as the one on [1] or Figure 1.1 below), and the goal in designing new materials will be to push the envelope up and to the left, increasing strength while reducing density.

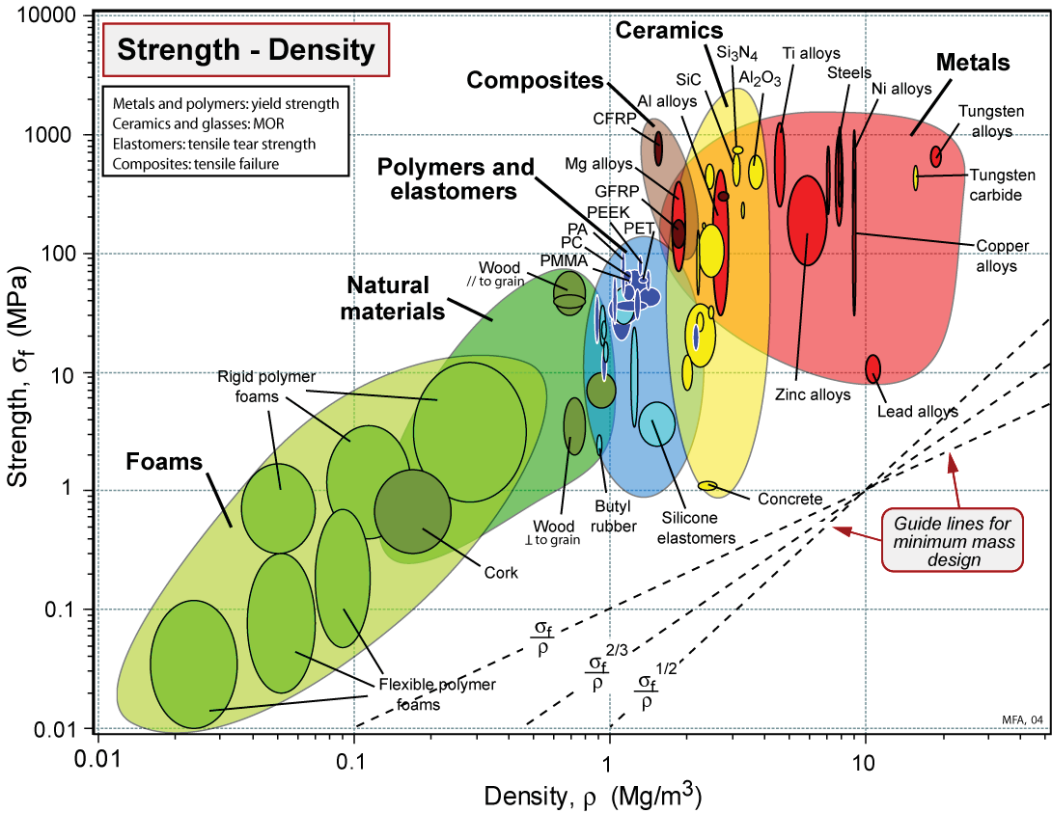

Figure 1.1: General Ashby plot of strength against density for a variety of materials from [2].

Metals and their alloys have been shown time and again to possess some of the highest strengths amongst all known materials, and this is reflected in Figure 1.1 by the fact that metals sit very high up on the vertical axis. Unfortunately, this has come at the cost of significant weight, denoted by the fact also that metals and their alloys are almost the farthest to the right in Figure 1.1.

To counteract this, contemporary materials engineering efforts have sought to combine materials together through alloying; this has resulted in the properties of the alloyed material exceed those of any of the individual constituents. Consequently, it has been tasked upon us to identify new candidate materials that can be alloyed in order to further improve upon material strength while further reducing the overall weight.

1.2 The Particular Interest in Magnesium

One of the new, lightweight materials that is seeing selected but increasing application is magnesium. Magnesium alloys have started appearing in instances which see the need for a lightweight yet resilient material due to its high strength-to-weight ratio [3]. For instance, modern professional camera bodies are built around a magnesium alloy chassis encased in a hardened plastic shell for ease of handling. In this application, magnesium alloys were chosen out of interest to design a camera body with low weight but high strength in order to be able to protect the optics and electronics

The integration of magnesium alloys into camera bodies is but one of what is hoped to eventually be a plethora of areas where magnesium alloys can improve society; the driving force behind this investigation is the broad interest to incorporate magnesium as the basis for the design of the next generation of alloys. Imagine the integration of magnesium alloys into automobiles and aircraft, which would allow for more lightweight vehicles and, thus, greater fuel efficiency. Envision a society with magnesium alloy bone implants. Wherever there is a need for lightweight, strong materials, it is hoped that magnesium alloys will eventually see deployment. As seen in Figure 1.2, magnesium is a promising alternative to the steel- and aluminum-based alloys widely in use throughout the industry today due to the fact that, although it retains comparable strength to these aforementioned materials, magnesium only has a fraction of the weight.

Although already seen in some applications, some barriers exist between a more widespread adoption of magnesium alloys. The first and foremost issue is that, compared to most other metals which see considerable industrial use today, magnesium by itself displays a very poor *ductility*, or ability to elongate without breaking. A visual

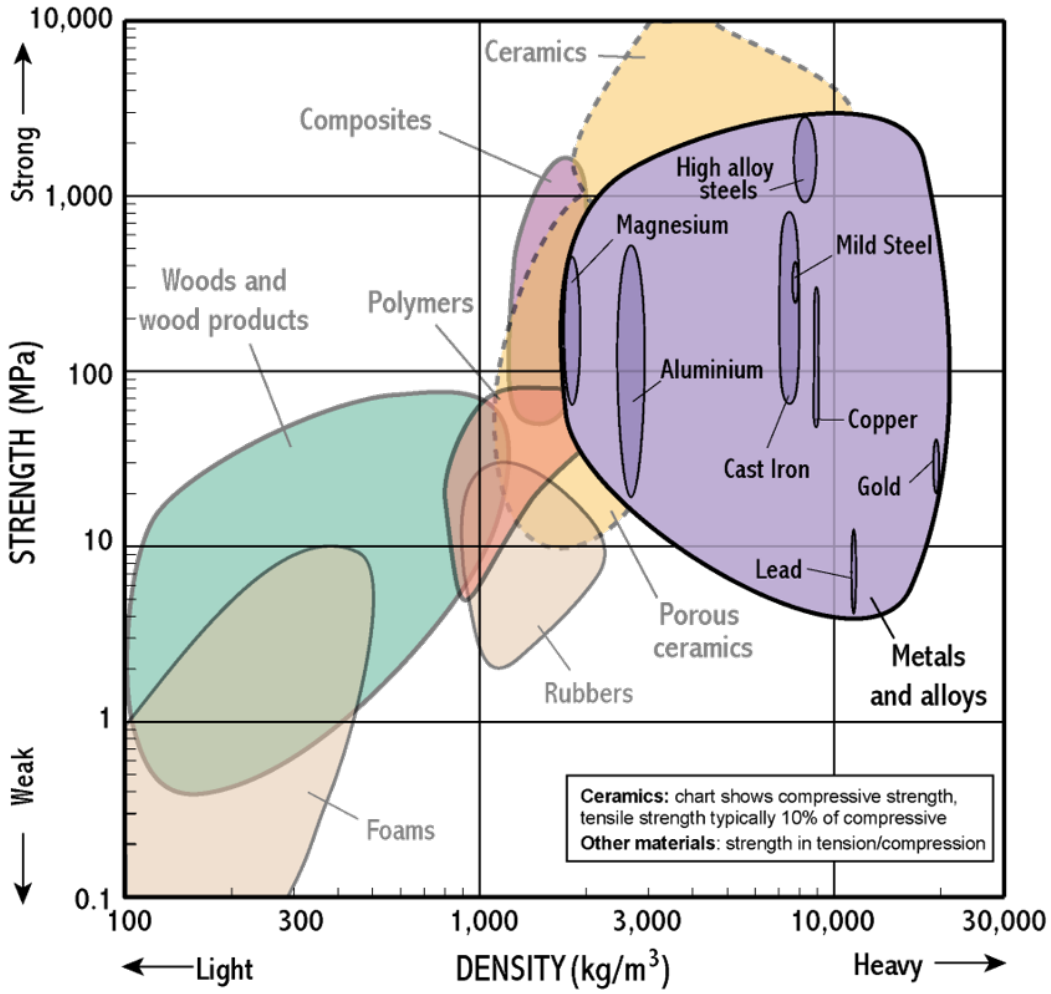

Figure 1.2: Ashby plot of strength against density focusing on metals and metallic alloys from [4].

representation of this is shown in Figure 1.3. As seen in Lu *et al.* [5, 6], the ductility of magnesium limits their ability to be integrated widely at the present. Efforts have been made in the past few years to improve upon their ductility without sacrificing strength through various alloying, which will be discussed more in Section 1.7

We've seen time and again that, for deformations too severe for a material to remain elastic, we observe irreversible, *plastic deformation*. This can be seen, for instance, when you distort a paper clip; if you tug on it gently, the paper clip might deform slightly, but it will return to its initial configuration. Pull it too far and it will remain in a permanently-deformed configuration. Pull far enough and eventually the clip will break entirely.

When magnesium exceeds its elasticity, its failure is very brittle in fashion; elongating

magnesium will reach failure quickly and without much warning. A schematic illustration of the stress-strain plot is shown in Figure 1.4; in this case, magnesium by itself would follow the red curve and fail without much warning.

As such, before we can fully integrate magnesium as a basis for alloys, we need to be able to design alloys that overcome this failure and fail in a more graceful, ductile fashion, i.e. a failure path similar to that following the green trajectory of Figure 1.4. Part of the reason why we aren't able to do this at the moment is because our overall understanding of the mechanisms by which magnesium accommodates deformation is very poor, and significant debate over these mechanisms is still ongoing. Consequently, our first task is to develop a better understanding of these mechanisms in magnesium.

1.3 An Introduction to Defects in Materials

From a macroscopic standpoint, we can see failure mechanisms in terms of plastic deformation; at the atomistic scale, plastic deformation manifests from the formation of defects in a material. In the scope of metals, an ideal sample will have nothing but a perfect, repeating crystal lattice. Of course, no real world samples can achieve such perfection, and all materials will have some kind of defects within them, such as a dislocation illustrated in Figure 1.5.

In this work, we choose to concentrate on a particular type of planar discontinuity known as a *twin*. First identified in the 1950s [7–9], twinning is the reorientation of a material's lattice about a discontinuity plane, as represented in Figure 1.6. Generally speaking, twinning has been accepted as one of the potential avenues by which a material can accommodate deformation. Although twinning is present in virtually all of the common crystallographic material classes, such as body-centered cubic (BCC) and face-centered cubic (FCC) materials (and others) [10–21], it appears to be reasonably well-understood in those materials due to the limited number of systems that can arise from the relatively highly-symmetric cubic crystal classes.

On the other hand, twinning is not nearly as well understood in HCP materials. The reason for the complicated picture of twinning (and, more generally, deformations) in HCP materials originates from asymmetry in the lattice structure. Consequently, we have easy slip in the basal planes. However, slip in the other directions — known as the prismatic and pyramidal directions — is difficult; it is because of this barrier to slip in the non-basal directions that twinning arises as a competitive means for deformation accommodation. A schematic summary of the slip modes and some

examples of twins are shown in Figure 1.7.

Though not as prevalent as slip when examining the plastic deformation of metallic alloys, twinning nevertheless remains an important mechanism due to the general difficulty in activating prismatic and pyramidal slip relative to basal slip. This leaves a great possibility for HCP materials to activate twinning as a means for accommodating out-of-plane deformations, which basal slip would not resolve, and is where we will begin our investigation.

1.4 Twinning and Identification of Twinning Modes

A central objective when it comes to studying twinning in materials is the identification of the orientations of planes about which a material can undergo twinning. Attempts to identify twins started in the 1950s, with work by Kiho [22, 23] and later Jaswon and Dove [24–26]; these early efforts were reviewed by Mahajan and Williams [27]. The later review article by Christian and Mahajan [28] provides a very comprehensive summary of all of the efforts that have been made to identify these twin modes from both a geometric and experimental point of view; techniques such as high resolution transmission electron microscopy (HRTEM) and X-ray diffraction (XRD) have helped researchers in this task. Despite these advances, resolving all of the possible twin modes in a material is still a great challenge, especially when it comes to resolving some of the more discreet twin modes. For instance, difficulties in orienting a sample for such imaging technique still make it difficult for researchers to discern the existence of planes which may have irrational crystallographic indices. Likewise, though various works throughout the past few decades have identified potential modes of twinning by matching lattices on both sides of the twin plane in order to identify all of the possible configurations by which twinning is possible, only a handful of modes have been confirmed to exist; these modes are tabulated in Table 1.1. In particular, Christian and Mahajan [28] have postulated the existence of a significantly greater number of twin modes, but many of these additional modes have not been explicitly confirmed in additional works of literature.

The contemporary, contested area of twinning are which planes can actually exist as twin planes. An enormous volume of works have been dedicated to the study of the $\{10\bar{1}2\}\langle 10\bar{1}1\rangle$ *tension twin* system, with some concluding that it is the only feasible mode of twinning that can be activated. The other twin mode which has been studied significantly is the $\{10\bar{1}1\}\langle\bar{1}012\rangle$ *compression twin*, although there have been debates as to whether or not this mode is feasible due to its allegedly high

activation stress. Several other prominent twin modes have appeared in literature over the years, although the observation of such modes has, quite often, been written off as anomalous observations. A brief summary of these literature results is shown in Table 1.1 and also visualized in Figure 1.8.

***n* (Indices)**	***s* (Indices)**	**Material**	**Citations**
$\{10\bar{1}2\}$	$\langle 10\bar{1}1\rangle$	All	[28]; Ti:[29, 30]; Co:[31]; Zr:[32]; Zn:[29, 33]; Be:[29] Mg:[29, 34–53], and many additional contemporary works
$\{10\bar{1}1\}$	$\langle 10\bar{1}2\rangle$	Mg, Ti	[28]; Ti:[32, 54]; Mg:[34, 36, 37, 40, 42, 44, 45, 49, 51, 53, 55–58], and many additional contemporary works
$\{11\bar{2}2\}$	$\langle 11\bar{2}3\rangle$	Mg, Ti, Zr	[28]; Ti:[29, 30, 32, 37, 44, 54]; Zr:[32]
$\{11\bar{2}1\}$	$\langle 11\bar{2}6\rangle$	Mg, Re, Ti, Zr, Co	[28]; Re:[59]; Ti:[29, 37, 44, 60]; Zr:[61], [62–64]; Co:[31]
$\{10\bar{1}3\}$	$\langle 30\bar{3}2\rangle$	Mg	[28, 36, 40, 57, 58, 65]
Unidentified	-	Mg	[40, 42, 45, 52, 66]

Table 1.1: Table of previously-identified twin modes in various HCP materials.

Over time, research efforts have shifted more towards tasks such as the precise construction of the compression and tension twins and away from attempting to identify additional modes which might exist in magnesium. For instance, El Kadiri *et al.* [48] and Li and Ma [43]) have worked to provide accurate atomistic reconstructions of twins. A variety of other works have sought to understand the mechanisms by which these two twins might form. However, we still cannot quite ignore the fact that rows other than the tension and compression twin exist in Table 1.1 and Figure 1.8; are they merely anomalous observations?

Electron Backscatter Diffraction

The technique of *electron backscatter diffraction*, which is shortened to *EBSD*, is one of the common experimental techniques for identifying orientations within a crystal. A polished sample is placed at an orientation in a scanning electron microscope chamber which is equipped with a backscatter detector. Electrons are then fired at the sample, some of which consequently backscatter and then exit at the Bragg condition,

represented in Equation (1.1) and Figure 1.9

$$2d \sin[\theta] = n\lambda, \tag{1.1}$$

where λ is the wavelength of the incident wave and n is a positive integer. The angle θ then gives the orientations at which the constructive interference patterns are strongest.

The diffraction patterns end up forming Kikuchi bands; these bands provide orientation information, including the orientation of the lattice with respect to a reference crystal lattice orientation. Different regions of a sample will have different orientations; it is then possible to examine the orientation of different regions with respect to each other and then deduce the orientation of any interfaces that lie in between the two oriented regions. Additional details on EBSD can be found in Schwartz *et al.* [67].

(High Resolution) Transmission Electron Microscopy

With *transmission electron microscopy*, also abbreviated as *TEM*, a beam of electrons are transmitted through a very thin sample. Diffraction patterns are obtained from these images, following which orientations can be back-computed as before. Because of the fact that they use electrons instead of standard optical visualization techniques, the detail resolved from these images is high enough to usually capture details at the atomic scale. As a higher resolution is sought, samples need to be thinner and the energy of the input electron beam needs to be increased; the thinness of the sample and these additional constraints pose limitations for what can be visualized, as the sample needs to be prepared and oriented cleverly in order to resolve sought-after details. Additional details on HRTEM can be found in Spence [68] and Fultz and Howe [69].

1.5 The Kinematic Approach

Rather than geometrically describe the location of each of the atoms in a particular twin, a more general description of the material requiring very few adjustments between the various twinned states is sought. Attempts at such kinematic descriptions of twinning began as early as the 1950s. However, a major step forward in kinematic descriptions of twinning came in the 1960s, with works by Bilby and Crocker [70] and also Bevis and Crocker [71, 72]; here, twins were treated as affine deformations and treatments of shears and shuffles an integral part of the theory, and these were the first works that were fairly rigorous in their descriptions of the kinematics.

Subsequent formulations of twins began to introduce certain elements that would eventually become the basis of this work. The introduction of a lattice equivalence metric in the 1960s and 1970s [73–75] (more details in Subsection 2.2) allowed for an even richer lattice description of the material. In the 1970s and 1980s Ericksen began to formulate additional lattice-based approaches for understanding crystalline materials and their phase transitions, with a particular interest in attempting to link concepts up to a continuum scale from the lattice [76–81]; Ericksen's furthering of this theory was then applied to twinning by James [82]. Pitteri, [83, 84], whose 1985 work will become a leading benchmark for our upcoming investigation of twinning, then used the lattice-based twinning approach to describe previously-observed twin modes. Ball and James then developed further theorems to calculate the particular aspects — such as the orientations of planes — in these lattices[85, 86]. Work on these lattices was then continued by Zanzotto [87–89] and Ericksen [90–93].

Though work on the kinematic description of twinning still continues to this day, the focus has consistently been on establishing twins as two-fold rotations which would be consistent with the classical notion that twinned configurations involved the symmetric reorientation of the crystal lattice across the twin plane. As we will see, the immediate restriction to two-fold rotations does limit the predictive capabilities of many earlier works, and our approach to use kinematics to *predict* new twin modes will take on a slightly different approach.

1.6 Challenges Leading to this Investigation

In Table 1.1, the last few rows pique the most interest. Why exactly are these additional modes observed in the literature of these HCP materials, but not widely acknowledged? What exactly are these unidentified twin modes, and do they play a role in governing the behavior of, in this case, magnesium? Why have Christian and Mahajan predicted so many additional twin modes which haven't been followed up upon? These so-called anomalous modes, though rare, must still be addressed; some of these modes have been postulated to occur around non-crystallographic, irrational planes.

Part of the reason why, up to now, this has been an unanswered question, lies with the complex nature of HCP lattices. Since HCP is not a Bravais lattice, constructing the material involves consideration of shuffles — effective atomic displacements in addition to the usual notion of lattice vectors, which are necessary to give the correct configuration. As such, describing twinning in those materials is a difficult task,

since there are endless ways that one could go about using different combinations of lattice vectors and shuffles to produce the twinned configuration. When it comes to quantifying what these unidentified twin modes are, it becomes necessary to use a different technique than what has been mentioned here, since that set of unidentified twins could very well number into the thousands or more and a more-efficient method of cataloging and describing these twins needs to be used.

1.7 Alloying Effects

Even though the deformation mechanisms in magnesium are not fully understood yet, research efforts have always kept an eye on the potential effects of alloys, since we are ultimately pursuing the design of *alloys* — materials with multiple constituent elements — and not just bulk magnesium. Consequently, research efforts have been looking into hardening and other mechanical effects of solute atoms for decades; only more recently have numerical techniques caught up and provided us reasonably accurate insight on systems whose behavior would not accurately be captured by analytic theories alone.

One such example of an early investigation came from Fleischer in 1962 [94], in which he drew on concepts from earlier works [95–97] to examine flow- and velocity-stress properties of dislocations in LiF with 80 parts-per-million magnesium, confirming that hardening was tetragonal, with elasticity arising from ionic attraction as had been shown in previous works; this provided a glimpse at the ability to calculate dislocation mobility and flow stress variation with the temperature. In 1963 [98], Fleischer used concepts from [99–102] in order to examined the effects of copper alloyed with a variety of other elements, finding that the hardening by substitutional impurities arises due to the interactions of solute atoms with screw dislocations that are generated in the matrix copper. In 1967 [103], Fleischer then also looked into BCC materials, using concepts from Peierls [104] and a new-at-the-time theory developed by Dorn and Rajnak [105] to find that, for iron alloyed with carbon and niobium alloyed with nitrogen that lattice/Peierls-Nabarro hardening is not the dominant source of low temperature strength, with interstitial impurities contributing to the major portion of the hardening, requiring further modeling considerations. Some forays into magnesium alloys have been made, such as in Clark [106] and Nussbaum *et al.* [107], which have looked at the addition of zinc into Mg-Al systems, examining effects such as precipitates.

Studies of alloys have greatly intensified since the turn of this century. For instance,

in Rzychoń and Kielbus [108] considered the addition of rare earth elements into Mg-Al systems, finding that certain additions of these rare earth elements led to a heaver appearance of secondary phases with $Al_x(RE)_y$ but didn't quite find a generalizable trend. Yang [109] considered some more complicated Mg-Al systems with zinc and other solutes. Many other examples of attempts to improve ductility in magnesium alloys without sacrificing strength exist; a few such examples include [110–113]. Computational efforts, such as those by Leyson *et al.* [114] and Shang *et al.* [115] have attempted to quantitatively predict solute strengthening and effects on the stacking fault energy, but only for dilute systems.

In terms of twinning, one particular driving force for us here is the fact that works such as Fitzner *et al.* [116] report that, above roughly 7% by weight of aluminum, twinning activity in these alloys is allegedly suppressed. Even though precipitates and general understanding of microstructural effects of solute atoms are still not fully understood, we will ultimately need to also develop a twin framework that can also capture behavior for alloys.

1.8 Plan of Action

In order to address the questions of what all possible and likely twin modes in a material are, we adopt the lattice-based approaches described in Section 1.5. Consequently, we are going to build on the precedent set in these works, using them to try and predict new twin modes in materials (as opposed to the immediate restrictions to two-fold rotations and earlier interests in describing observed modes). In this thesis, we will develop a novel framework that first kinematically predicts the possible twin modes in a given material. We will then examine the energetics of these twins from an atomistic scale and then work our way towards the construction of a new yield surface that identifies the twin modes which are likely to affect yield behavior in magnesium. Through this work, we will show that there are, indeed, a significant number of additional twin modes affecting yield behavior in magnesium that others have yet to fully consider.

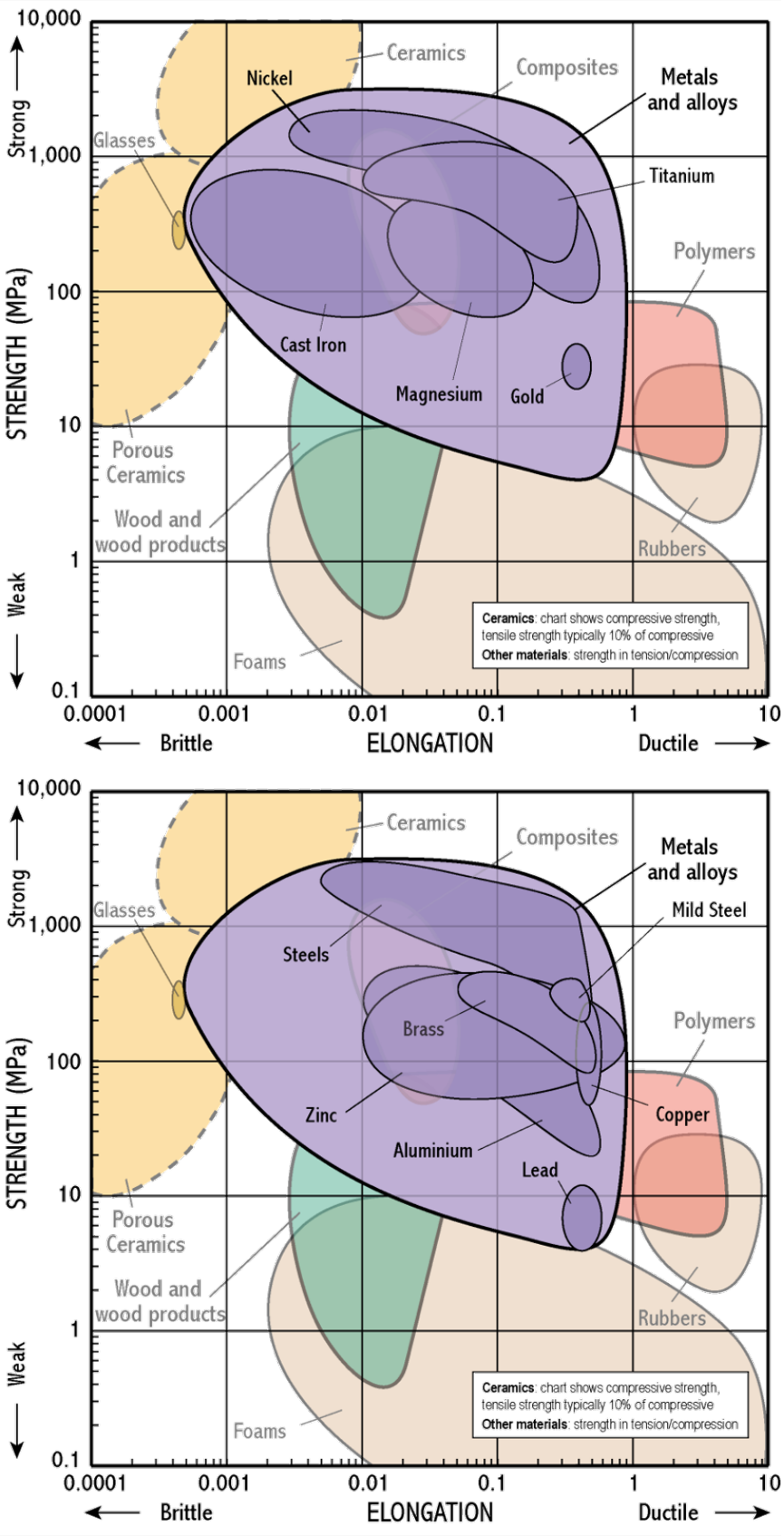

Figure 1.3: Ashby plot of strength against elongation focusing on the metals and metallic alloys from [4].

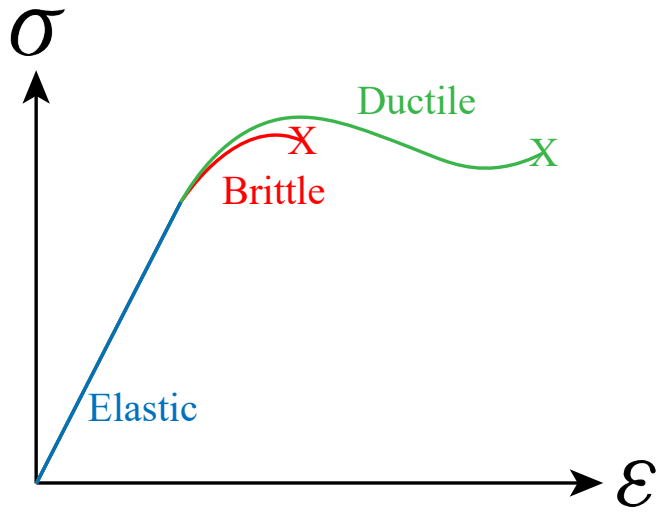

Figure 1.4: Schematic stress-strain plot for a generic material.

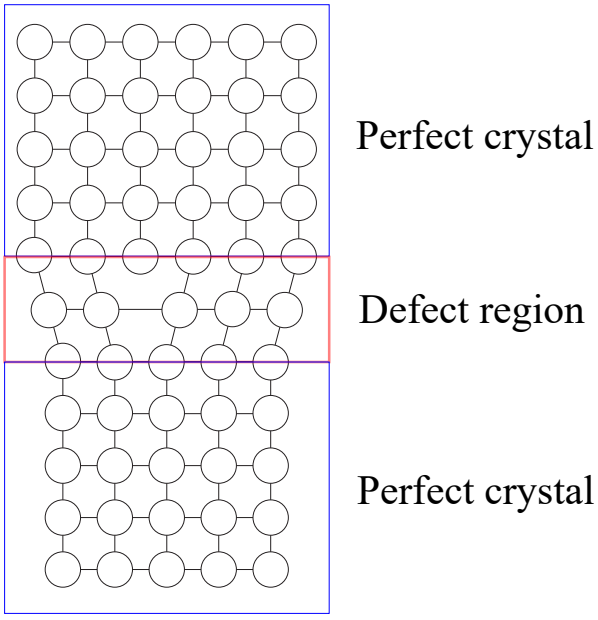

Figure 1.5: Example illustration of a defect in a crystalline material.

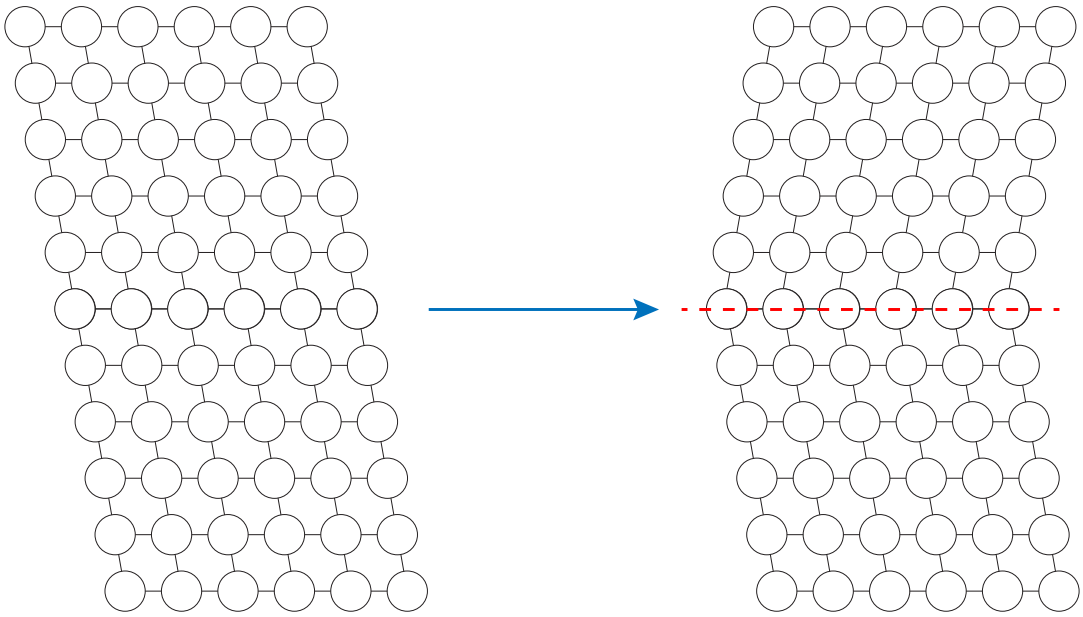

Figure 1.6: Example illustration of a twin.

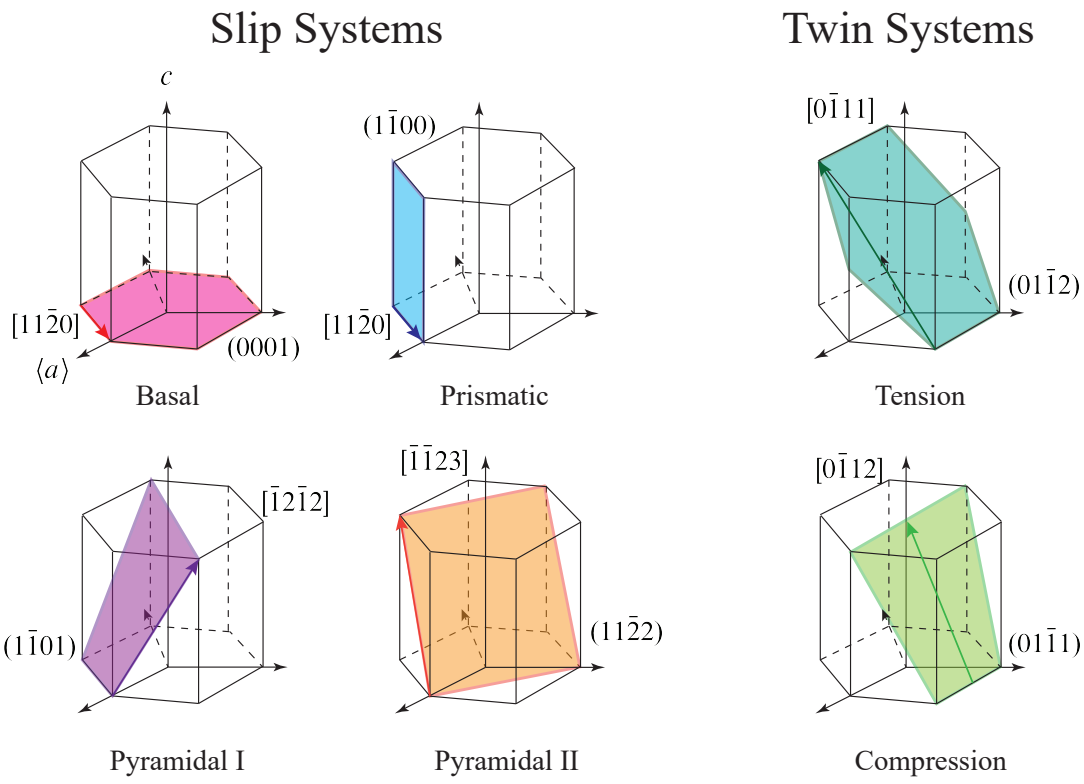

Figure 1.7: Mechanisms of deformation in HCP materials

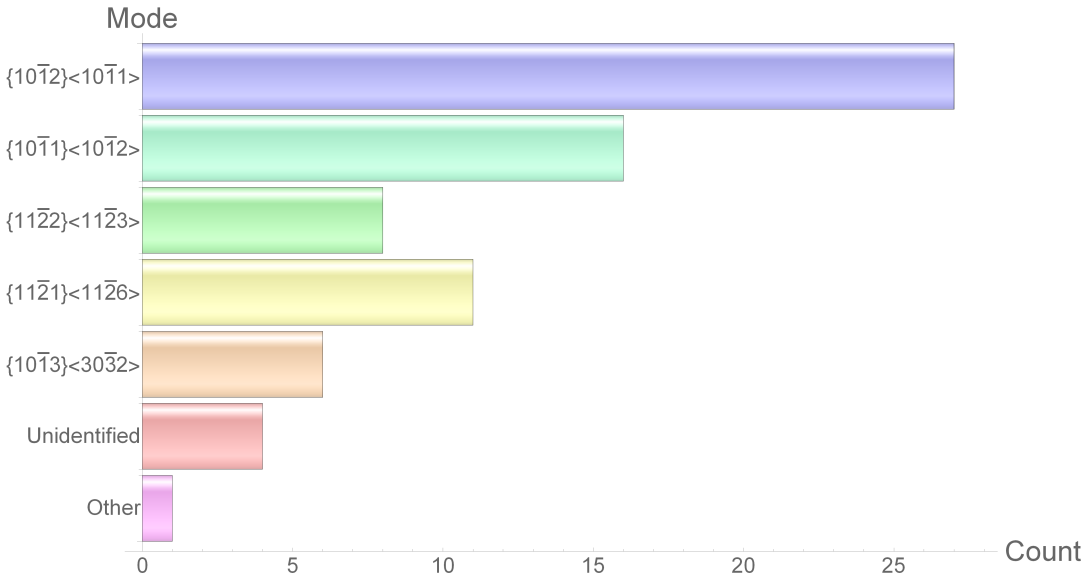

Figure 1.8: Summary of Table 1.1 in visual form, with bars representing frequency of citations found in a search for non-classical twin modes in magnesium.

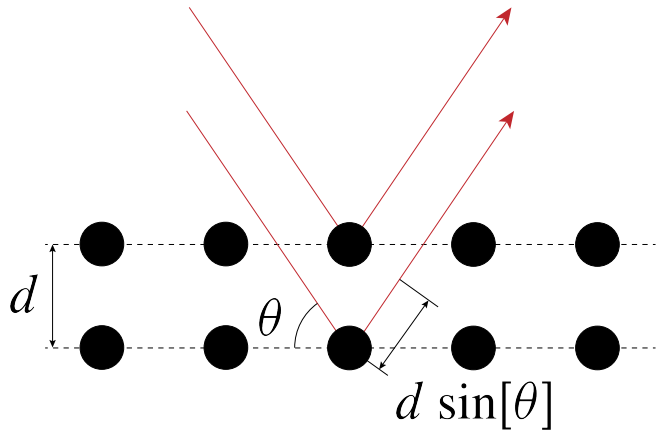

Figure 1.9: Schematic illustration of the Bragg condition.

Chapter 2

TWIN KINEMATICS

2.1 Goals of the Twin Kinematic Framework

The first step in explaining twins is to predict, for any given material, what are the kinematically allowable modes by which a material may twin. Consequently, in this chapter, we explore the fundamental concepts behind this framework. We first introduce essential background concepts and terminology for lattices. We then review the mathematics that led to the development of the framework. Finally, we discuss our implementation of this framework as a tool for predicting twin modes rather that would not have been previously considered.

2.2 Lattices

Let us consider a crystalline material for the time being. The crystalline nature of the material ensures that there is some degree of periodicity; this allows for the description of the material by what are known as lattice vectors. We suppose that, in its initial state, we can describe the material of interest by a set of lattice vectors $\boldsymbol{e}_i$, with $i = 1, 2, 3$. As the material is assumed to be free of defects, this description of the material by the lattice vectors is *almost* complete; for a *Bravais lattice* $\mathcal{L}_b$, a defect-free material can be completely described by the lattice vectors $\boldsymbol{e}_i$ through the relationship

$$\mathcal{L}_b = \left\{ x : x = \sum_{i=1}^{3} n_i \boldsymbol{e}_i, n_i \text{ integers} \right\}. \tag{2.1}$$

Examples of Bravais lattices include *body-centered cubic*, i.e. *BCC*, and *face-centered cubic*, i.e. *FCC* materials. A schematic example of Bravais lattices is shown in Figure 2.1, and some examples of cubic lattices are shown in Figure 2.2.

The wrinkle with this is when one has to also consider a *non-Bravais lattice*; in particular, we focus on the notion of a *multilattice*, where the material is described by the union of a finite number of Bravais lattices . In such a case, a full description of the lattice $\mathcal{L}_{nb}$ would require

$$\mathcal{L}_{nb} = \left\{ x : x = \sum_{i=1}^{3} n_i \boldsymbol{e}_i + \sum_{k=1}^{K-1} \eta_k \boldsymbol{p}_k, n_i \text{ integers} \right\} \tag{2.2}$$

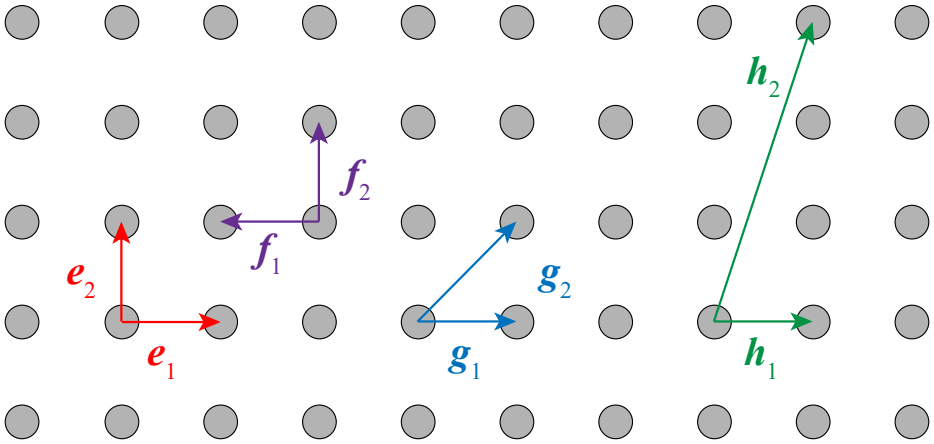

Figure 2.1: Schematic examples of Bravais lattices.

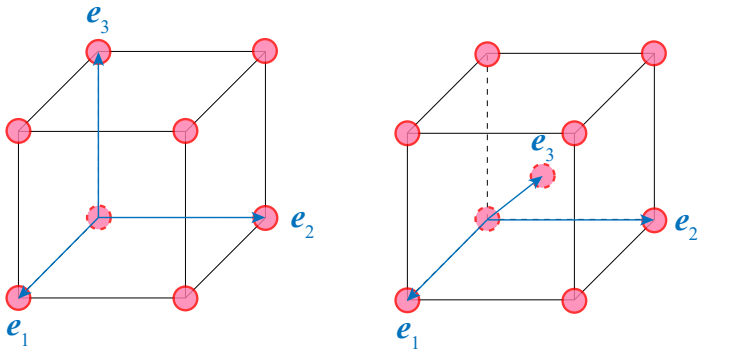

Simple Cubic Body-Centered Cubic (BCC)

Figure 2.2: Schematic examples of cubic lattices.

with $\boldsymbol{p}_k$ being known as *shifts* and K being the number of atoms in the unit cell. Examples of multilattices are shown in Figure 2.3, where we can see that two lattices have been merged to create the material. Unfortunately for us, *hexagonal close-packed* (*HCP*) materials fall into this domain of multilattices, with $K = 2$ in typical descriptions. For visualization, a schematic of the typical HCP lattice is shown in Figure 2.4. Furthermore, by choosing a larger unit cell, we can change the periodicity and the value of K, further complicating the lattice description. We shall see later that the introduction of the larger unit cell can actually be useful.

Deformation Gradient

From continuum mechanics, the *deformation gradient* gives the measure of distortion of a material between two different configurations of interest. For a material that is described in its initial reference state by some set of coordinates X_J, with $J = 1, 2, 3$, and then in a second, current configuration by some set of coordinates x_i, with

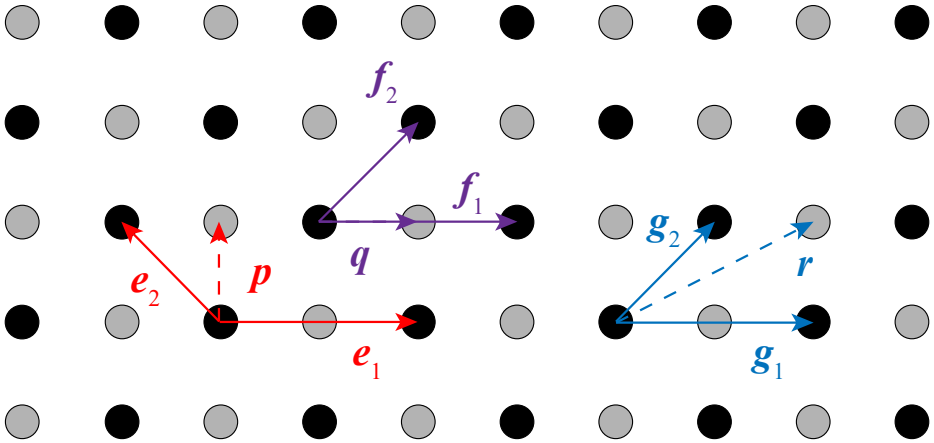

Figure 2.3: Schematic examples of multilattices.

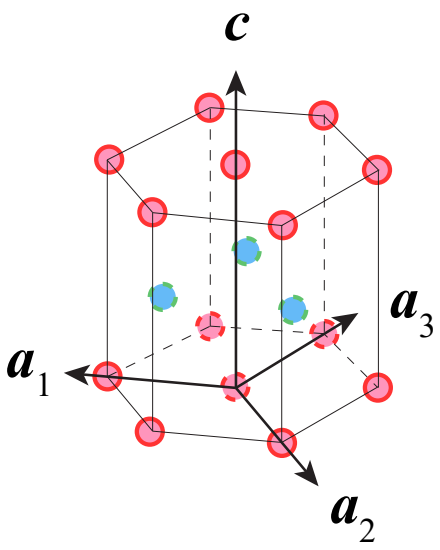

Figure 2.4: Schematic of the hexagonal close packed lattice.

$i = 1, 2, 3$, then the deformation gradient is defined by

$$F_{iJ} = \frac{\partial x_i}{\partial X_J}. \tag{2.3}$$

We will see shortly that the deformation gradient will play a key role in describing our lattice deformations such that we may obtain a twin.

Reciprocal Lattices

Since the problem of twinning is crystallographic, a mathematical notion of a *reciprocal lattice* can be conveniently be applied. In a very loose sense, the reciprocal lattice exists in reciprocal space, and can be thought of as the Fourier transform of an original, reference lattice. Examples of reciprocal lattices are shown in Figure 2.5.

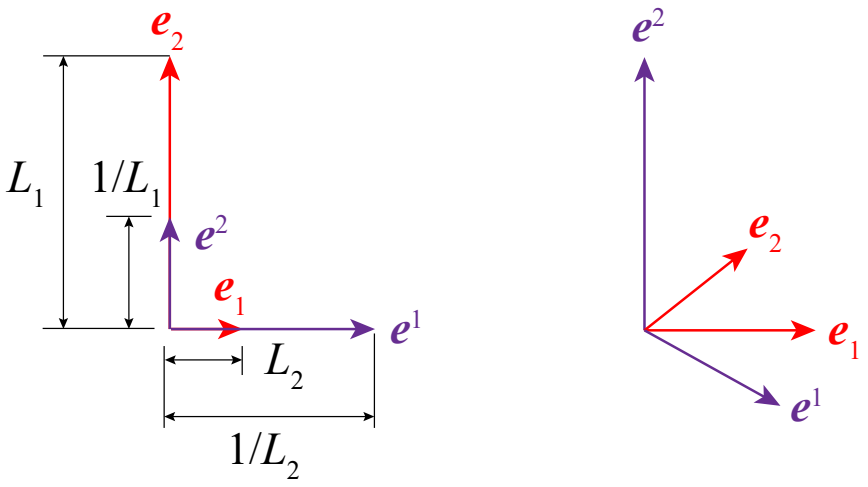

Figure 2.5: Schematic examples of reciprocal lattices.

Starting with the parent crystal lattice vectors $\boldsymbol{e})_i$, a reciprocal basis $\boldsymbol{e}^i$ can be defined by

$$\boldsymbol{e}^i = \frac{\boldsymbol{e}_j \times \boldsymbol{e}_k}{\boldsymbol{e}_i \cdot (\boldsymbol{e}_j \times \boldsymbol{e}_k)}, \tag{2.4}$$

with i, j, and k permuting. The notion of a reciprocal lattice will be especially important later when identifying the indices of the twin planes. However, it also has its immediate importance, since it allows for the definition of a deformation gradient associated with a discontinuity,

$$\boldsymbol{F} = \boldsymbol{g}_i \otimes \boldsymbol{e}^i. \tag{2.5}$$

The concept of reciprocal lattices will not only factor into the procedure for calculating kinematically-allowable twin modes, but will also be used for indexing the normals to planes and also directions, as described in Appendix A.1.

The Lattice Equivalence Metric

We will follow the notions of a *lattice equivalence metric* introduced by Friedel, Santoro, and Mighell [73–75]. A class of equivalent lattices can be reproduced by introducing a metric $\mu_i^j \in \mathrm{GL}[3, \mathbb{Z}]$, i.e. that it is a 3×3 array of integers, with $\det[\mu_i^j] = \pm 1$. In full form, for some matrix $\boldsymbol{M}$ being the matrix of scalar products of the material lattice vectors,

$$\boldsymbol{\mu}\boldsymbol{M}\boldsymbol{\mu}^{\mathrm{T}} \approx \boldsymbol{M}. \tag{2.6}$$

As summarized by Bhattacharya [117], with two sets of lattice vectors $\boldsymbol{e}_i$ and $\boldsymbol{f}_i$ with the same orientation, the same lattice is generated if, and only if,

$$\boldsymbol{f}_i = \mu_i^j \boldsymbol{e}_j. \tag{2.7}$$

The properties of μ_i^j are important because the unit determinant means that there will not be any artificial distortion of the lattice introduced merely by this crystallographic definition of the lattice, and the material identity does not change simply because of the existence of a twin plane in the crystal. Consequently, we can use μ_i^j from here forth as a means of generating lattices equivalent to the original. This will play a crucial role when we discuss the twin kinematic framework formulation.

2.3 Twinning

With the notion of lattice vectors in place, we now introduce the twin as a defect on the crystal. Consider a crystal with two distinct lattices separated by a planar discontinuity. Following the notions of [118, 119], a *twin* is a special situation where the lattice on one side of the discontinuity plane may be obtained as both a (i) rotation) and (ii) a simple shear of the lattice on the other side. A schematic of this is represented in Figure 2.6.

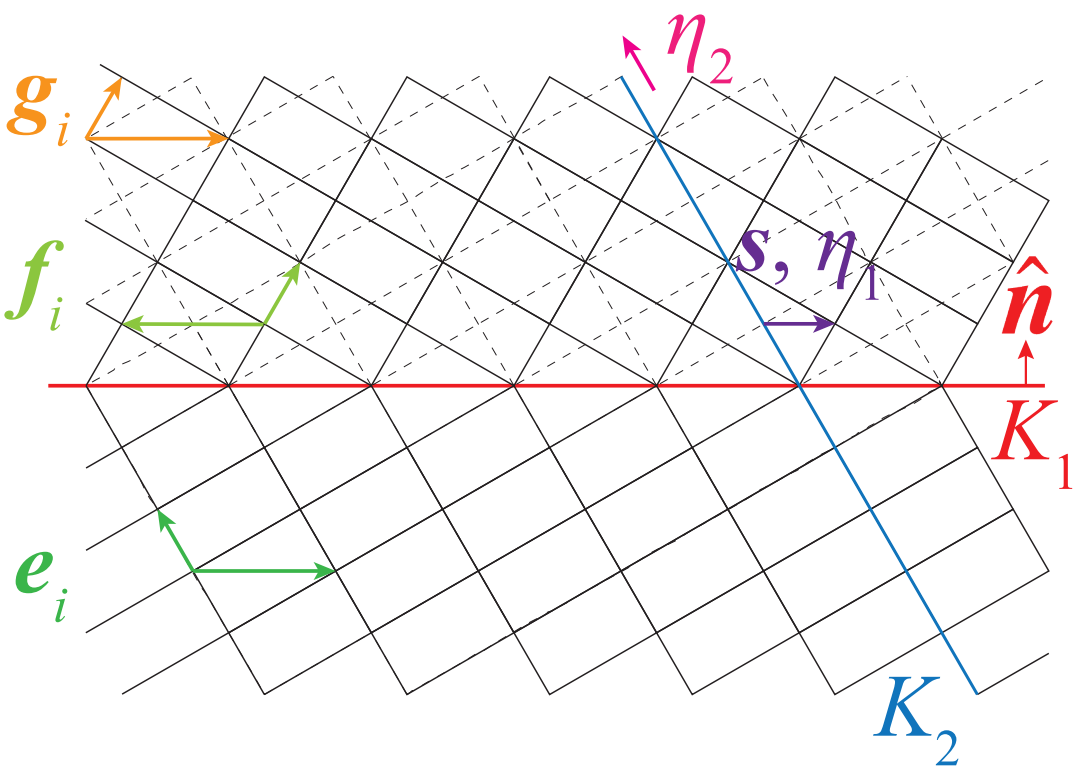

Figure 2.6: Schematic illustration of a lattice that has undergone twinning, with lattice vectors and twinning elements labeled.

As can be seen in Figure 2.6, we have the following items of interest:

- The *twin plane* (the plane of discontinuity), is described by a normal $\hat{\boldsymbol{n}}$ which is presumed to have a unit magnitude since we only need it to indicate direction. In classical literature, this is also denoted by K_1.
  - In classical theory, if K_1 is rational, then the particular twin is said to be a *type I twin*.
- In constructing the twin through the simple shear, we note that the shear vector is represented by $\boldsymbol{s}$, which also shows up as η_1 in classical works. This is known as the *twinning shear*.
- Conjugate to these the twin plane and shear direction, K_2 represents a plane which remains undistorted over the course of the twin deformation. An associated direction which remains undistorted is denoted η_2. These two quantities often show up in classical literature, but are not explicitly calculated in our formulation.
  - In classical theory, if K_2 is rational, then the particular twin is said to be a *type II twin*.
  - For the case of both K_1 and K_2 being rational, the twin is said to be a *compound twin*.
- We refer to the lattice vectors $\boldsymbol{e}_i$ as describing the *perfect crystal*, i.e. the reference material prior to twinning. Once the twin is introduced, we refer to the lattice described by $\boldsymbol{f}_i$ and $\boldsymbol{g}_i$ as the *twinned crystal*.

Now, let us develop some mathematical formalism to describe this phenomenon.

2.4 Twin Kinematic Framework

Since the goal of this investigation is to predict the *relevant* twin modes, the first task necessary is to identify all of the *possible* twin modes. This means that an exhaustive search for all of the possible twin configurations given a material's description is necessary. To surmount the challenges of describing what could (and will be shown to) be many thousands of twin modes, the aforementioned lattice-based approach, but with some variations, shall be used. Instead of the immediate assumption of two-fold rotations, this work will take the lattice vectors of a material of interest and then make use of the principles of Pitteri [83] by testing all of the possible lattice configurations on the opposing side of the planar discontinuity in order to find the ones that satisfy the twin definition by invoking calculations completed in Ball and James [85, 86].

The result of this step is the cataloging of the set of all possible twins in a material, as given by the twin normal and an effective twinning shear which reproduces the twinned configuration.

Let us follow Figure 2.6; let $\boldsymbol{e}_i$, with $i = 1, 2, 3$, be the lattice vectors of the reference crystal, while $\boldsymbol{f}_i$ and $\boldsymbol{g}_i$ be the lattice vectors of the twinned crystal. Since the twin can be constructed by rotating one side of the lattice to achieve the other, we suppose that $\boldsymbol{f}_i$ may be related to the original set of lattice vectors through a rotation $\boldsymbol{Q}$, i.e. the rotation matrix satisfies the conditions that $\det[\boldsymbol{Q}] = \pm 1$ and $\boldsymbol{Q}^{\mathrm{T}}\boldsymbol{Q} = \boldsymbol{Q}\boldsymbol{Q}^{\mathrm{T}} = \boldsymbol{\delta}$. This allows us to then write

$$\boldsymbol{f}_i = \boldsymbol{Q}\boldsymbol{e}_i. \tag{2.8}$$

However, one of the central arguments is that we can also construct the twinned crystal by applying a simple shear to the atoms; thus, we require $\boldsymbol{g}_i$ to be related to $\boldsymbol{e}_i$ through a simple shear,

$$\boldsymbol{g}_i = (\boldsymbol{\delta} + \boldsymbol{s} \otimes \hat{\boldsymbol{n}})\boldsymbol{e}_i, \tag{2.9}$$

where $\boldsymbol{\delta}$ is the identity matrix. Since $\boldsymbol{g}_i$ and $\boldsymbol{f}_i$ both represent the twinned side of the crystal, they must reproduce the *exact* same lattice, and thus must satisfy some notion of equivalence through the equivalent metric μ_i^j (see 2.2). As such, following Pitteri [83], we can say that $\boldsymbol{f}_i$ and $\boldsymbol{g}_i$ are related through

$$\boldsymbol{g}_i = \mu_i^j \boldsymbol{f}_j. \tag{2.10}$$

Thus, combining Equations (2.8)-(2.10) gives us the *twinning equation*,

$$\mu_i^j \boldsymbol{Q}\boldsymbol{e}_j = (\boldsymbol{\delta} + \boldsymbol{s} \otimes \hat{\boldsymbol{n}})\boldsymbol{e}_j. \tag{2.11}$$

Equation (2.11) admits a vast (countably infinite) space of solutions. In order to identify these solutions, we index our problem by the array μ_i^j and rearrange things such that we first fix the value of μ_i^j and then solve Equation (2.11) for $\boldsymbol{s}$ and $\hat{\boldsymbol{n}}$; we then repeat this procedure for a different μ_i^j.

For any given μ_i^j, we may define a tensor $\boldsymbol{H}$,

$$\boldsymbol{H} = \mu_i^j \boldsymbol{e}_j \otimes \boldsymbol{e}^i, \tag{2.12}$$

with $\boldsymbol{e}^i$ being the reciprocal lattice defined in Equation (2.4). Consequently, the twinning relationship given in Equation (2.11) can be rewritten as

$$\boldsymbol{F} = \boldsymbol{Q}\boldsymbol{H} = \boldsymbol{\delta} + \boldsymbol{s} \otimes \hat{\boldsymbol{n}}. \tag{2.13}$$

An associated notion of deformation is the right Cauchy-Green deformation tensor, which maintains its definition from continuum mechanics, i.e.

$$\boldsymbol{C} = \boldsymbol{F}^{\mathrm{T}}\boldsymbol{F}. \tag{2.14}$$

Since the right Cauchy-Green tensor measures actual distortion of the lattice (as opposed to the deformation gradient, which can also account for rotations), it becomes the primary quantity of interest for defining a twin. Because the twin is achieved when the lattice $\boldsymbol{g}_i$ is within a rotation of a simple shear of the lattice of the parent crystal lattice $\boldsymbol{e}_i$, a special form can be written for $\boldsymbol{C}$. Following Ball and James [85, 86], necessary and sufficient conditions for $\boldsymbol{C}$ to be written in a form consistent with simple shear[1],

$$\boldsymbol{C} = (\boldsymbol{\delta} + \hat{\boldsymbol{n}} \otimes \boldsymbol{s})(\boldsymbol{\delta} + \boldsymbol{s} \otimes \hat{\boldsymbol{n}}),$$

are that the shear $\boldsymbol{s}$ and the (unit) normal $\hat{\boldsymbol{n}}$ satisfy particular conditions. Taking an eigendecomposition of $\boldsymbol{C}$ to result in sorted eigenvalues $\lambda_1[\boldsymbol{C}] \leq \lambda_2[\boldsymbol{C}] \leq \lambda_3[\boldsymbol{C}]$, with corresponding eigenvectors $\boldsymbol{\xi}_1, \boldsymbol{\xi}_2$, and $\boldsymbol{\xi}_3$, the simple shear condition may be satisfied by requiring that $\boldsymbol{C} \neq \boldsymbol{\delta}$[2] and that the eigenvalues satisfy

$$0 \leq \lambda_1[\boldsymbol{C}] \leq \lambda_2[\boldsymbol{C}] = 1 \leq \lambda_3[\boldsymbol{C}], \tag{2.15}$$

which enforces the condition that $\boldsymbol{C} \geq \boldsymbol{0}$ and that there is no stretch in one of the principal directions, which is consistent with the notion of simple shear.

With the restriction taken, the solutions for the twin normal and twinning shear are given to be

$$\boldsymbol{s} = \rho\left(\sqrt{\frac{\lambda_3[\boldsymbol{C}](1-\lambda_1[\boldsymbol{C}])}{\lambda_3[\boldsymbol{C}]-\lambda_1[\boldsymbol{C}]}}\hat{\boldsymbol{\xi}}_1 + \kappa\sqrt{\frac{\lambda_1[\boldsymbol{C}](\lambda_3[\boldsymbol{C}]-1)}{\lambda_3[\boldsymbol{C}]-\lambda_1[\boldsymbol{C}]}}\hat{\boldsymbol{\xi}}_3\right) \tag{2.16a}$$

$$\hat{\boldsymbol{n}} = \frac{1}{\rho}\left(\frac{\sqrt{\lambda_3[\boldsymbol{C}]}-\sqrt{\lambda_1[\boldsymbol{C}]}}{\sqrt{\lambda_3[\boldsymbol{C}]-\lambda_1[\boldsymbol{C}]}}(-\sqrt{1-\lambda_3[\boldsymbol{C}]}\hat{\boldsymbol{\xi}}_1 + \kappa\sqrt{\lambda_3[\boldsymbol{C}]-1}\hat{\boldsymbol{\xi}}_3)\right). \tag{2.16b}$$

Here, $\rho \neq 0$ is a normalization constant in order to ensure that the twin normal $\hat{\boldsymbol{n}}$ maintains a unit magnitude, and $\hat{\boldsymbol{\xi}}_i$ are the *normalized* eigenvectors of $\boldsymbol{C}$ corresponding to the i^{th} eigenvalue $\lambda_i[\boldsymbol{C}]$, with $i = 1, 2, 3$, and $\kappa = \pm 1$ determines a pair of

[1] The original statement focused on necessary and sufficient conditions for $\boldsymbol{H}^{\mathrm{T}}\boldsymbol{H}$, but since $\boldsymbol{F} = \boldsymbol{Q}\boldsymbol{H}$, this is equivalent here.

[2] Examining Equation (2.15), it becomes apparent that one of the values of $\boldsymbol{C}$ that would satisfy this condition would be identity, i.e. $\boldsymbol{C} = \boldsymbol{\delta}$. This branch of solutions, however, yields a set of stacking fault solutions, which are not desired since this investigation is interested in looking at twins. Consequently, the restriction of $\boldsymbol{C} \neq \boldsymbol{\delta}$ is taken.

conjugate solutions for twins in order to be consistent with the classical notion of twin systems existing in conjugate pairs.

Looking back at Equation (2.11), it is now possible to construct the rotation matrix explicitly based on the twin elements. Reorganizing, we have

$$\boldsymbol{Q} = ((\mu_i^j)^{-1}(\boldsymbol{\delta} + \boldsymbol{s} \otimes \hat{\boldsymbol{n}})\boldsymbol{e}_i) \otimes \boldsymbol{e}^j. \tag{2.17}$$

It can be seen that the rotation matrix will satisfy the usual properties of SO[3], i.e. $\det[\boldsymbol{Q}] = 1$ and $\boldsymbol{Q}^{\mathrm{T}}\boldsymbol{Q} = \boldsymbol{\delta}$. Moreover, with the rotation matrix $\boldsymbol{Q}$ now defined, we can extract the usual angle of rotation through the relation

$$\mathrm{tr}[\boldsymbol{Q}] = 1 + 2\cos[\theta]. \tag{2.18}$$

Equation (2.18) then becomes important for compactly visualizing the results of the kinematic framework analysis.

Remark on Shuffling

We conclude by extending the discussion to non-Bravais lattices. We require that the skeletal lattice described by the unit vectors satisfy the same relations above. However, the shifts are unrestricted; this is known as *shuffling*.

2.5 Implementation: Kinematic Framework

We now quickly review the implementation of the twin kinematic framework and outline its implementation in Algorithm 2.1. Upon completion, we have all of the information that we need in order to catalog twin modes for a given material, and are able to kinematically reconstruct the atomic configurations of these twins upon demand.

Remark on the Implementation

Note that, in our discussion of the twin kinematic framework (Section 2.4), we made specific mention that the twinning equation (Equation (2.11)) had an infinite number of solutions, i.e. twin modes. This arises because of the fact that μ_i^j is not technically bounded by the values that its indices may take on, as long as the condition on $\det[\mu_i^j] = \pm 1$ is satisfied. The infinitude of the solution space also arises from the unit cells; since there are no limits on the unit cells that could be taken to describe a material — especially in the case of HCP materials — each choice leads to an infinite set of solutions!

Since this is a computationally-intractable task, our implementation seeks to find twinning solutions within a large, finite space by respecting hardware limitations (e.g.

Algorithm 2.1 Procedure for identifying possible and relevant twin modes in a given material of interest.

function IDENTIFY POSSIBLE TWINS($a, c, \boldsymbol{e}_i$) ▷ Identify all possible twin configurations.
    Identify an admissible range of μ_i^j.
    Compute the twinned lattice vectors $\boldsymbol{g}_i$.
    Compute deformation gradient $\boldsymbol{F}$ and right Cauchy-Green tensor $\boldsymbol{C}$.
    for all μ_i^j forming $\boldsymbol{C}$ satisfying Equation (2.15) **do**
        Compute the twinning shear $\boldsymbol{s}$ using Equation (2.16a).
        Compute the twinning normal $\hat{\boldsymbol{n}}$ using Equation (2.16b).
        Compute the associated rotation matrix $\boldsymbol{Q}$ using Equation (2.17).
    end for
    Store: $\boldsymbol{s}, \hat{\boldsymbol{n}}, \boldsymbol{g}_i$.
end function

memory). Consequently, truly finding *all* twin modes for a given material is presently intractable, but our work seeks to change the paradigm and show how diverse the space of twinning solutions for HCP materials is within this finite space.

2.6 Summary

In this chapter, we have developed a kinematic framework grounded on lattice theory that generates kinematically-admissible twin modes. Unlike previous works, we can now use this kinematic framework in a predictive fashion, using it to find many novel twin modes in any material of interest, as long as we are able to conjure up a set of lattice vectors to describe that material. We are now ready to implement this kinematic framework and demonstrate its potential.

Chapter 3

RESULTS: TWIN KINEMATICS

3.1 Goals of this Chapter

We now implement the techniques of Chapter 2. We start by showing the application of the implementation to several, simpler examples, including the classes of cubic materials, showing that we recover some classically-known results. We then move on and demonstrate the application of our implementation to magnesium, using two common lattice vector descriptions of it. From the resulting list of potential twin modes in magnesium, we highlight the ability of the implementation to capture classically-verified twin modes. We also demonstrate how the kinematic framework predicts a significantly larger set of possible twins than what classical literature suggests. At the end of the chapter, we also demonstrate the flexibility of this twin kinematic framework and apply it to a variety of different materials.

3.2 Examples

Before presenting the bulk results on magnesium, we illustrate the application of the kinematic framework to several, simpler examples with well-known results.

Square Lattice

Let us consider a square lattice, which can be described by inputting the lattice vectors

$$\begin{aligned} \boldsymbol{e}_1 &= [1, 0] \\ \boldsymbol{e}_2 &= [0, 1]. \end{aligned} \tag{3.1}$$

In the case of a two-dimensional material like this, the eigenvalue conditions of Equation (2.15) still hold, but since the resultant dimensionality leads to a vanishing third eigenvalue, we now have the modification that

$$\lambda_1[\boldsymbol{C}] < 1 \cup \lambda_3[\boldsymbol{C}] > 1.$$

Let's consider the particular case the metric

$$\mu_i^j = \begin{bmatrix} -1 & 0 \\ -1 & 1 \end{bmatrix}.$$

We see that $\det[\mu_i^j] = -1$ and it is an array of integers, which means that we have the conditions that we need.

From this, we form the test deformed lattice vectors $\boldsymbol{g}_i' = \mu_i^j \boldsymbol{e}_j$. Using the particular μ_i^j we have in this example, we see that we have

$$\begin{aligned}\boldsymbol{g}_1' &= \mu_1^j \boldsymbol{e}_j = [-1, -1] \\ \boldsymbol{g}_2' &= \mu_2^j \boldsymbol{e}_j = [0, 1].\end{aligned}$$

The test vectors allow us to then construct the deformation gradient,

$$\boldsymbol{F} = \begin{bmatrix} 1 & 0 \\ -1 & 1 \end{bmatrix}.$$

The right Cauchy-Green tensor is then

$$\boldsymbol{C} = \begin{bmatrix} 2 & -1 \\ -1 & 1 \end{bmatrix}.$$

The eigenvalues of this right Cauchy-Green tensor are

$$\begin{aligned}\lambda_1[\boldsymbol{C}] &= \frac{1}{2}(3 - \sqrt{5}) < 1 \\ \lambda_2[\boldsymbol{C}] &= \frac{1}{2}(3 + \sqrt{5}) > 1,\end{aligned}$$

and this is a good result because it means that we have worked out everything correctly, and the μ_i^j proposed is, indeed, consistent with our notion of a twin. With this, we can now use Equations (2.16a) and (2.16b), noting that λ_3 and $\boldsymbol{\xi}_3$ are now replaced with the second eigenvalue and second eigenvector, respectively. The eigenvectors are

$$\begin{aligned}\boldsymbol{\xi}_1 &= \left[\frac{1}{2}(\sqrt{5} - 1), 1\right] \\ \boldsymbol{\xi}_2 &= \left[-\frac{1}{2}(1 + \sqrt{5}), 1\right],\end{aligned}$$

and the consequent twinning elements are

$$\begin{aligned}\hat{\boldsymbol{n}} &= \frac{1}{\sqrt{5}}[1, -2] \\ \boldsymbol{s} &= \frac{1}{\sqrt{5}}[2, 1].\end{aligned}$$

The results of this example are shown in Figure 3.1

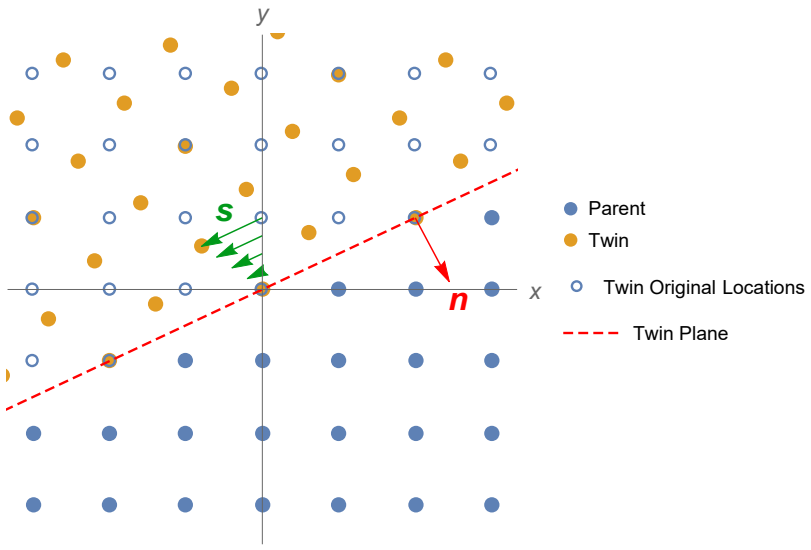

Figure 3.1: Atomic visualization for the square lattice example, with blue points representing the perfect lattice, and solid points representing the final, twinned configuration.

The Pitteri Example of Body-Centered Cubic Materials

We can make sure that our formulation also works appropriately for three-dimensional materials by validating against Pitteri's example of a body-centered cubic material [83]. In this case, we are given that the lattice vectors to test are

$$\boldsymbol{e}_1 = [d, 0, 0] \tag{3.2a}$$

$$\boldsymbol{e}_2 = [0, d, 0] \tag{3.2b}$$

$$\boldsymbol{e}_3 = \frac{1}{2}[d, d, d] \tag{3.2c}$$

and we have a metric

$$\mu_i^j = \begin{bmatrix} 1 & 0 & 0 \\ 0 & 1 & 0 \\ -1 & -1 & -1 \end{bmatrix}$$

from [83]. Our goal is to show that, if implemented correctly, the twin normal has indices

$$\hat{\boldsymbol{n}} \sim (112)$$

and the twin shear has indices

$$\boldsymbol{s} \sim [11\bar{1}]$$

We start off by making sure that μ_i^j satisfy the appropriate properties. Here, $\det[\mu_i^j] = -1$, which satisfies the conditions that we need. Thus, we then begin the task of

computing the test deformed vectors $\boldsymbol{g}_i'$, giving us that

$$\begin{aligned}\boldsymbol{g}_1' &= \mu_1^j \boldsymbol{e}_j = \frac{d}{2}[1,-1,1] \\ \boldsymbol{g}_2' &= \mu_2^j \boldsymbol{e}_j = \frac{d}{2}[-1,1,-1] \\ \boldsymbol{g}_3' &= \mu_3^j \boldsymbol{e}_j = -\frac{d}{2}[1,1,1].\end{aligned}$$

We also note that we need the reciprocal lattices in this case, which are

$$\begin{aligned}\boldsymbol{e}^1 &= \frac{\boldsymbol{e}_2 \times \boldsymbol{e}_3}{\boldsymbol{e}_1 \cdot (\boldsymbol{e}_2 \times \boldsymbol{e}_3)} = \frac{1}{d}[1,0,-1] \\ \boldsymbol{e}^2 &= \frac{\boldsymbol{e}_3 \times \boldsymbol{e}_1}{\boldsymbol{e}_1 \cdot (\boldsymbol{e}_2 \times \boldsymbol{e}_3)} = \frac{1}{d}[0,1,-1] \\ \boldsymbol{e}^3 &= \frac{\boldsymbol{e}_1 \times \boldsymbol{e}_2}{\boldsymbol{e}_1 \cdot (\boldsymbol{e}_2 \times \boldsymbol{e}_3)} = \frac{2}{d}[0,0,1].\end{aligned}$$

The deformation gradient is then

$$\boldsymbol{F} = \boldsymbol{g}_i' \otimes \boldsymbol{e}^i = \frac{1}{2}\begin{bmatrix} 1 & -1 & -2 \\ -1 & 1 & -2 \\ -1 & -1 & 0 \end{bmatrix},$$

leading to a right Cauchy-Green tensor of

$$\boldsymbol{C} = \boldsymbol{F}^{\mathrm{T}}\boldsymbol{F} = \frac{1}{4}\begin{bmatrix} 3 & -1 & 0 \\ -1 & 3 & 0 \\ 0 & 0 & 8 \end{bmatrix}.$$

Consequently, the eigenvalues of $\boldsymbol{C}$ are

$$\begin{aligned}\lambda_1[\boldsymbol{C}] &= \frac{1}{2} < 1 \\ \lambda_2[\boldsymbol{C}] &= 1 \\ \lambda_3[\boldsymbol{C}] &= 2 > 1,\end{aligned}$$

which means that we have the possibility of writing out this as a twin as we would like. The corresponding (non-normalized) eigenvectors in this case are

$$\begin{aligned}\boldsymbol{\xi}_1 &= [1,1,0] \\ \boldsymbol{\xi}_2 &= [-1,1,0] \\ \boldsymbol{\xi}_3 &= [0,0,1].\end{aligned}$$

Substituting this into Equations (2.16a) and (2.16b) with $\kappa = -1$ gives us

$$\hat{\boldsymbol{n}} = -\frac{1}{\sqrt{6}}[1,1,2]$$
$$\boldsymbol{s} = \frac{1}{\sqrt{6}}[1,1,-1].$$

The shear magnitude of $1/\sqrt{2}$ also matches expectation for BCC. We note that the result for $\hat{\boldsymbol{n}}$ gives us the identical plane to the original proposition, i.e. that our plane is symmetry-related to (112). Since we have a cubic material, we are allowed to make direct comparisons between the indices that we have obtained in Cartesian coordinates in this case with the indices that were proposed in Pitteri. Note that, for a non-cubic crystal system, the raw Cartesian coordinates that we have produced here would not be sufficient, and one would need to take additional steps before comparisons to the proposed indices in literature could be made.

The Pitteri Example of Face-Centered Cubic Materials

The example of face-centered cubic materials demonstrates how fickle these calculations can be. We will take the prescribed μ_i^j from [83][1],

$$\mu_i^j = \begin{bmatrix} 1 & 1 & 1 \\ 0 & 1 & 0 \\ 0 & -1 & -1 \end{bmatrix}.$$

However, we will take an alternative approach from what is suggested in the work, since there is strong evidence to suggest that there may be a typo in the given formulation for FCC. We will assume the traditional FCC lattice vectors

$$\boldsymbol{e}_1 = \frac{1}{2}[d,d,0] \tag{3.3a}$$
$$\boldsymbol{e}_2 = \frac{1}{2}[0,d,d] \tag{3.3b}$$
$$\boldsymbol{e}_3 = \frac{1}{2}[d,0,d]. \tag{3.3c}$$

Our goal is to show that, if implemented correctly, the twin normal has indices

$$\hat{\boldsymbol{n}} \sim (111)$$

and the twin shear has indices

$$\boldsymbol{s} \sim [11\bar{2}],$$

[1]The original Pitteri example suggested that $\mu_2^3 = -2$ instead of the -1 here, which resulted in a higher shear magnitude than what is known for FCC materials, so this is believed to be a typo.

with the tradeoff here being that this formulation will yield a higher shear magnitude than what is suggested in [83][2]. We start off by making sure that μ_i^j satisfy the appropriate properties. Here, $\det[\mu_i^j] = -1$, which satisfies the conditions that we need. Thus, we then begin the task of computing the test deformed vectors $\boldsymbol{g}_i'$, giving us that

$$\begin{aligned}\boldsymbol{g}_1' &= \mu_1^j \boldsymbol{e}_j = \frac{d}{2}[1,1,0] \\ \boldsymbol{g}_2' &= \mu_2^j \boldsymbol{e}_j = d[0,1,0] \\ \boldsymbol{g}_3' &= \mu_3^j \boldsymbol{e}_j = \frac{d}{2}[0,1,-1].\end{aligned}$$

We also note that we need the reciprocal lattices in this case, which are

$$\begin{aligned}\boldsymbol{e}^1 &= \frac{\boldsymbol{e}_2 \times \boldsymbol{e}_3}{\boldsymbol{e}_1 \cdot (\boldsymbol{e}_2 \times \boldsymbol{e}_3)} = \frac{1}{d}[1,1,-1] \\ \boldsymbol{e}^2 &= \frac{\boldsymbol{e}_3 \times \boldsymbol{e}_1}{\boldsymbol{e}_1 \cdot (\boldsymbol{e}_2 \times \boldsymbol{e}_3)} = \frac{1}{d}[-1,1,1] \\ \boldsymbol{e}^3 &= \frac{\boldsymbol{e}_1 \times \boldsymbol{e}_2}{\boldsymbol{e}_1 \cdot (\boldsymbol{e}_2 \times \boldsymbol{e}_3)} = \frac{2}{d}[1,-1,1].\end{aligned}$$

The deformation gradient is then

$$\boldsymbol{F} = \boldsymbol{g}_i' \otimes \boldsymbol{e}^i = \frac{1}{2}\begin{bmatrix} 1 & 1 & -1 \\ 0 & 2 & 2 \\ -1 & 1 & -1 \end{bmatrix},$$

leading to a right Cauchy-Green tensor of

$$\boldsymbol{C} = \boldsymbol{F}^{\mathrm{T}}\boldsymbol{F} = \frac{1}{2}\begin{bmatrix} 1 & 0 & 0 \\ 0 & 3 & 1 \\ 0 & 1 & 3 \end{bmatrix}.$$

Consequently, the eigenvalues of $\boldsymbol{C}$ are

$$\begin{aligned}\lambda_1[\boldsymbol{C}] &= \frac{1}{2} < 1 \\ \lambda_2[\boldsymbol{C}] &= 1 \\ \lambda_3[\boldsymbol{C}] &= 2 > 1,\end{aligned}$$

[2]Using the suggested lattice vectors in [83], which are based on the BCT lattice vectors, the indices of the normal and shear vectors would not be able to match the proposed FCC indices.

which means that we have the possibility of writing out this as a twin as we would like. The corresponding (non-normalized) eigenvectors in this case are

$$\begin{aligned}\boldsymbol{\xi}_1 &= [1,0,0]\\ \boldsymbol{\xi}_2 &= \frac{1}{\sqrt{2}}[0,-1,1]\\ \boldsymbol{\xi}_3 &= \frac{1}{\sqrt{2}}[0,1,1].\end{aligned}$$

Substituting this into Equations (2.16a) and (2.16b) with $\kappa = -1$ gives us

$$\begin{aligned}\hat{\boldsymbol{n}} &= \frac{1}{\sqrt{3}}[-1,1,1]\\ \boldsymbol{s} &= \frac{1}{2\sqrt{3}}[2,1,1].\end{aligned}$$

This initially looks like it might be a problem, since the indices do not match the proposed values in [83]. However, we realize that the proposed indices are only suggested as being within a symmetry operation of the true result, which means that we can check and see if our resultant system falls within the symmetry set of the proposed solution. Fortunately, we see that applying $\boldsymbol{R}_{[0,1,0]}[\pi/2]$, i.e. a rotation about $[0,1,0]$ of $\pi/2$ gives us

$$\boldsymbol{R}_{[0,1,0]}[\pi/2]\hat{\boldsymbol{n}} = \frac{1}{\sqrt{3}}[1,1,1]$$

and

$$\boldsymbol{R}_{[0,1,0]}[\pi/2]\boldsymbol{s} = \frac{1}{2\sqrt{3}}[1,1,-2].$$

We immediately see that the rotation to $\hat{\boldsymbol{n}}$ and $\boldsymbol{s}$ gives us the proposed indices, as expected. Moreover, the shear magnitude of $1/\sqrt{2}$ follows expectation for the lowest shear of FCC.

3.3 Results for Magnesium

We now explore the particular application of this work to magnesium. Up to this point, the examples that have been shown have all been for Bravais lattices. Hexagonal close-packed materials, on the other hand, are non-Bravais, and so there are multiple descriptions of the material which will be studied in this section. A visual representation of the two most popular lattice vector descriptions for magnesium are shown in Figure 3.2; further details on these vectors will be discussed in the following subsections.

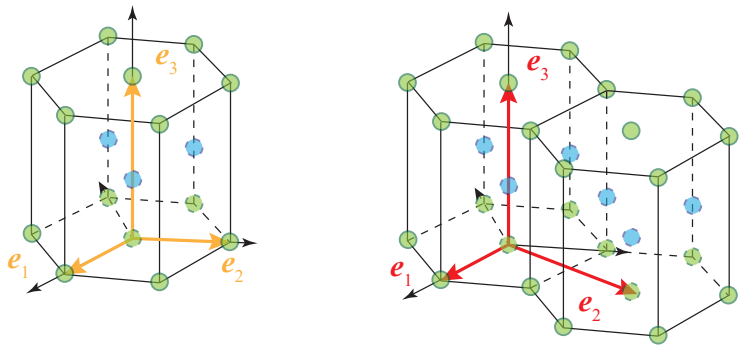

Skeletal Multilattice

Figure 3.2: The unit and the super cell used in the calculation of the potential twinning modes of magnesium along with the choice of lattice vectors.

HCP Skeletal Lattice

For the skeletal lattice, we make use of the following for input lattice vectors:

$$\boldsymbol{e}_1 = a[1, 0, 0] \tag{3.4a}$$

$$\boldsymbol{e}_2 = \frac{a}{2}[-1, \sqrt{3}, 0] \tag{3.4b}$$

$$\boldsymbol{e}_3 = [0, 0, c]. \tag{3.4c}$$

For the purposes of this initial calculation, we take

$$c/a = 1.624 \tag{3.5}$$

for magnesium[3]. We then use $|\mu_i^j| \leq 4$, giving us a total of $9^9 = 384,420,489$ lattice configurations to test; this value is chosen due to memory limitations on the devices on which this framework was implemented. We then follow the prescription of Algorithm 2.1 in order to obtain the twin elements. We then construct the rotation matrix $\boldsymbol{Q}$ following Equation (2.17), computing the rotation angle by using Equation (2.18). We plot a histogram of θ in Figure 3.3.

Note that the $+$ label refers to the branch of solutions from Equations (2.16a) and (2.16b) whereby $\kappa = +1$; similarly, the $-$ label refers to the branch of solutions with $\kappa = -1$. Figure 3.3 captures the behavior that we suspected for twinning in magnesium; that there are a considerably larger number of twin modes that are possible in the material. Fortunately, we do observe a peak in the distribution at 180°, which coincides with the notion from classical theory that twin modes are two-fold

[3]The exact c/a value will be revisited in the next chapter when energetics are explored, as the various interatomic potentials which are used to compute the twin interface energy for magnesium all yield slightly different values of c/a.

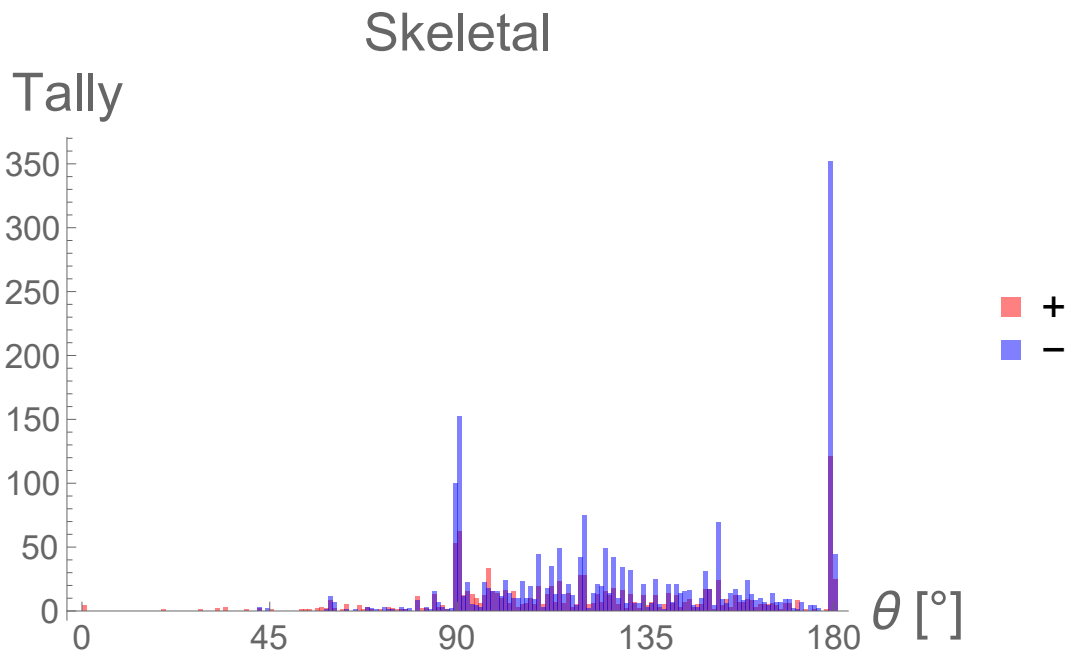

Figure 3.3: Histogram of the distribution of angles of computed twin modes for magnesium, using the skeletal lattice.

rotations; it is nice that this peak at 180° is a result that arises naturally from the framework. However, the greatest point of interest in this histogram is the fact that there are a significant number of modes which fall in the domain of rotations which would not have been considered under classical theory, with many new reorientations which still satisfy the definition of the twin.

Another method by which we can explore the computed twin modes is by examining the distribution of the shear magnitudes of all of the twin modes, since, to some extent, they portray a kinematic barrier to formation. We plot the distribution of the shear magnitudes of all of the computed twin modes in Figure 3.4[4].

Examination of Figure 3.4 gives us the same overall message as we had gathered from the histograms of the angles; in the case of HCP materials, there are a wide variety of twinning shear magnitudes, many of which form a fairly continuous distribution; this suggests that there exists a diverse landscape of twins in HCP materials.

[4]Note that, since κ does not affect the value of the shear magnitude, we will not distinguish between the $\kappa = \pm 1$ branches in these shear magnitude plots.

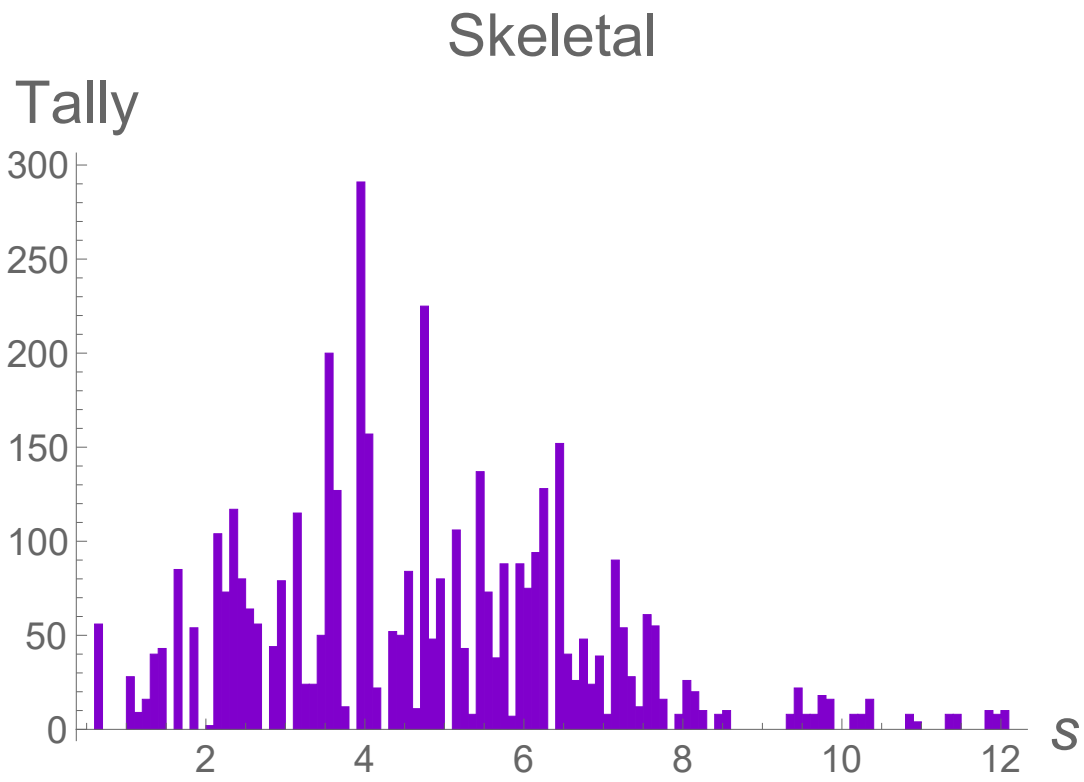

Figure 3.4: Histogram of the distribution of shear magnitudes of computed twin modes for HCP magnesium with the skeletal lattice description, with histogram bin width of 0.1.

HCP Multilattice

The multilattice construction is somewhat different; the new lattice vectors that are now inserted into the framework are

$$\boldsymbol{e}_1 = [a, 0, 0] \tag{3.6a}$$

$$\boldsymbol{e}_2 = [0, a\sqrt{3}, 0] \tag{3.6b}$$

$$\boldsymbol{e}_3 = [0, 0, c]. \tag{3.6c}$$

The construction of this lattice is considerably different; in the skeletal lattice, there is the inherent assumption that there is one shuffle $\boldsymbol{p}_1$ which which takes atoms constructed using the skeletal lattice vectors in order to recover the appropriate atomic configuration for HCP materials; here, with the multilattice construction, there is the assumption that there are three shuffles $\boldsymbol{p}_1 \ldots, \boldsymbol{p}_3$ in order to recover the correct configuration. This is fundamentally necessary due to the fact that Equations (3.6a)-(3.6c) set up a supercell that is twice the size of a standard hexagonal lattice. For consistency, we will again assume $c/a = 1.624$ for magnesium, and then insert these lattice vectors into the kinematic framework (Algorithm 2.1) with $|\mu_i^j| \leq 4$.

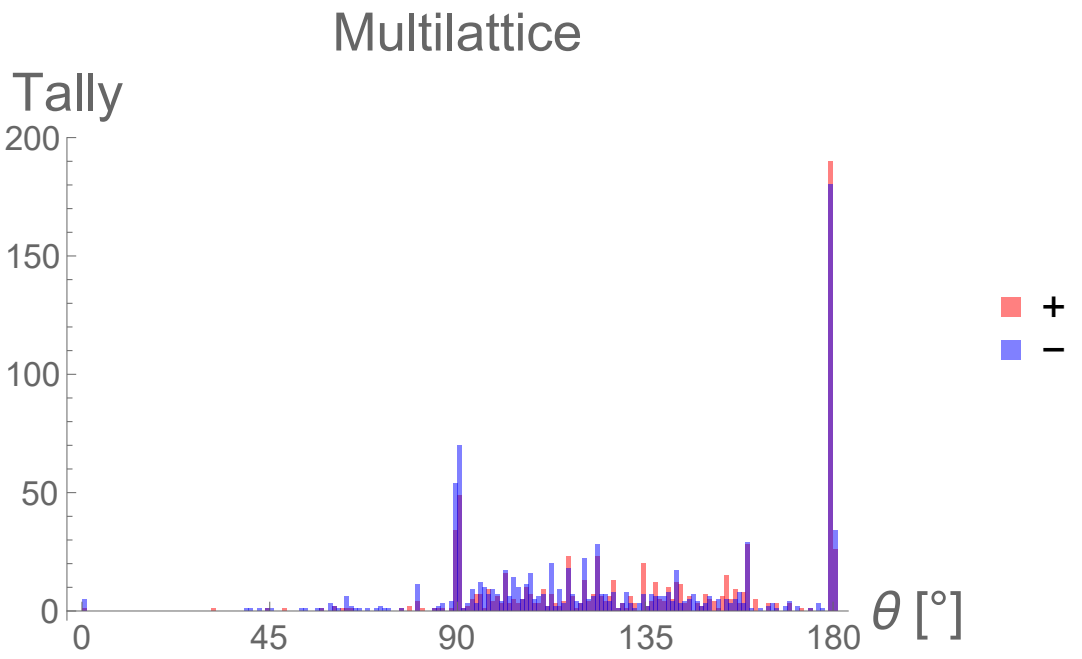

Figure 3.5: Histogram of the distribution of angles of computed twin modes for magnesium, using the multilattice.

Once more, we observe that there is a peak in the histogram at 180°, which means that, even though we have changed our lattice vector description, we are still capturing classical theory as a natural result of the formulation. It should be noted, though, that there are some changes in the actual shape of the distribution relative to Figure 3.3 due to this change in the lattice vectors.

We also generate a histogram of the shear magnitudes of the twin modes computed with the multilattice set and display the results in Figure 3.6. Inspection of this histogram repeats the notion that we had obtained with the skeletal lattice set that the landscape for twinning in HCP materials is very diverse, again, due to the nearly-continuous nature of the distribution of shear magnitudes observed for the predicted twin modes.

Comparisons Between Lattice Descriptions

We now take a brief moment to examine the differences between the skeletal lattice and multilattice descriptions of HCP magnesium. These differences are most evident when one examines the shear magnitudes. In Table 3.1, we tabulate the shear magnitudes for several important cases. In the first row, we display the minimum shear magnitude of all of the twin modes obtained from our calculation. In the next two rows, we display the shear magnitudes computed for the tension and compression twins, respectively.

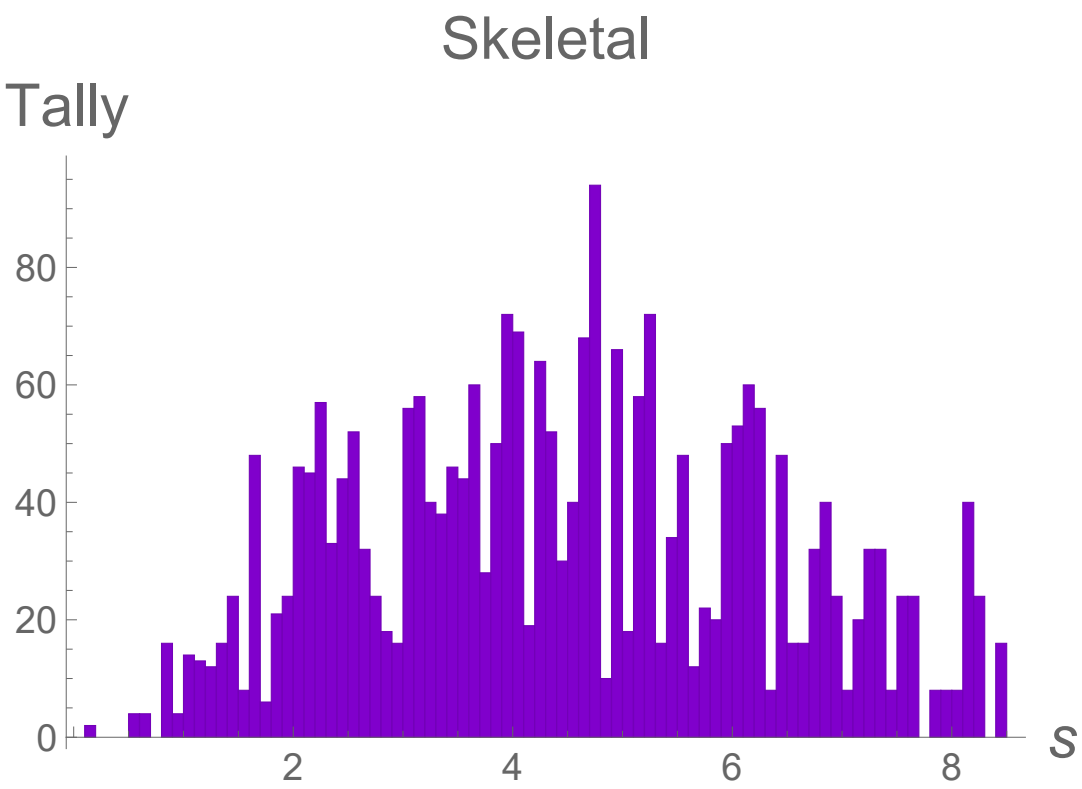

Figure 3.6: Histogram of the distribution of shear magnitudes of computed twin modes for HCP magnesium with the multilattice description, with histogram bin width of 0.1.

In the final row, we display the shear magnitude of a twin mode with an irrationally-indexed plane with the lowest twinning shear magnitude.

	Skeletal Lattice	Multilattice
s_{min}	0.616	0.129
$s_{\text{compression}}$	1.309	0.844
s_{tension}	1.688	0.129
$s_{\text{irrational}}$	1.493	0.854

Table 3.1: Tabulated values of shear magnitudes for several twin modes of interest, calculated using both the skeletal lattice and multilattice descriptions of HCP magnesium.

The values obtained in Table 3.1 reflect a trend that is also observed when comparing Figures 3.4 and 3.4; despite the unified message that the twin modes in HCP magnesium are numerous and distributed across the domain of shear magnitudes, the shear magnitudes obtained using the skeletal lattice description always tend to be higher

than the shear magnitudes obtained for equivalent modes in the multilattice description of the material. In the histograms, we see that the domain of shear magnitudes is considerably larger for the skeletal lattice results, despite the fact that the same bounds for $|\mu_i^j| \leq 4$ are used in both cases. Another illustrative example of this is the fact that, under the multilattice description, the famed tension twin has the lowest shear magnitude of all of the twin modes computed; on the other hand, in the skeletal lattice, other modes are computed to have lower shear magnitudes.

As mentioned earlier, there are also some changes in the exact shape of the distribution when we switch from the skeletal lattice description to the multilattice description. One would expect that, for additional multilattice combinations — perhaps ones with larger unit cells and, thus, larger accompanying shuffles — that one could continue to change the distribution of both the orientations and the shear magnitudes.

The comparisons between the skeletal and multilattice descriptions are the primary motivation for the remainder of our investigation and subsequent introduction of energetics into our calculations. As we see here, the sensitivity of the shear magnitude predicted from the kinematic framework means that we cannot solely depend on the twinning shear magnitude as the metric for the likeliness to visualize any particular twin mode.

3.4 Results for Additional Materials

One of the significant benefits of using this kinematic framework is the ability to study a variety of materials without any changes to the formulation beyond adjustments to the material lattice parameters and also the lattice vectors being used to describe the material. Consequently, we will now illustrate some further applications of the twin kinematic framework to materials other than magnesium.

BCC Materials

We use the lattice vectors shown in Equations (3.2a)-(3.2c) and apply Algorithm 2.1. We then plot θ from Equation (2.18) in Figure 3.7.

It is interesting to note that the BCC twin kinematic landscape is also very diverse, with many twins of non-classical orientations being predicted from the framework. However, the differentiation arises when we examine the distribution of the twinning shear magnitudes. As seen in Figure 3.8, the shear magnitudes for BCC materials are at much more discrete values. Furthermore, compared to HCP descriptions, we see that the shear magnitudes are also considerably higher. This is consistent with

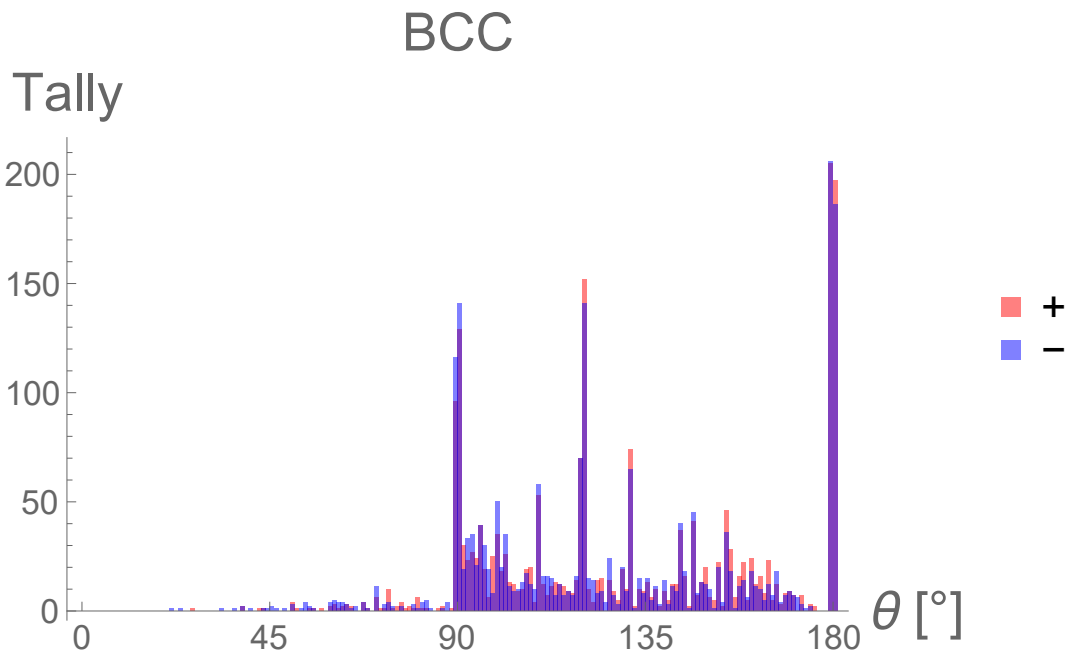

Figure 3.7: Histogram of the distribution of angles of computed twin modes for BCC materials.

the classical notion that twinning is not as prevalent a mechanism in BCC materials compared to HCP materials.

It should be noted that the insensitivity of the kinematic framework to the values of the lattice parameter itself mean that the modes obtained here can be universally applied to all BCC materials.

FCC Materials

We use the lattice vectors shown in Equations (3.3a)-(3.3c) and apply Algorithm 2.1. As before, we plot θ from Equation (2.18) in Figure 3.9.

Similar to the case for BCC, FCC materials also tend to twin along the lines of what classical theory would predict, somewhat more so than BCC materials, as denoted by the greater concentration of predicted twins at 90° and 180°. However, there are still additional modes that appear at non-classical orientations which would merit additional further investigation. Like we did for the materials before, plot the distribution of the shear magnitudes for all of the twin modes predicted for FCC materials in Figure 3.10. In observing the histogram, we note that, much like for BCC, in FCC, the shear magnitudes are also fairly discrete and are also considerably higher in magnitude than the typical shear magnitudes seen for HCP materials. This

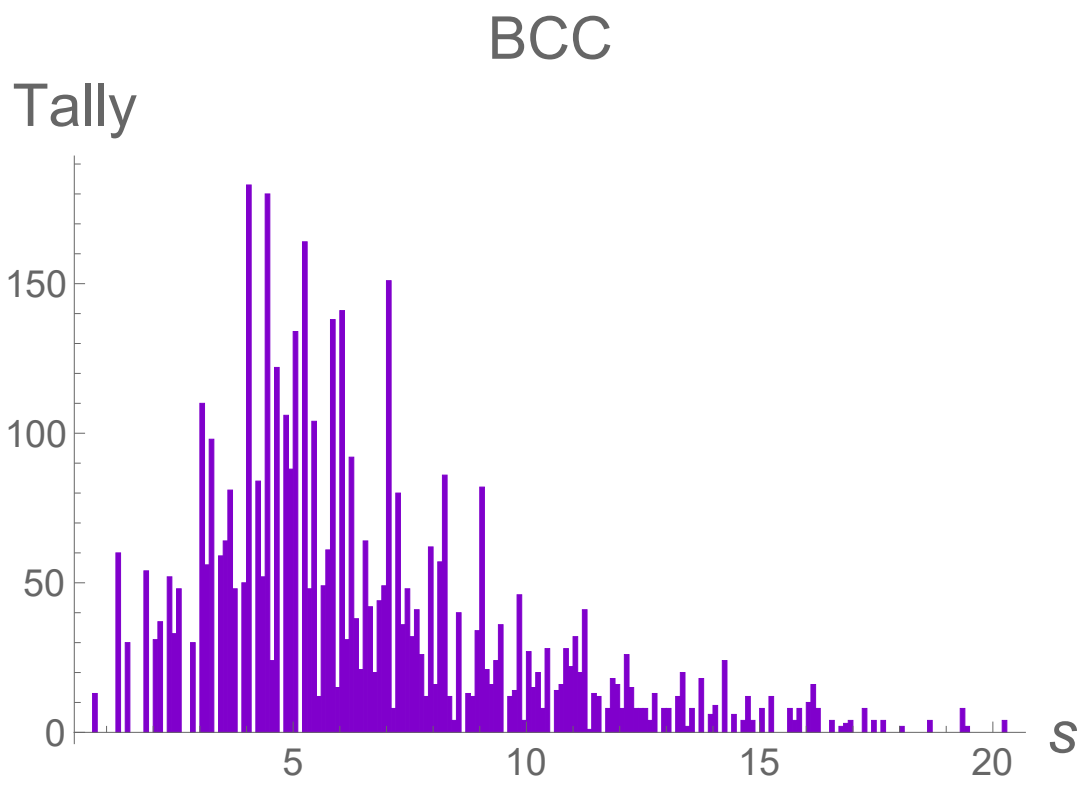

Figure 3.8: Histogram of the distribution of shear magnitudes of computed twin modes for BCC materials, with histogram bin width of 0.1.

is also consistent with the classical notion that twin modes are not too prevalent in FCC materials!

Once again, it should be noted that the insensitivity of the kinematic framework to the values of the lattice parameter itself mean that the modes obtained here can be universally applied to all FCC materials.

Additional HCP Materials

To apply the framework to additional HCP materials, we use the same base skeletal lattice vectors, shown in Equations (3.4a)-(3.4c), and the same base multilattice lattice vectors, shown in Equations (3.6a)-(3.6c), and change the c/a ratio in order to simulate the changing of materials. We then apply Algorithm 2.1. Once more, we plot θ from Equation (2.18), except we now examine the detail in Figure 3.11 through a smoothed histogram.

We only show a few examples of materials with different c/a values which are near that of magnesium. 1.6232 is chosen because it is a c/a ratio that arises out of one of the interatomic potentials that we will later use to investigate the energetics of the

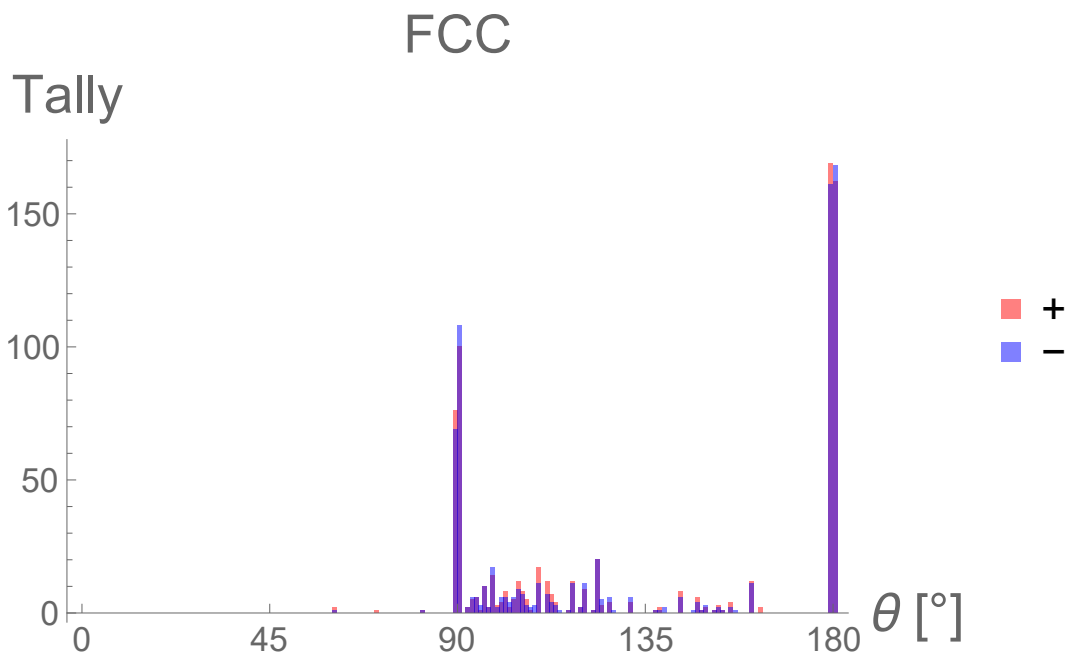

Figure 3.9: Histogram of the distribution of angles of computed twin modes for FCC materials.

various twin modes in magnesium; 1.624 is chosen because it is the experimental value of the c/a ratio for magnesium; $\sqrt{8/3}$ is chosen because it is the so-called "ideal" c/a ratio for HCP materials. The actual changes in the c/a ratios between these three is very small; however, we can see that, for both the skeletal lattice and multilattice descriptions, there are some small differences in the distributions of the orientations that are seen for the various twin modes. In all cases, a peak at 180°, corresponding to the set of solutions which are two-fold rotations, is still observed, but there are shifts in the intermediate distributions, indicating that the twinning picture remains diverse for additional HCP materials.

It is, however, also possible to conduct this study for a significantly larger range of c/a ratios. We first conduct the investigation using the set of skeletal lattice vectors (Equations (3.4a)-(3.4c)). Applying Algorithm 2.1 and then plotting θ from Equation (2.18) in a smoothed histogram form, we obtain Figure 3.12.

Figure 3.12 illustrates some considerable shifts in the dominance of twin modes as the c/a ratio changes from $c = a$ to $c = 2a$. In all cases, there is still a prevalence of potential twin modes at the usual rational-fold rotation points, but there is a significant amount of shifting for the orientation in between, suggesting that different materials of drastically different c/a ratios might experience some drastically different twin modes.

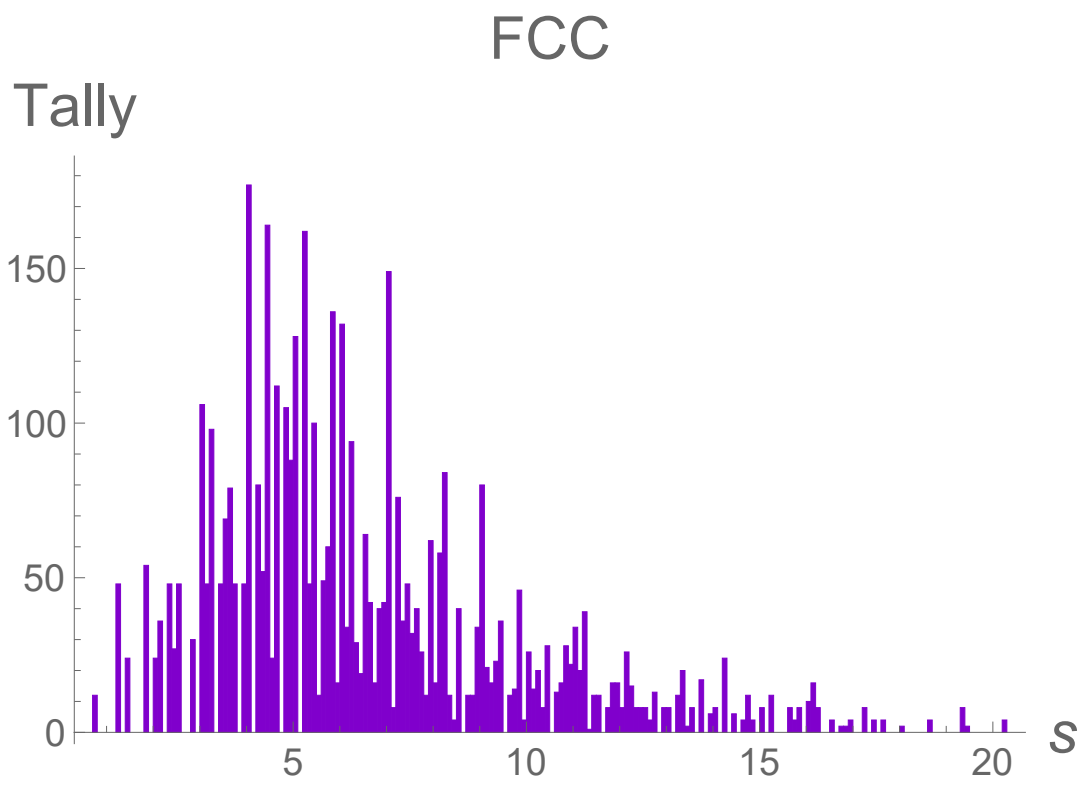

Figure 3.10: Histogram of the distribution of shear magnitudes of computed twin modes for FCC materials, with histogram bin width of 0.1.

The procedure was repeated using the multilattice vectors (Equations (3.6a)-(3.6c)) and the results are shown in Figure 3.13

Although the specific distributions obtained using the multilattice description are quite different, the overall message remains that the twins with more interesting orientations shift drastically as the c/a ratio is changed. The large range of c/a ratios investigated here may yet play an important role in upcoming studies of alloyed materials, as introducing solute elements is shown to affect the overall c/a ratio of these materials. Consequently, the shift in the twin modes observed as the c/a ratio changes may play a role in determining which modes appear in magnesium (and other) alloys.

3.5 Summary

Our implementation of the kinematic framework started off by considering some simple examples; we showed a visual example for a square lattice of an example configuration predicted from the framework. We then also demonstrated how the framework could be used to capture classical results from Pitteri [83]. We then used the framework to predict modes in BCC, FCC, and HCP materials. In each of these

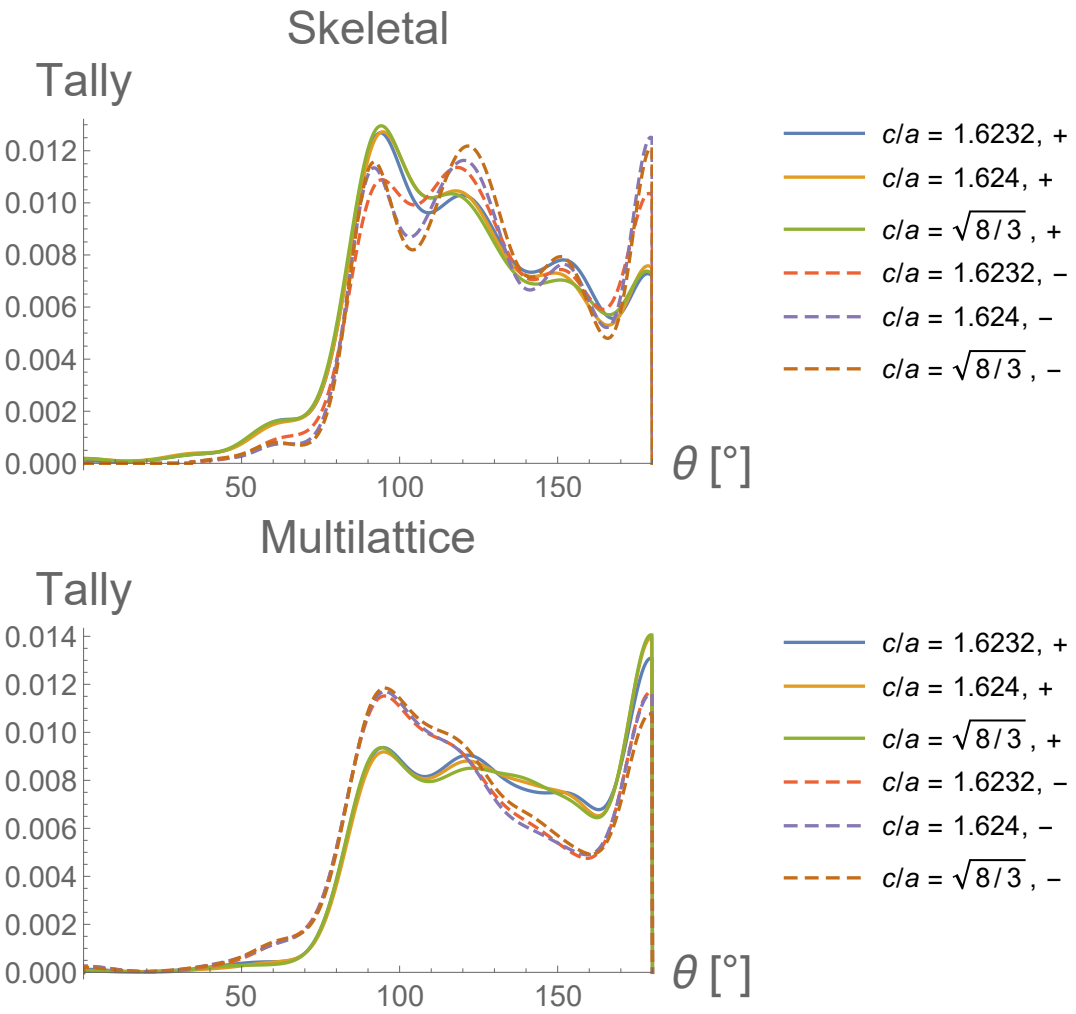

Figure 3.11: Smoothed histograms of angular distributions for various values of c/a.

cases, we saw that there were a variety of different modes that classical theory would have missed altogether, as they were not necessarily two-fold rotations of the lattice! We then saw how the picture for HCP is quite complicated, as the multiple lattice descriptions yielded different twinning shear magnitudes and twin modes. For HCP materials, we also saw how the c/a ratio change could drastically affect the twin mode distribution as well. All of this motivates us to explore the energetics of each of these kinematically-admissible twin systems.

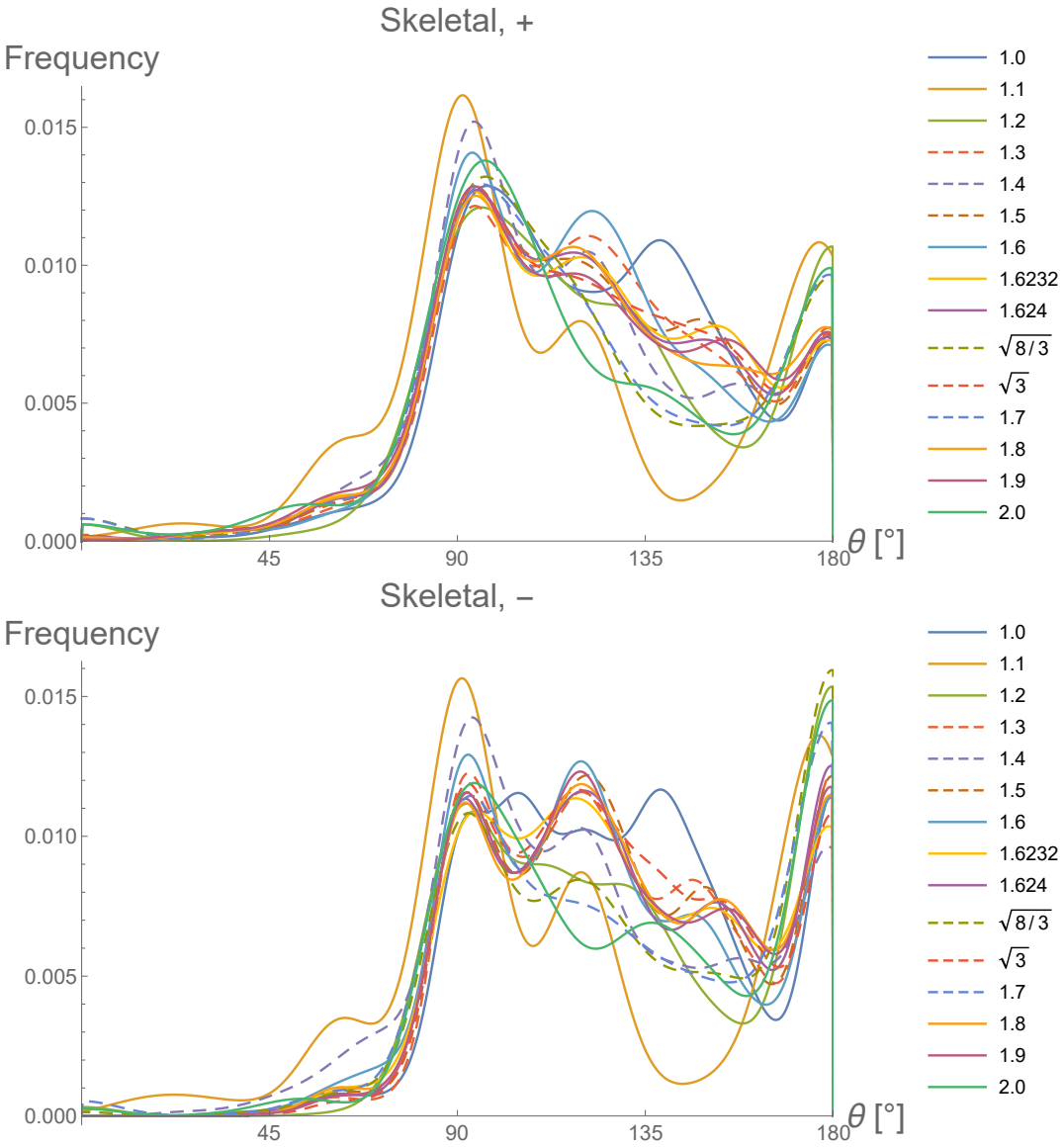

Figure 3.12: Smoothed histograms of angular distributions for a larger range of c/a values using the skeletal lattice description.

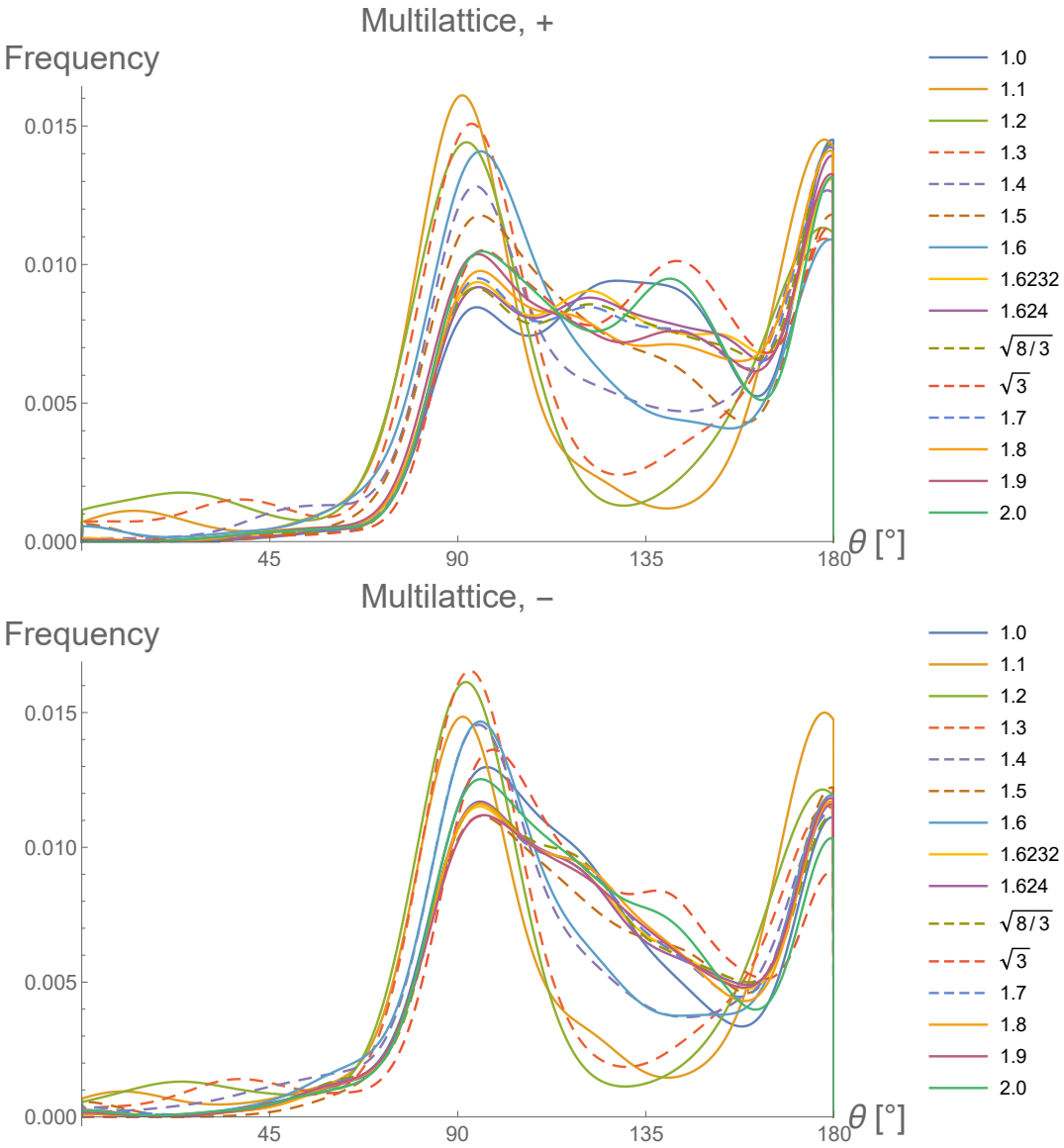

Figure 3.13: Smoothed histograms of angular distributions for a larger range of c/a values using the multilattice description.

Chapter 4

TWIN ENERGETICS

4.1 Goals of the Energetics Calculations

We now study the configurations predicted in the kinematic framework and how they compare to each other in terms of energetics. The reasoning behind this is that, if a twinned configuration and the perfect crystal have a low difference in energy, then i should not take too much in order for the twin to be visualized in some kind of a setting. Understanding the energetic difference between the perfect crystal and the twin configuration, however, is not sufficient by itself, since, in the transition states between the two endpoints, an enormous energetic barrier would also act as a deterrence to the formation of that twin. As such, this barrier must be considered in order to achieve a complete picture of the energetics governing the likeliness of a twin formation.

To this end, we set out on a three-step procedure in order to examine a full picture of the energetics behind all of the twin configurations. We assume the twin configurations from Chapter 2 as inputs in this section. Since this set of data is likely to be extremely large, we need to first use some kind of a fast, yet reasonably accurate screening technique in order to gain an estimate on the energetic landscape of the complete set of predicted twins. As the technology for conducting this large volume of calculations accurately using density functional theory is not yet in place, we turn to the execution of a series of calculations on the complete set of twins in LAMMPS using molecular statics — that is, we compute a set of energy minima at 0 K and report those values.

Unfortunately, the interatomic potentials used as the basis of molecular statics calculations are calibrated to some particular problem of interest. In this particular case, most of the twin potentials for magnesium have been calibrated for fracture behavior in magnesium, with accurate calculation of the energy of the $\{10\bar{1}2\}\langle 10\bar{1}1\rangle$ twin being a bonus. Since our goal is to move beyond this domain and calculate energy for a significantly larger set of twins, many of which have not been previously considered, we need to ensure that the values we end up seeing in molecular statics are accurate to some sense. To achieve this, we compare some twin interface energy values for known twins against previous computations from density functional theory. Once a satisfactory degree of agreement between our molecular statics and prior density

functional theoretical results is attained, we will proceed in calculating energies of new twins with some degree of confidence in our results.

Finally, since the barriers to formation also need to be considered, a discussion of the nudged elastic band technique is carried out. This technique aims to produce a series of replicas — steps between the perfect crystal and the twinned state — which are then subjected to energetic calculations, giving us a picture of the energetics of the steps between the perfect crystal and the twin configuration.

4.2 Background on Molecular Statics and Dynamics

The primary concept we will be examining is the notion of *molecular dynamics*, whose zero-temperature variant is known as *molecular statics*. Details on the earliest formulations of this can be found in [120–123] and are reviewed in [124]. For additional information on the separation of length scales inherent to the molecular dynamics/statics problem, please consult Appendix A.4.

General Concepts of Molecular Statics and Dynamics

Let's suppose that we are interested in a set of atomic nuclei, which are located at $\boldsymbol{q} = \{\boldsymbol{q}_1, \ldots, \boldsymbol{q}_n\}$ and have the momenta $\boldsymbol{p} = \{\boldsymbol{p}_1, \ldots, \boldsymbol{p}_n\}$. Molecular dynamics and molecular statics are interested in finding the configurations of these nuclei and treat them in a very classical sense. The Hamiltonian operator for this problem is then

$$\mathscr{H} = \sum_{i=1}^{n} \frac{\|\boldsymbol{p}_i\|^2}{2m_i} + \mathsf{V}[\boldsymbol{q}], \tag{4.1}$$

where $\mathsf{V}[\boldsymbol{q}]$ is an *interatomic potential*, a term which captures all of the electronic interactions and is the key to determining the energy of the configuration. Being that we are operating within classical mechanics, *Hamilton's equations of motion*,

$$\begin{cases} \dot{\boldsymbol{q}} = \dfrac{\partial \mathscr{H}}{\partial \boldsymbol{p}} \\ \dot{\boldsymbol{p}} = -\dfrac{\partial \mathscr{H}}{\partial \boldsymbol{q}} \end{cases}. \tag{4.2}$$

Note that Equation (4.2) is very similar to the standard equation for force balance from classical mechanics,

$$m\ddot{\boldsymbol{q}} = -\frac{\partial \mathsf{V}}{\partial \boldsymbol{q}}[\boldsymbol{q}] = \boldsymbol{f}[\boldsymbol{q}], \tag{4.3}$$

which measures the force on any given atom. This is the essence of molecular dynamics; we solve this force balance relation of Equation (4.3), subject to the

boundary conditions that are relevant to us. In molecular statics, we simplify the problem at hand because we are reduced to only looking at the equilibrium problem, i.e.

$$\frac{\partial \mathsf{V}}{\partial \boldsymbol{q}} = \mathbf{0}. \tag{4.4}$$

The main point of interest now is to find a suitable interatomic potential to model our system, which we will discuss in the next section.

The Embedded Atom Method

An important interatomic potential from which much of our work on energetics derives is the *embedded atom method potential*, which is also identified as the *EAM potential*. Developed by Sun *et al.* [125], this potential has the overall form

$$\mathsf{V}_i[\boldsymbol{q}] = \frac{1}{2}\sum_j \Phi[r_{ij}] + \mathsf{U}[\rho_i], \tag{4.5}$$

where $\Phi[r_{ij}]$ describes the pair interaction between two atoms of interest and $\mathsf{U}[\rho_i]$ is an *embedding function*, i.e. it measures the energy to move a nucleus from infinity to some position of relevance, whilst accounting for the interaction with electrons already in the vicinity. Note that it is inherently assumed that $\rho_i = \sum_j f[r_{ij}]$, i.e. that the electron density depends on the distance to all other atoms r_{ij}.

The introduction of Equation (4.5) allows for the computing of forces on each of the atoms. We will make use of the relation that

$$\sum_{i,j}[\cdot]\frac{\partial r_{ij}}{\partial \boldsymbol{q}_k} = \sum_{i,j}[\cdot]\frac{\boldsymbol{r}_{ij}}{r_{ij}}(\delta_{ik}-\delta_{jk}) = \sum_{i,j}[\cdot]_{ij}\hat{\boldsymbol{r}}_{ij}(\delta_{ij}-\delta_{jk}).$$

Taking advantage of the fact that $\boldsymbol{r}_{ij} = -\boldsymbol{r}_{ji}$ and that $r_{ij} = r_{ji}$, the force on the k^{th} atom with the EAM potential can then be by going through the calculation below to arrive at Equation (4.6), with $\hat{\boldsymbol{r}}_{jk} = \boldsymbol{r}_{jk}/r_{jk}$ being the unit vector between atoms j and k.

$$
\begin{aligned}
\boldsymbol{f}_k &= -\frac{\partial \mathsf{V}}{\partial \boldsymbol{q}_k} \\
&= -\left(\frac{1}{2}\sum_{i,j\in\mathscr{L}} \dot{\Phi}[r_{ij}] + \sum_{i\in\mathscr{L}} \dot{U}[\rho_i] \sum_{j\in\mathscr{L}} \dot{f}[r_{ij}]\right) \frac{\partial r_{ij}}{\partial \boldsymbol{q}_k} \\
&= -\left(\frac{1}{2}\sum_{i,j\in\mathscr{L}} \dot{\Phi}[r_{ij}] + \sum_{i\in\mathscr{L}} \dot{U}[\rho_i] \sum_{j\in\mathscr{L}} \dot{f}[r_{ij}]\right) \frac{\boldsymbol{r}_{ij}}{r_{ij}}(\delta_{ik} - \delta_{jk}) \\
&= -\left(\frac{1}{2}\sum_{j\in\mathscr{L}} \dot{\Phi}[r_{jk}] + \dot{U}[\rho_k] \sum_{j\in\mathscr{L}} \dot{f}[\boldsymbol{r}_{jk}]\right) \frac{\boldsymbol{r}_{kj}}{r_{jk}} \\
&\quad + \left(\frac{1}{2}\sum_{i\in\mathscr{L}} \dot{\Phi}[r_{ik}] + \sum_{i\in\mathscr{L}} \dot{U}[\rho_i] f[r_{ik}]\right) \frac{\boldsymbol{r}_{ik}}{r_{ik}} \\
&= \left(\sum_{j\in\mathscr{L}} \dot{\Phi}[r_{jk}] + (\dot{U}[\rho_j] + \dot{U}[\rho_k]) \sum_{j\in\mathscr{L}} \dot{f}[r_{jk}]\right) \hat{\boldsymbol{r}}_{jk}. \qquad (4.6)
\end{aligned}
$$

Note that, although the summations are technically implied to be over the lattice $\mathscr{L}$, in reality, when implemented, only atoms within some cutoff radius r_{cutoff} are summed over for the purposes of calculating the force.

Further details for the implementation of this potential are found in [125] itself; the remainder of the task involves calibrating a variety of parameters for the interatomic potential so that certain target material parameters — such as the lattice constant a or the material elastic constants — are acceptably close to other target values which are obtained either experimentally or from first principles calculations.

Additional Interatomic Potentials

Naturally, there are other choices of potentials that can be made. For instance, the *MEAM* (*modified embedded atom method*) potential extends the EAM potential by including the effects of angular forces. While greater accuracy in modeling is achieved, computational cost of such potentials is considerably higher. Many other interatomic potentials exist; we will not discuss them further since they all seek tradeoffs between accuracy and computational cost.

4.3 Interatomic Potential Training

Now that we have discussed the importance of the interatomic potential in molecular statics calculations, we will outline the steps necessary in order to simulate our

collection of novel twin modes with reasonable accuracy. Accurate determination of lattice parameters — a and c in the case of HCP materials — is usually of paramount importance in the calibration of interatomic potentials. Consequently, the first task with any interatomic potential is to perform some calibration with perfect crystal samples in order to find the relaxed lattice parameters a and c. Additional details can be found in Baskes [126] and Daw and Baskes [127]. The confirmation of these optimal parameters then allows for us to compute the *cohesive energy* of the perfect crystal, E_0^{pc}. More importantly for us, the values of a and c will matter because, for any given interatomic potential with optimal a and c, we will need to use the ratio of the two for the c/a input into the twin kinematic framework!

4.4 Twin Interface Energy

The natural measure of energy that would be computed in these twin energetics simulations would be the potential energy of a relaxed system. However, since each one of the twin configurations yields a simulation which may have a different number of atoms, directly computing the energy of the configuration might not provide us with much insight as to which systems are actually more energetically favorable than others. To work around this, we need to define a new measure that will give us insight on which interfaces are energetically favorable and which ones are not. To this end, we introduce the twin interface energy density,

$$\gamma^{\text{tw}} = \frac{\mathsf{E}^{\text{tw}} - \mathsf{E}_0^{\text{pc}} n_{\text{atoms}}}{A_{\text{interface}}}, \tag{4.7}$$

where E^{tw} is the energy of the twinned configuration, n_{atoms} is the number of atoms in the simulation, and $A_{\text{interface}}$ is the area of the twin interface. We will thus measure the energy of the various twin configurations E^{tw}, and then normalize it by the per-atom cohesive energy of the perfect crystal, E_0^{pc}, and the area of the twin interface, $A_{\text{interface}}$ in order to produce a reasonably normalized metric of the energy of each of the systems, thus providing us with a more true representation of how energetically favorable each of the twin systems is.

4.5 The Method of Nudged Elastic Band

Finding γ^{tw} is a useful measure of the energetic contribution of the twin, but it does not quite tell the whole picture, since it is only technically measuring the energies at the two endpoints of a reaction trajectory. What happens to the energy of the configuration in those transient steps is also important to understanding the likeliness of a twin to form, since, should the energetic barrier in the intermediate steps be too

high, one would imagine that this would make a particular twin mode significantly less likely to form and, thus, be exploited. As such, we employ the *nudged elastic band* technique, whereby we introduce a series of replicas which represent various steps along a minimum energy path between the perfect crystal state and the twinned configuration, which are taken to be the two endpoints.

We will now briefly review the original formulation of the nudged elastic band technique; further details about potential improvements can be found in [128–130]. For these calculations, we suppose that we have $N + 1$ images — or *replicas* — at positions $[\boldsymbol{R}_0, \boldsymbol{R}_1, \ldots, \boldsymbol{R}_N]$, with endpoints $\boldsymbol{R}_0$ and $\boldsymbol{R}_N$. The endpoints are fixed by the minimized configurations of the initial and final states; in our particular case, this involves the perfect crystal and twinned configurations. The $N - 1$ replicas in the middle of the reaction coordinate path are the objective for minimization in our calculation; all are effectively connected by elastic springs. This is schematically represented in Figure 4.1.

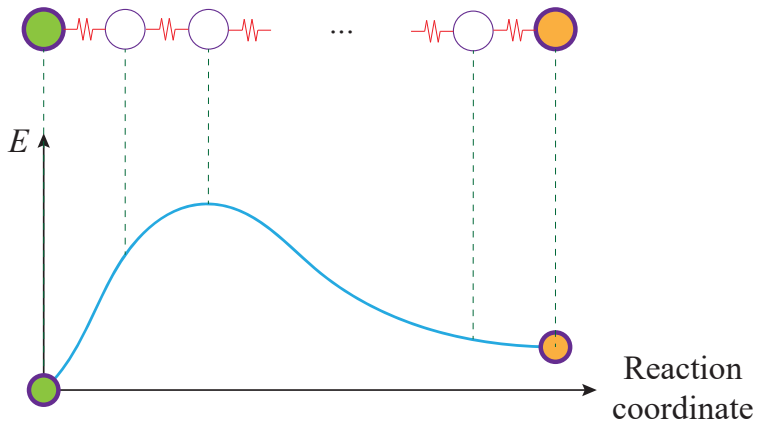

Figure 4.1: Schematic illustration of nudged elastic band replicas, with energy measurements along the reaction coordinate.

To construct a tangent at the i^{th} replica, $\boldsymbol{\tau}_i$, we make use of the two replicas adjacent to it, i.e.

$$\hat{\boldsymbol{\tau}}_i = \frac{\boldsymbol{R}_{i+1} - \boldsymbol{R}_{i-1}}{\|\boldsymbol{R}_{i+1} - \boldsymbol{R}_{i-1}\|}. \tag{4.8}$$

An alternative approach to Equation (4.8) would be to bisect the two images through

$$\boldsymbol{\tau}_i = \frac{\boldsymbol{R}_i - \boldsymbol{R}_{i-1}}{\|\boldsymbol{R}_i - \boldsymbol{R}_{i-1}\|} + \frac{\boldsymbol{R}_{i+1} - \boldsymbol{R}_i}{\|\boldsymbol{R}_{i+1} - \boldsymbol{R}_i\|} \tag{4.9}$$

and then subsequently obtain the normalized tangent through $\hat{\boldsymbol{\tau}} = \boldsymbol{\tau}_i / \|\boldsymbol{\tau}_i\|$. Equation (4.9) ensures that, for uniform springs between all replicas, the replicas will be reasonably uniformly distributed. The force acting on the i^{th} replica can be decomposed

into a tangent and perpendicular contribution,

$$\boldsymbol{F}_i = (\boldsymbol{F}_i^{\mathrm{s}})_{\parallel} - (\nabla V[\boldsymbol{R}_i])_{\perp}, \tag{4.10}$$

with

$$(\nabla V[\boldsymbol{R}_i])_{\perp} = \nabla V[\boldsymbol{R}_i] - \nabla V[\boldsymbol{R}_i] \cdot \hat{\boldsymbol{\tau}}_i,$$

and the spring force is of the form

$$(\boldsymbol{F}_i^{\mathrm{s}})_{\parallel} = (\boldsymbol{F}_i^{\mathrm{s}} \cdot \hat{\boldsymbol{\tau}}_i)\hat{\boldsymbol{\tau}}_i,$$

which, in one of the simpler formulations of the nudged elastic band, might take on a form like[1]

$$\boldsymbol{F}_i^{\mathrm{s}} = k(\|\boldsymbol{R}_{i+1} - \boldsymbol{R}_i\| - \|\boldsymbol{R}_i - \boldsymbol{R}_{i-1}\|)\hat{\boldsymbol{\tau}}_i.$$

A visual representation of the forces is provided in Figure 4.1. The idea of the nudged elastic band procedure is to then minimize the forces so that the replicas then lie on what is treated as a minimum energy path.

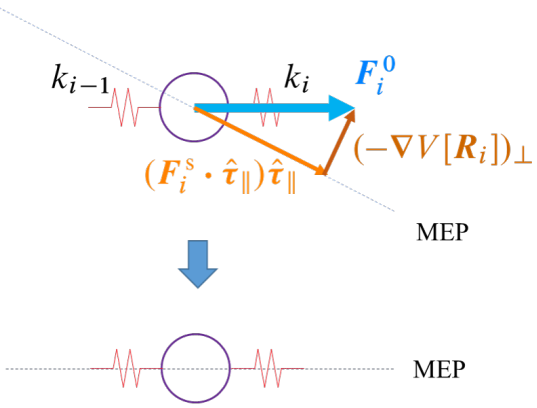

Figure 4.2: Schematic illustration of the goals of the nudged elastic band procedure in order to position replicas along a minimum energy path.

Additional modifications which have been made to the formulation of the nudged elastic band since its initial version include the adjustment of the tangent estimate initially to

$$\boldsymbol{\tau}_i = \begin{cases} \boldsymbol{\tau}_i^+, & V_{i+1} > V_i > V_{i-1} \\ \boldsymbol{\tau}_i^-, & V_{i+1} < V_i < V_{i-1} \end{cases},$$

[1] The original formulation of the spring force was that $(\boldsymbol{F}_i^{\mathrm{s}})_{\parallel} = k((\boldsymbol{R}_{i+1} - \boldsymbol{R}_i) - (\boldsymbol{R}_i - \boldsymbol{R}_{i-1})) \cdot \hat{\boldsymbol{\tau}}_i \hat{\boldsymbol{\tau}}_i$, but this was susceptible to leaving replicas unevenly distributed in regions of high curvature.

with $\boldsymbol{\tau}_i^+ = \boldsymbol{R}_{i+1} - \boldsymbol{R}_i$ and $\boldsymbol{\tau}_i^- = \boldsymbol{R}_i - \boldsymbol{R}_{i-1}$; in the case that the i^{th} replica is at an extremum, then a weighted average is taken, and

$$\boldsymbol{\tau}_i = \begin{cases} \boldsymbol{\tau}_i^+ \, \Delta V_i^{\max} + \boldsymbol{\tau}_i^- \, \Delta V_i^{\min}, & V_{i+1} > V_{i-1} \\ \boldsymbol{\tau}_i^+ \, \Delta V_i^{\min} + \boldsymbol{\tau}_i^- \, \Delta V_i^{\max}, & V_{i+1} < V_{i-1}, \end{cases}$$

with $\Delta V_i^{\max} = \max[\{|V_{i+1} - V_i|, |V_{i-1} - V_i|\}]$ and $\Delta V_i^{\min} = \min[\{|V_{i+1} - V_i|, |V_{i-1} - V_i|\}]$. These changes allow for improved convergence given a sufficient number of replicas. An additional change which may be implemented is to change the force on the replica with the highest energy as

$$\begin{aligned} \boldsymbol{F}_i^{\max} &= -\nabla V[\boldsymbol{R}_i^{\max}] + 2(\nabla V[\boldsymbol{R}_i^{\max}])_{\parallel} \\ &= -\nabla V[\boldsymbol{R}_i^{\max}] + 2\nabla V[\boldsymbol{R}_i^{\max}] \cdot \hat{\boldsymbol{\tau}}_i^{\max} \hat{\boldsymbol{\tau}}_i^{\max}. \end{aligned}$$

This implementation also improves convergence.

Let us now look more at the application to twins. Since the whole goal of the nudged elastic band is to provide some kind of an insight to the energetics of the twin system before it has fully formed an interface, the basic measure of energy here is just the difference in the per-atom energy in the replica configuration with that of the per-atom perfect crystal cohesive energy,

$$\Delta \mathsf{E}^i = \frac{\mathsf{E}^i}{n_{\text{atoms}}} - \mathsf{E}_0^{\text{pc}}, \tag{4.11}$$

with i representing the different replicas. The replica of interest to us is the one of the highest barrier. From this, we define the energetic barrier[2]

$$\Delta \mathsf{E}_{\max} = \max_i \Delta \mathsf{E}^i \, . \tag{4.12}$$

Note that we will make use of this raw change in the energy, as opposed to a measure more like γ^{tw} because there is technically no twin interface in the intermediate steps; consequently, it makes no sense to divide by an interface area, as we did for γ^{tw}.

Visualizing this information is a little tricky, since simply plotting E^i over the different replicas will not reveal too much useful information. Instead, we opt to represent the information through an Arrhenius relation,

$$K = \nu_0 \mathrm{e}^{-\Delta \mathsf{E}_{\max}/k_B \mathsf{T}}, \tag{4.13}$$

[2]For purposes of compactness, we will refer to this maximum energetic barrier as $\Delta \mathsf{E}$ in the tables which display this information.

where K is some measure of the frequency of visualization, k_B is Boltzmann's constant, and T is representative of some temperature. The idea is that twins with a higher $-\Delta\mathsf{E}_{\max}$ will result in a steeper Arrhenius curve, which indicates a lower likeliness to visualize that particular twin mode. The only additional quantity that needs to be computed in Equation (4.13) is the *attempt frequency* ν_0. This attempt frequency can be computed as a product of eigenvalues of the acoustic tensor in the stable (twin) state S and an unstable meta-state U (the position of the highest energetic barrier) following a prescription from Weiner [131],

$$\nu_0 = \frac{1}{2\pi} \frac{\prod_{i=1}^{n} \omega_{i,S}}{\prod_{i'=2}^{N} \omega_{i,U}}. \tag{4.14}$$

Equation (4.13) can be cast in a log-log form,

$$\ln[f] = \ln[\nu_0] - \frac{\Delta\mathsf{E}_{\max}}{k_B} \frac{1}{\mathsf{T}}, \tag{4.15}$$

which is then much more useful for visualization.

4.6 Additional Concepts: Atomistics

Geometric Construction of Twin Computational Cells

It is worth briefly mentioning that constructing a cell within LAMMPS requires a particular construction in order to facilitate the construction of scripts for computing the energy. In order to match the standard Cartesian coordinate formulation for a simple LAMMPS script, we need to correctly rotate our twin systems in order to line up appropriately. Fortunately, we are able to exploit the rotation invariance of the energies of the system, and are thus able to set up a computational domain normal to the twin plane, as illustrated in Figure 4.3.

The general notion of this rotation is that, since the normal and shear are perpendicular, we can construct a complete basis by introducing a third, orthogonal direction, $\boldsymbol{t} = \hat{\boldsymbol{n}} \times \boldsymbol{s}$. We may then apply a simple rotation so we now lie in the basis spanned by the twin normal, twinning shear, and this third, perpendicular direction. The details of the exact rotation are elaborated in Section A.2. For all of our simulations, we choose the twin normal direction to be the x direction, the twinning shear to be the y direction, and the third direction to be z for purposes of construction in LAMMPS.

4.7 Implementation: LAMMPS

The main software that we use for implementation is LAMMPS [132], a widely-recognized platform for calculations at the atomistic length scale. The implementation

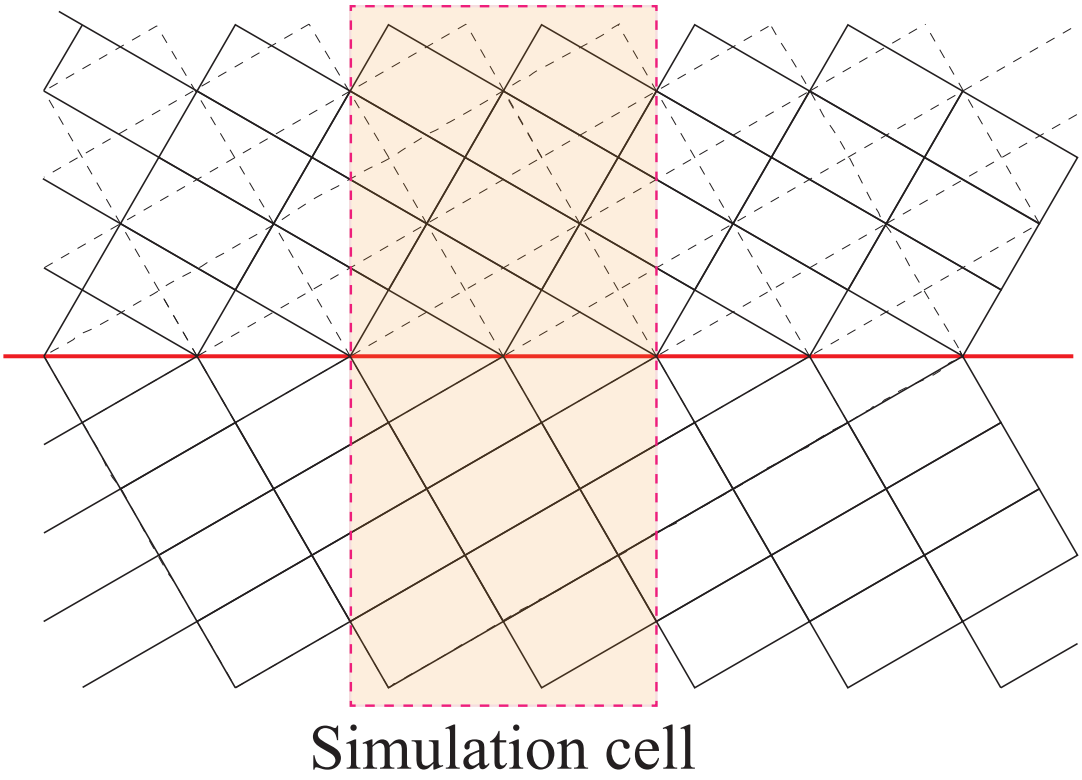

Figure 4.3: Schematic illustration of the computational cell used for energetics simulations with twins.

schemes we present in the remainder of this section will effectively outline the scripts that were used in order to perform calculations on the various twin modes relevant to this study.

Calibration of the Potential

The goal of this implementation is to find a stable energy minimum for a perfect crystal sample for any given interatomic potential. The end result of this is the identification of the lattice parameters a and c, along with the perfect crystal cohesive energy $\mathsf{E}_0^{\mathrm{pc}}$.

Twin Construction

We now present the implementation for constructing the twin geometry to account for both the rotation necessary to get the twin plane to line up with a box direction and be compatible with LAMMPS and also to account for potentially-irrational twin systems by rescaling the box to provide a sufficiently large sample.

Note that we have tested and verified that the rescaling presented in Algorithm 4.2 are such that the orientation of the plane produced here is no more than 0.003° from

Algorithm 4.1 Procedure for identifying the minimum-energy lattice parameters for studying a material of interest.

function CALIBRATE POTENTIAL($\boldsymbol{e}_i$) ▷ Identify stable parameters for interatomic potentials.
  for Each interatomic potential **do**
    Identify a reasonable test range of a and c.
    for Each test a and test c **do**
      Identify the units type (e.g. `metal`).
      Identify the dimensionality of the problem (e.g. for magnesium, `3`).
      Identify the periodicity of the problem (e.g. periodic directions).
      Identify the `atom_style` (e.g. for magnesium, `atomic`).
      Create the simulation box dimensions.
      Create a perfect crystal lattice of atoms.
      `replicate` the simulation box if necessary to increase the sample size.
      Point the script to the correct directory for the interatomic potential and its coefficients.
      Identify the neighborhood modification and thermodynamic variable calculation frequency.
      Define number of atoms, N, and energy of the system, E.
      Apply boundary conditions (e.g. anisotropic relaxation of atoms).
      Define minimization scheme, along with stop criteria.
      while $\mathsf{E} > \mathsf{E}_{\text{min}}$ **do**
        Compute energy of the crystal E_{test}.
      end while
      $\mathsf{E}^{\text{test}} \leftarrow \mathsf{E}_{\text{min}}$.
    end for
    $\mathsf{E}_0^{\text{pc}} \leftarrow \min_{a,c} \mathsf{E}_{\text{test}}[a, c, \boldsymbol{e}_i]$.
    Output: E_0^{pc} and a, c which yield that value.
  end for
end function

the true orientation of the plane for a sample size of approximately 2×10^6 atoms. This tolerance is deemed to be acceptably small for the purpose of rationalizing otherwise-irrational twin systems for computational purposes.

Twin Interface Energies

We now turn our attention towards the actual computation of the twin interface energies. Specifically, we seek to outline the procedure necessary to compute E^{tw}, the energy of the twinned configuration.

Once we have completed execution of Algorithm 4.3, we have E^{tw} for any predicted

Algorithm 4.2 Procedure for handling rational vs. irrational twin planes.

function DETERMINE TWIN RATIONALITY($\boldsymbol{e}_{[i]}, \boldsymbol{g}_{[i]}, \hat{\boldsymbol{n}}, \boldsymbol{s}, N^{\max}_{\text{atoms}}, l_x, l_y, l_z, \epsilon_R$)
  for Each twin solution **do**
    Identify a rotation matrix $\boldsymbol{Q}_B$ such that $\boldsymbol{Q}_B\hat{\boldsymbol{n}} = [1,0,0]$ ▷ This rotation changes the frame such that the twin plane normal always coincides with the x direction of the LAMMPS simulation box..
    Compute $\boldsymbol{e}'_{[i]} = \boldsymbol{Q}_B\boldsymbol{e}_{[i]}$ and $\boldsymbol{g}'_{[i]} = \boldsymbol{Q}_B\boldsymbol{g}_{[i]}$ ▷ $\boldsymbol{e}'_{[i]}$ and $\boldsymbol{g}'_{[i]}$ become the lattice vectors for the simulation.
    function APPROXIMATE RATIONALITY($\hat{\boldsymbol{n}}, \boldsymbol{s}$)
      Compute $\hat{\boldsymbol{n}}' = \text{round}[\hat{\boldsymbol{n}}]$ and $\boldsymbol{s}' = \text{round}[\boldsymbol{s}]$.
      if $(\hat{\boldsymbol{n}}' - \hat{\boldsymbol{n}} \leq \epsilon_R) \cap (\boldsymbol{s}' - \boldsymbol{s} \leq \epsilon_R)$ **then**
        System is approximately rational: $\epsilon_R \leftarrow 1$.
      else
        System is treated as irrational: $\epsilon_R \leftarrow 0$.
      end if
      Output: ϵ_R.
    end function
    if $\epsilon_R = 1$ **then**
      Use pre-defined box length inputs from LAMMPS script, l_x, l_y, l_z such that several periodic lengths in $\boldsymbol{s}$ along the plane are achieved.
    else if $\epsilon_R = 0$ **then**
      Find new multiplying factor ℓ on lateral periodicity such that $N_{\text{atoms}} \simeq N^{\max}_{\text{atoms}}$.
      $l_y \leftarrow \ell l_y$
      $l_z \leftarrow \ell l_z$
    end if
    Output: l_x, l_y, l_z.
  end for
end function

twin system. It is then just a matter of using E^{tw} and the atomic positions to deduce the remainder of the quantities necessary to compute γ^{tw} from Equation (4.7).

Barriers to Formation

In this section, we will outline the procedure for computing the barriers of formation for twins in LAMMPS. After executing Algorithm 4.4, we should have the information necessary to create Arrhenius plots for any of the twin modes of interest. Furthermore, we should also have information on the state of stress at any of the given replicas in the reaction path to producing any of the twin modes of interest, and we will use this information in Chapter 7 in order to construct the new yield surface for magnesium while accounting for the addition of these new twin modes.

Algorithm 4.3 Procedure for computing the twin interface energy.

function COMPUTE TWIN INTERFACE ENERGIES($\boldsymbol{e}_i, \boldsymbol{g}_i$) ▷ Use atomistic simulations to calculate the energies.
    Construct a simulation cell consistent with Figure 4.3.
    for all Interatomic potentials **do**
        for all Each twin predicted from the kinematic framework **do**
            Identify the units type (e.g. `metal`).
            Identify the dimensionality of the problem (e.g. for magnesium, `3`).
            Identify the periodicity of the problem (e.g. periodic directions).
            Identify the `atom_style` (e.g. for magnesium, `atomic`).
            Create the simulation box dimensions.
            Create the perfect crystal and twinned regions.
            Create regions where atoms will be fixed. Apply Algorithm 4.2 if necessary to adjust the simulation.
            Create atoms and `group` them for further assessment.
            Point the script to the correct directory for the interatomic potential and its coefficients.
            Identify the neighborhood modification and thermodynamic variable calculation frequency.
            Define number of atoms, N, and energy of the system, E.
            Apply boundary conditions (e.g. fixed atoms).
            Define minimization scheme, along with stop criteria.
            while $\mathsf{E} > \mathsf{E}^{\min}$ **do**
                Compute variables of interest (e.g. atomic locations, energy).
            end while
            $\mathsf{E}^{\mathrm{tw}} \leftarrow \min \mathsf{E}$.
        end for
    end for
    Store: E^{tw}, atomic positions.
end function

4.8 Background on Density Functional Theory

Usable as a tool for accurate calculation of the configuration, *density functional theory* is an approximation to quantum mechanics which allows for implementation of efficient, scalable codes in order to solve for a variety of physical problems which may be of interest. The idea is that the electronic structure of a system of interest can be determined through the use of functionals that depend on functions of the electron density. The earliest forerunners of density functional theory were formulated in 1927 by Thomas and Fermi [133, 134]; other formulations, such as the one by Hohenberg and Kohn [135], were cast over the years. A summary of these formulations can be found in Parr and Yang [136].

Algorithm 4.4 Procedure for computing the barriers to formation for the twins.

function COMPUTE FORMATION BARRIER($\boldsymbol{e}_i, \boldsymbol{g}_i$) ▷ Use atomistic simulations to calculate the formation barriers for each of the twins.
  for all Twin modes with $\gamma^{\text{tw}} < 325$ mJ/m^2 and $s \leq 4$ **do**
    Maintain all of the same construction procedures as Algorithm 4.3, but change the lattice parameters to reconstruct a perfect crystal and also adjust sorting if you wish for the perfect crystal atom IDs.
    Compute the atomic locations of the perfect crystal, storing them for instruction into the NEB calculation.
    Set the end replicas as the perfect crystal and twinned state.
    Distribute replicas between the perfect crystal and twinned state (e.g. in this case, 64 replicas). Displace atoms a small amount if necessary.
    Define convergence criteria for NEB replicas (energy and force tolerances, along with maximum number of iterations).
    for all Replicas **do**
      Define minimization scheme and conditions.
      Calculate E_i, the energy of the i^{th} replica.
    end for
    Calculate the energetic barrier to formation $\Delta\mathsf{E}^{\max} = \max_i[\mathsf{E}_i - \mathsf{E}_0^{\text{pc}}]$.
    Calculate the attempt frequency ν_0 using Equation (4.14).
    Compute the Arrhenius barrier K using Equation (4.13).
    Export the virial stresses at the maximum barrier $\boldsymbol{\sigma}^{\max}$.
  end for
  Store: $\Delta\mathsf{E}^{\max}$, $\boldsymbol{\sigma}^{\max}$, atomic positions.
end function

Although there have been many variants of density functional theory developed over the years, the one that we choose to focus on is the formulation by Kohn and Sham [137]. The main feature of interest in this case is the introduction of an energy functional

$$\begin{aligned}\mathsf{E}[\psi, \boldsymbol{R}] = \mathsf{T}_s[\rho_\alpha, \rho_\beta] + \mathsf{E}_H[\rho_\alpha, \rho_\beta] + \mathsf{E}_{\text{ext}}[\rho_\alpha + \rho_\beta, \boldsymbol{R}] \\ + \mathsf{E}_{zz}[\boldsymbol{R}] + \mathsf{E}_{xc}[\rho_\alpha, \rho_\beta],\end{aligned} \tag{4.16}$$

with ψ being the quantum mechanical wavefunctions, $\boldsymbol{R}$ being the positions of the atomic nuclei, and ρ_α and ρ_β denoting the spin-up and spin-down electron densities, respectively. Note that the terms in Equation (4.16) can be further expanded. T_s represents the kinetic energy of non-interacting electrons,

$$\mathsf{T}_s[\rho_\alpha, \rho_\beta] = -\frac{1}{2}\sum_\sigma \sum_{i=1}^{N_\sigma} \int_{\mathbb{R}^3} \psi_{i\sigma}^*[\boldsymbol{x}]\nabla^2\psi_{i\sigma}[\boldsymbol{x}]\,\mathrm{d}\boldsymbol{x}. \tag{4.17}$$

E_H represents the Hartree energy,

$$\mathsf{E}_H[\rho] = \frac{1}{2}\iint_{\mathbb{R}^3} \frac{\rho[\boldsymbol{x}]\rho[\boldsymbol{x}']}{\|\boldsymbol{x}-\boldsymbol{x}'\|}\,\mathrm{d}\boldsymbol{x}\,\mathrm{d}\boldsymbol{x}', \tag{4.18}$$

which is the classical electrostatic interaction energy of the electron density. E_{ext} represents the energy that arises from interaction with an external potential,

$$\mathsf{E}_{\text{ext}}[\rho, \boldsymbol{R}] = \int_{\mathbb{R}^3} \rho[\boldsymbol{X}]\mathsf{V}_{\text{ext}}[\boldsymbol{x}, \boldsymbol{R}]\,\mathrm{d}\boldsymbol{x}. \tag{4.19}$$

E_{zz} represents the repulsive energy between the nuclei,

$$\mathsf{E}_{zz}[\boldsymbol{R}] = \frac{1}{2}\sum_{i=1}^{M}\sum_{\substack{j=1\\ j\neq i}}^{M} \frac{Z_i Z_j}{\|\boldsymbol{R}_i - \boldsymbol{R}_j\|} = \frac{1}{2}\iint_{\mathbb{R}^3} \frac{b[\boldsymbol{x}, \boldsymbol{R}]b[\boldsymbol{x}', \boldsymbol{R}]}{\|\boldsymbol{x}-\boldsymbol{x}'\|}\,\mathrm{d}\boldsymbol{x}\,\mathrm{d}\boldsymbol{x}'. \tag{4.20}$$

Finally, E_{xc}, the exchange correlation energy, represents a point of controversy, since all of the "unknown" terms in the energy are effectively cast in this term. The exchange correlation energy can be decomposed additively into an exchange energy, E_x, and a correlation energy, E_c, through the relation

$$\mathsf{E}_{xc} = \mathsf{E}_x[\rho_\alpha, \rho_\beta] + \mathsf{E}_c[\rho_\alpha, \rho_\beta]. \tag{4.21}$$

A common approach to these terms is to assume a local spin density approximation, with uniform electron gas of same local density. This allows for the expression of the exchange energy and the correlation energy as

$$\mathsf{E}_x[\rho_\alpha, \rho_\beta] = -\frac{3}{4}\left(\frac{6}{\pi}\right)^{1/3}\int_{\mathbb{R}^3}\left[\rho_\alpha[\boldsymbol{x}]^{4/3} + \rho_\beta[\boldsymbol{x}]^{4/3}\right]\mathrm{d}\boldsymbol{x} \tag{4.22a}$$

$$\mathsf{E}_c = \int_{\mathbb{R}^3} \mathcal{E}_c[\rho_\alpha[\boldsymbol{x}], \rho_\beta[\boldsymbol{x}]]\,\mathrm{d}\boldsymbol{x}. \tag{4.22b}$$

Objectively, one would like to take the energy of Equation (4.16) and subject it to some form of minimization. In this case, the energy would be taken by finding

$$\mathsf{E}_0[\boldsymbol{R}] = \inf_{\psi} \mathsf{E}[\psi, \boldsymbol{R}], \tag{4.23}$$

subject to the constraint of

$$\int_{\mathbb{R}^3} \psi^*_{i\sigma}[\boldsymbol{x}]\psi_{j\sigma}[\boldsymbol{x}]\,\mathrm{d}\boldsymbol{x} = \delta_{ij}, \tag{4.24}$$

which holds for $\sigma \in \{\alpha, \beta\}$ denoting the spin of the electrons, and $\{i, j\} = \{1, 2, \ldots, N_\sigma\}$. Such minimization can be accomplished by recasting our equations to an eigenvalue problem,

$$\left(-\frac{1}{2}\nabla^2 + \mathsf{V}_{\text{eff}}[\boldsymbol{x}, \boldsymbol{R}]\right)\psi_i[\boldsymbol{x}] = \mathcal{H}\psi_i[\boldsymbol{x}] = \sum_{j=1}^{N}\lambda_{ij}\psi_j[\boldsymbol{x}]. \tag{4.25}$$

The trouble with solving these kinds of eigenvalue problems is that they typically scale as $\mathcal{O}[N^3]$, with N being the number of electrons in the system. This severely limits the size of the computational systems that may be examined and, consequently, the scope of real-world materials problems that can be examined with these techniques. For instance, material defects occur on the order of several parts per million, meaning that a system of millions of atoms would be necessary in order to accurately model the system, something that simply would not be possible with standard, $\mathcal{O}[N^3]$ methods.

Fortunately, advancements in density functional theory method development have allowed us to surmount this limitation. A method known as the linearly-scaling spectral Gauss quadrature (LSSGQ) method was introduced by Suryanarayana *et al.* [138], which not only brought down the scaling to a very tractable $\mathcal{O}[N]$, but also laid the groundwork for further implementation (completed by Ponga *et al.* [139]). In particular, the use of the spectral integral

$$(f[H]\zeta, \zeta) = \int_{\sigma[H]} f[\lambda] \, \mathrm{d}\xi_{\zeta,\zeta}[\lambda] \tag{4.26}$$

allowed the casting of various terms as functions which would become integrals over their eigenvalue spectra. In turn, this paved the way for several key quantities of interest in DFT calculations, such as the electron density,

$$\rho[\boldsymbol{x}_0] = 2 \sum_{n=1}^{N_d} g[\lambda_n, \lambda_f] |\psi_n[\boldsymbol{x}]|^2, \tag{4.27}$$

and the band energy,

$$\mathsf{U}_{\text{band}} = 2 \sum_{n=1}^{N_d} \lambda_n g[\lambda_n, \lambda], \tag{4.28}$$

to be written as integrals over the eigenvalue spectrum, which were then written numerically in terms of spectral Gauss quadrature:

$$\rho[\boldsymbol{x}_0] = 2 \int_a^b g[\lambda, \lambda_f] \, \mathrm{d}\xi_{\zeta,\zeta}[\lambda] \approx 2 \sum_{k=1}^{K} w_k^{\zeta} g[\lambda_k^{\zeta}, \lambda_f] \tag{4.29a}$$

$$\mathsf{U}_{\text{band}} = 2 \sum_{p=1}^{N_d} \int_a^b \lambda g[\lambda, \lambda_f] \, \mathrm{d}\xi_{\eta_p,\eta_p}[\lambda] \approx 2 \sum_{k=1}^{N_d} \sum_{k=1}^{K} w_k^{\eta_p} \lambda_k^{\eta_p} g[\lambda_k^{\eta_p}, \lambda_f], \tag{4.29b}$$

with λ_f being the Fermi level, w representing Gauss node weights, and g representing an occupation function, which would typically be taken to be some approximation to the Fermi-Dirac distribution, usually chosen to be some kind of polynomials. Note that the efficient approximation of the spectrum is still an area of active research. Additional concepts not covered in [138] can be found in Wang *et al.* [140].

4.9 Additional Concepts: MacroDFT Formulation

Electrostatic Energy

The calculation of the electrostatics relies on the fact that the energy term

$$\mathsf{E}_H[\rho] + \mathsf{E}_{\text{ext}}[\rho, \boldsymbol{R}] = -\frac{1}{8\pi}\int_{\mathbb{R}^3} \|\nabla\phi[\boldsymbol{x}, \boldsymbol{R}]\|^2 \,\mathrm{d}\boldsymbol{x} + \int_{\mathbb{R}^3} (\rho[\boldsymbol{x}] + b[\boldsymbol{x}, \boldsymbol{R}])\phi[V\boldsymbol{x}, \boldsymbol{R}]\,\mathrm{d}\boldsymbol{x} \tag{4.30}$$

results in the Poisson's equation

$$-\frac{1}{4\pi}\nabla^2\phi[\boldsymbol{x}, \boldsymbol{R}] = \rho[\boldsymbol{x}] + b[\boldsymbol{x}, \boldsymbol{R}], \tag{4.31}$$

with ϕ being the electrostatic potential. A calculation of this is shown in Appendix A.5.

Atomic Positions and Forces

In order to fully achieve the ground state configuration, the energy functional must also be minimized with respect to the positions of the nuclei, $\boldsymbol{R}$. Consider the forces on the j^{th} nuclei, f_j. This can be found by varying $\mathcal{E}_0[\boldsymbol{R}]$ with respect to $\boldsymbol{R}$, giving us that

$$f_j = -\int_{\mathbb{R}^3} \frac{\partial b_j[\boldsymbol{x}, \boldsymbol{R}_j]}{\partial \boldsymbol{R}_j}\,\mathrm{d}\boldsymbol{x}\,, \tag{4.32}$$

with

$$\phi_j[\boldsymbol{x}, \boldsymbol{R}_j] = \int_{\mathbb{R}^3} \frac{b_j[\boldsymbol{x}', \boldsymbol{R}_j]}{\|\boldsymbol{x} - \boldsymbol{x}'\|}\,\mathrm{d}\boldsymbol{x}'\,.$$

In the special case of $b_j[\boldsymbol{x}, \boldsymbol{R}_j] = Z_j\delta[\boldsymbol{x} - \boldsymbol{R}_j]$, i.e. that we have a distribution of point charges, then Equation (4.32) reduces to

$$f_j = Z_j\nabla\big[\phi[\boldsymbol{x}, \boldsymbol{R}] - \phi_j[\boldsymbol{x}, \boldsymbol{R}_j]\big]. \tag{4.33}$$

This is implemented in MacroDFT (Section 4.10).

Finite Temperature Approximation

By definition, the ground state energy is taken at zero temperature. To extend this as an approximation to finite temperature, we make use of the term

$$\begin{aligned}\mathcal{E}_\sigma = 2\sum_n g[\lambda_n, \lambda_f]\lambda_n + \mathsf{E}_{xc}[\rho] + \frac{1}{2}\int_{\mathbb{R}^3} (b[\boldsymbol{x}, \boldsymbol{R}] - \rho[\boldsymbol{r}])\phi[\boldsymbol{x}, \boldsymbol{R}]\,\mathrm{d}\boldsymbol{x} \\ - \int_{\mathbb{R}^3} \mathsf{V}_{xc}[\rho]\rho[\boldsymbol{x}]\,\mathrm{d}\boldsymbol{x} - \frac{1}{2}\sum_{j=1}^{m}\iint_{\mathbb{R}^3} \frac{b_j[\boldsymbol{x}, \boldsymbol{R}_j]b_j[\boldsymbol{x}', \boldsymbol{R}_j]}{\|\boldsymbol{x} - \boldsymbol{x}'\|}\,\mathrm{d}\boldsymbol{x}\,\mathrm{d}\boldsymbol{x}'\,,\end{aligned} \tag{4.34}$$

which then results in the entropy being

$$\begin{aligned} \mathsf{S} = 2k_B \sum_n \big[& g[\lambda_n, \lambda_f] \log[g[\lambda_n, \lambda_f]] \\ & + (1 - g[\lambda_n, \lambda_f]) \log[1 - g[\lambda_n, \lambda_f]] \big] . \end{aligned} \tag{4.35}$$

With these terms computed, we can then find the Helmholtz free energy and, consequently, the approximation of the ground state results. Further details of the finite temperature approximation can be found in Gillian [141].

Spectral Theory

Let there exist a self-adjoint operator $\mathscr{H}$ on a finite-dimensional Hilbert space $\mathcal{H}$, with inner product $(\cdot, \cdot)$ and norm $\| \cdot \|$ defined. Then, there exists a unique resolution of the identity ξ that satisfies

$$\mathscr{H} = \int_{\sigma[\mathscr{H}]} \lambda \, \mathrm{d}\xi[\lambda] , \tag{4.36}$$

with $\sigma[\mathscr{H}]$ defined as the spectrum of $\mathscr{H}$. As a result, any function f on $\sigma[\mathscr{H}]$ can be expanded using a Riemann-Stieltjes integral as

$$f[\mathscr{H}] = \int_{\sigma[\mathscr{H}]} \lambda f[\lambda] \, \mathrm{d}\xi[\lambda] . \tag{4.37}$$

Now suppose that we have some kind of an orthonormal basis $\mathcal{H}$, which we call $\{\eta_p\}_{p=1}^{N_d}$ so that, for any $\zeta \in \mathcal{H}$, we can write out

$$\zeta = \sum_{p=1}^{N_d} \zeta_p \eta_p .$$

In such a basis, we would be able to expand out the eigenfunctions on this basis according to

$$\psi_n = \sum_{p=1}^{N_d} \psi_{n,p} \eta_p .$$

Hereafter, we have a representation of some measure $\xi_{\zeta,\xi}[\lambda]$ on $\mathscr{H}$; this can be written as

$$\begin{aligned} \xi_{\zeta,\xi}[\lambda] &= (\xi[\lambda]\zeta, \zeta) \\ &= \begin{cases} 0, & \lambda < \lambda_1 \\ \displaystyle\sum_{n=1}^{m} \sum_{p=1}^{N_d} \sum_{q=1}^{N_d} \psi_{n,p} \psi_{n,q} \zeta_p \zeta_q , & \lambda_m \leq \lambda < \lambda_{m+1} \\ \displaystyle\sum_{n=1}^{N_d} \sum_{p=1}^{N_d} \sum_{q=1}^{N_d} \psi_{n,p} \psi_{n,q} \zeta_p \zeta_q , & \lambda_{N_d} < \lambda \end{cases} . \end{aligned} \tag{4.38}$$

In the special case of $\zeta = \eta_k$ (which is directly applicable to our case), Equation (4.38) reduces to

$$\xi_{\eta_k,\eta_k}[\lambda] = \begin{cases} 0, & \lambda < \lambda_1 \\ \sum_{n=1}^{m} |\psi_{n,k}|^2, & \lambda_m \leq \lambda < \lambda_{m+1} \\ \sum_{n=1}^{N_d} |\psi_{n,k}|^2, & \lambda_{N_d} < \lambda \end{cases}. \tag{4.39}$$

Consequently, for any $\zeta \in \mathcal{H}$, we may then write

$$(f[\mathscr{H}]\zeta, \zeta) = \int_{\sigma[\mathscr{H}]} f[\lambda]\, \mathrm{d}\xi_{\zeta,\zeta}[\lambda] = \int_a^b f[\lambda]\, \mathrm{d}\xi_{\zeta,\zeta}[\lambda]\,, \tag{4.40}$$

with $a = \lambda_1$ and $b = \lambda_{N_d}$. Numerically, an integral like the form of Equation (4.40) can be evaluated using Gauss quadrature; the function can thus be expanded as

$$f[\lambda] \approx \sum_{k=1}^{K} f[\lambda_k^\xi] l_k^\xi[\lambda], \tag{4.41}$$

with $\{\lambda_k^\xi\}_{k=1}^K$ being the quadrature points, and $l_k^\xi[\lambda]$ being the Lagrange polynomial

$$l_k^\xi[\lambda] = \prod_{\substack{j=1 \\ j\neq k}} \frac{\lambda - \lambda_j^\xi}{\lambda_k^\xi - \lambda_j^\xi}.$$

Additional details for this can be found in Golub and Meurant [142].

The Modified Lanczos Algorithm

The idea here is that we have an eigenvalue problem of the form

$$\boldsymbol{H}\psi_n = \lambda_n \psi_n,$$

which is the fundamental eigenvalue problem that we are trying to solve in quantum mechanical problems. The modified Lanczos algorithm that is implemented within MacroDFT itself is prescribed in Algorithm 4.5. The result of this procedure is the set of eigenvalues of the Hamiltonian operator, which is an integral portion of the self-consistent loop.

4.10 Implementation: MacroDFT

With the theory summarized here, Ponga *et al.* [139] implemented this as a real-space density functional theory code known as MacroDFT. With spatial coarse graining,

Algorithm 4.5 Modified Lanczos algorithm which is used within MacroDFT.

1: **function** MODIFIED LANCZOS ALGORITHM
2: Initialize with $b_0 = 1$ and

$$\boldsymbol{v}_0 = \begin{bmatrix} 0 \\ \vdots \\ 0 \\ \vdots \\ 0 \end{bmatrix} \qquad \boldsymbol{v}_1 = \begin{bmatrix} 0 \\ \vdots \\ 1 \\ \vdots \\ 0 \end{bmatrix}.$$

3: Use the iterative relation that

$$b_{k+1}\boldsymbol{v}_{k+1} = (\boldsymbol{H} - B\boldsymbol{a}_{k+1})\boldsymbol{v}_{k+1} - b_k\boldsymbol{v}_{k-1}.$$

4: Update $\boldsymbol{a}_{k+1} \leftarrow \boldsymbol{v}_k \boldsymbol{H} \boldsymbol{v}_k$.
5: **end function**

MacroDFT has been shown to be a viable method for solving problems of up to the order of billions of atoms. The general procedure for MacroDFT is shown in Algorithm 4.6.

4.11 Summary

We began this chapter wanting a way to examine the energetic landscape of twinning. Over the course of this chapter, we have now covered two techniques which will help us identify the energy of the twin interface; the first of these is the relatively inexpensive molecular statics, and the other is the expensive-but-accurate density functional theory. The identification of the twin interface energy will begin to allow us to understand why certain twin modes are favored over others, and if there are any additional modes with competitive energies relatively to previously-visualized twin modes. Our routine of studying the energetics of the twins will also provide us insight on the energetic barriers to formation, which will give us yet another avenue by which we can measure the likeliness to visualize any particular twin mode. In the next chapter, we will utilize these techniques and begin to study the twin modes that we had predicted as being kinematically possible in Chapter 3.

Algorithm 4.6 Procedure for identifying the minimum-energy lattice parameters for studying a material of interest.

function COMPUTE TWIN INTERFACE ENERGY($\boldsymbol{e}_i$, $\boldsymbol{g}_i$) ▷ Use MacroDFT to compute the twin interface energy.
  for Each twin mode **do**
    Input the coarse-grained atomic and electronic meshes.
    while $\mathsf{E} > \mathsf{E}_{\text{min}}$ **do**
      Compute the nuclear charge density $b[\boldsymbol{x}, \boldsymbol{R}]$.
      Provide the guess of the electron density $\rho[\boldsymbol{x}]$.
      while $|\rho_2 - \rho_1| >$ tol. **do**
        Solve the eigenvalue problem $\mathcal{H}\psi_n = \lambda_n \psi_n$
        Find λ_f subject to constraint $N_e = 2\sum_n g[\lambda_n, \lambda_f]$.
        Update the density, $\rho_2 = \sum_n g[\lambda_n, \lambda_f]|\psi_n|^2$.
        Solve Poisson's equation, $\nabla^2\phi = -4\pi(\rho + b)$.
        Update the density through a mixing algorithm.
      end while
      Compute the forces on the atomic nuclei.
    end while
    Compute the Helmholtz free energy.
    Take a ground-state approximation of the energy.
    Output: Atom and electron distributions, E^{tw}.
  end for
end function

Chapter 5

RESULTS: TWIN ENERGETICS

5.1 Goals of this Chapter

Now that we have completed discussing the steps of formulation necessary to study all of the energetics of the various twin systems, we will actually put the concepts into practice and show the results that were achieved for magnesium. Towards the end of the chapter, we will also highlight the flexibility of our development by also applying some components of our energetics studies to additional materials.

5.2 Perfect Crystal Calibration

Reasonable implementation of the potentials is a vital first step, and the goal of this is to extract the c/a which will be used in the kinematic framework, in addition to the lattice parameter a and the perfect crystal cohesive energy E_0^{pc}, which will be a centerpiece for the energetics calculations. For magnesium, a range of test values for a and c were chosen and the relaxation of 32-atom perfect crystal samples were studied using LAMMPS to find the values of a, c and E_0^{pc}. The values for the three potentials which would be tested for magnesium [125, 143, 144] are presented in Table 5.1. Further validation in the form of elastic constants are computed from these optimal parameters; the results are presented in Table 5.2.

	EAM [125]	MEAM [143]	Mod. MEAM[144]
a [Å]	3.184	3.208	3.196
c/a	1.628	1.620	1.623
E_0^{pc} [eV/atom]	-1.529	-1.548	-1.508

Table 5.1: Relaxed lattice parameters and cohesive energy obtained from potential training.

Varying sample sizes for potential training up to 512 atoms were tested, with all relaxed parameters showing agreement to six decimal points. As such, the results for samples of other sizes will not require further reporting in this work.

Training of the potentials is necessary not only for obtaining the optimal lattice parameters to ensure a stable solution for a given potential, but also for obtaining the c/a ratio that affects the results predicted in the kinematic framework. Table 5.1

Constant	Experiment	EAM [125]	MEAM [143]	Mod. MEAM [144]
C_{11}	63.5	67.4	67.2	67.7
C_{22}	25.9	26.1	25.6	24.7
C_{13}	21.7	13.8	19.8	18.7
C_{33}	66.5	69.4	68.5	68.9
C_{44}	18.4	10.8	17.2	17.9

Table 5.2: Elastic constants calculated from the optimal parameters of Table 5.1.

confirms that the implementation of the potentials here — particularly the MEAM and Modified MEAM — are acceptably-close to the implementations in their respective works. The particular $c^\star/a^\star$ found in the Modified MEAM is then passed into the kinematic framework. Note that this is an important, since Figure 3.11 shows that there is, to some extent, dependence of the possible twin modes on the c/a ratio being inputted — a finding which is consistent with that of classical literature.

5.3 Twin Interface Energy: Magnesium

We perform the calculations for γ^{tw} following Algorithm 4.3. We then plot γ^{tw} against the magnitude of the twinning shear, $s = \|\boldsymbol{s}\|$, and obtain the scatterplot represented in Figure 5.1. The cutoff regions are chosen to be $s \leq 8$, by choice from setting the parameters of μ_i^j, and also $\gamma^{\text{tw}} \leq 500$ mJ/m^2, since this region focuses our studies to modes which are competitive relative to modes that have been previously observed.

An immediate observation from Figure 5.1 is that the energy landscape for magnesium is extremely diverse, thus continuing our narrative from Chapter 3 that the picture of twinning in magnesium is considerably more complicated than what has been previously acknowledged. The five highlighted points on the scatterplot of Figure 5.1 represent the modes that had been previously visualized and discussed in Table 1.1 and Figure 1.8. Consequently, our notions that there are additional, competitive twin modes (relative to the ones that have been observed in prior literature) are strengthened.

One additional observation that we are able to gather from this investigation is the fact that the vast majority of twins with low interface energies and low shear magnitudes are two-fold rotations. Since two-fold rotations are outlined in teal in Figure 5.1, we can see that most of these are concentrated more towards the lower-left, with twin modes with high shear and high interface energy typically being rotations other than two-fold. This is a rather interesting result, as it would seem to lie in agreement with classical notions that twins arise from two-fold rotations.

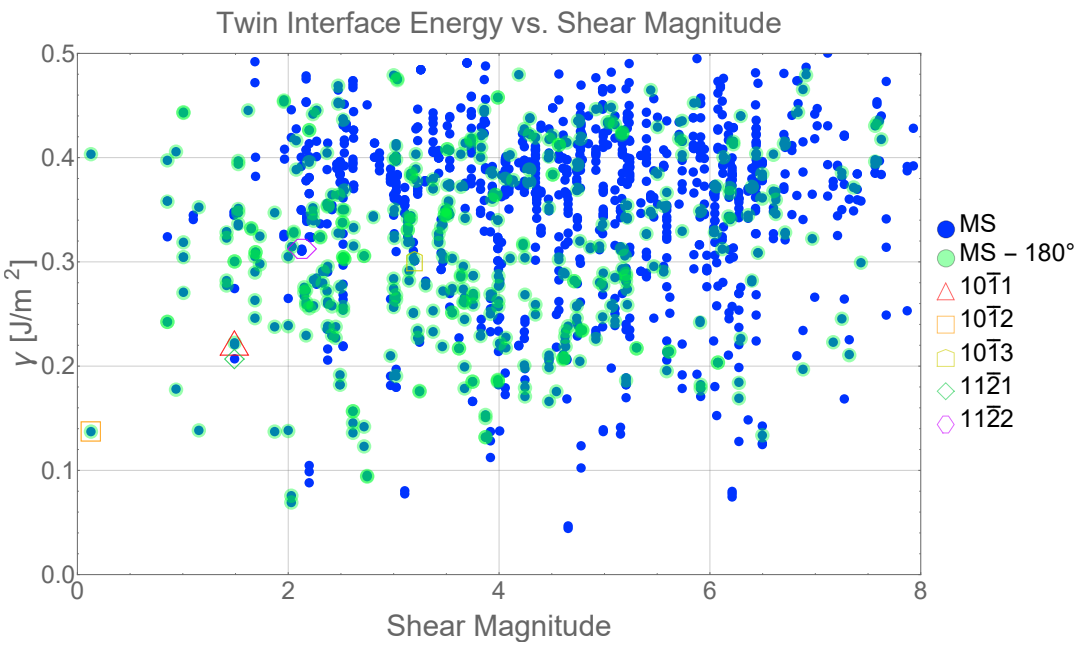

Figure 5.1: Scatterplot of the twin energies for magnesium, as detected using the modified MEAM potential [144]. Cutoffs chosen are $\gamma \leq 500$ mJ/m^2 and $s \leq 8$ to capture the energies of previously-observed twin modes.

To put some numerical values into perspective, we tabulate all of the information computed up to this point for twelve example twin modes in Table 5.3. This table include information on the twin system, along with the shear magnitude, the rotation from Equation (2.18), and also the computed interface energy γ^{tw}. Note that modes a and b are representative of the classical tension and compression twins, respectively. Additionally, note that the rationalized representations of the irrational indices were chosen by the usual process of finding common ratios and then rounding to the nearest full integer.

The twelve twin modes from Table 5.3 also show that many of the low-energy, low-shear modes are mostly two-fold rotations. By the way we selected these twin modes, all of the interface energies are competitive relative to the classically-observed modes. We also still see that there are several irrational twin modes which are represented in this table, also reflective of what we saw with Figure 5.1.

Let's look at some of the irrational twin modes. The atomic configuration of one of these modes is represented in Figure 5.2. In particular, we note that, although the twin plane technically does not pass through more than one set of atoms, the interface itself appears to form facets upon relaxation! This seems to agree with classical postulations that irrational twins would likely form steps [145–150].

i	Twin $\{K_1\}\langle\eta_1\rangle$	s	θ	γ^{tw} [mJ/m^2]
a	$\{10\bar{1}2\}\langle10\bar{1}1\rangle$	0.1299	180	137.0
b	$\{10\bar{1}1\}\langle10\bar{1}2\rangle$	1.4919	180	222.0
c	$\{21\bar{3}0\}\langle10\bar{1}0\rangle$	1.7321	180	297.4
d	$\{11\bar{2}0\}\langle0001\rangle$	1.8743	180	242.2
e	$\{21\bar{3}2\}\langle10\bar{1}0\rangle$	2.0343	180	68.8
f	$\{10\bar{1}3\}_{\text{I}}\langle50\bar{5}4\rangle_{\text{I}}$	2.1568	180	275.4
g	$\{21\bar{3}0\}\langle10\bar{1}1\rangle$	2.3738	180	271.8
h	$\{15, 8, \overline{23}, 1\}_{\text{I}}\langle10\bar{1}1\rangle$	2.3773	159.3	290.1
i	$\{31, 1, \overline{32}, \overline{29}\}_{\text{I}}\langle10\bar{1}1\rangle$	3.0245	159.3	309.6
j	$\{11\bar{2}1\}_{\text{I}}\langle10\bar{1}1\rangle$	3.1921	159.3	250.6
k	$\{30\bar{3}4\}_{\text{I}}\langle10\bar{1}3\rangle_{\text{I}}$	3.4703	180	271.4
l	$\{10\bar{1}2\}_{\text{I}}\langle40\bar{4}5\rangle_{\text{I}}$	3.7584	180	266.2

Table 5.3: Details on twelve example twin systems with $\gamma^{\text{tw}} \leq 325$ mJ/m^2 and $s \leq 4$.

5.4 Twin Interface Energy for Magnesium in MacroDFT

Subsequently, we also perform an investigation of the twin interface energy using density functional theory calculations in order to obtain additional assurance of the reputedly low energies of these twin interfaces. Due to the highly expensive nature of these calculations, we were only able to study a small number of twin systems.

The lattice vectors from the kinematic framework are inputted into MacroDFT and γ^{tw} is computed, allowing again for relaxation of atoms subject to fixture at the twin interface, which is consistent with the boundary conditions in the molecular statics simulations. Example calculations of γ^{tw} are obtained and presented in Table 5.4, where they are also compared against literature results where available.

Twin Normal	$(10\bar{1}1)$	$(10\bar{1}2)$	$(11\bar{2}1)$	Irrational 1
Literature γ^{tw}	70.0[51]-85.5[49]	114.0[46, 51]-122.3[49]	-	-
MacroDFT γ^{tw}	80.5	102.0	189.2	52.3

Table 5.4: Tabulation of γ^{tw} for several example low-energy twin modes, with results from MacroDFT compared to values previously found in literature.

Based on this tangential investigation, the Modified MEAM potential was chosen for further study in creating Figure 5.1 and also for the subsequent nudged elastic band calculation, as it was one of the latest potentials that was developed at the time this work was written and was very accurately calibrated to capture the behavior of twins accurately. Further confidence was instilled by the fact that an interface energy value for the tension twin of $\gamma^{\text{tw}} = 137.0$ mJ/m^2 using the Modified MEAM

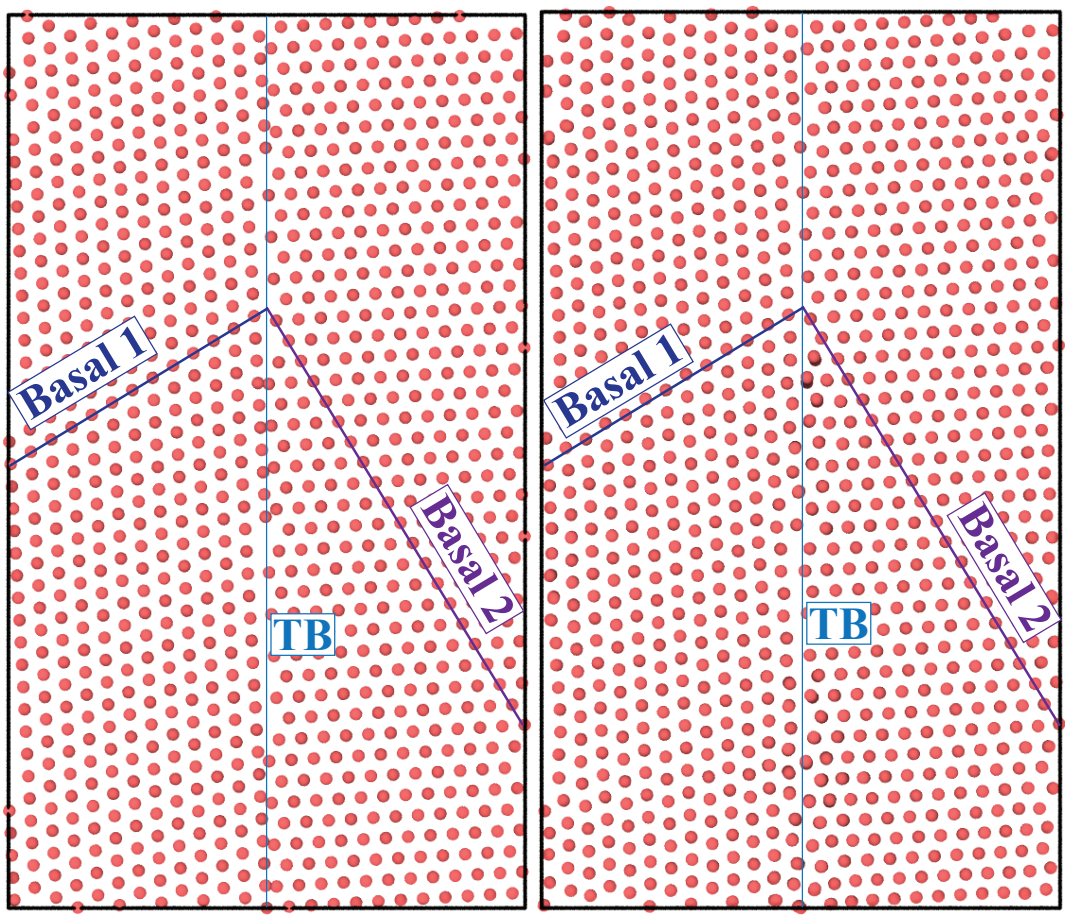

Figure 5.2: Atomic configuration of a predicted irrational twin, with basal direction labeling, visualized within OVITO [151]. Note that only a part of the entire simulation box is visualized.

potential, which was reasonably close to a value of $\gamma^{\text{tw}} = 102.0$ mJ/m^2 obtained using MacroDFT.

5.5 Twin Interface Energy: Additional Materials

Cubic Materials

A rudimentary study of the twin interface energy for cubic materials is also performed. We study BCC iron using a potential developed by Mendelev *et al.* [152], FCC silver using a potential developed by Williams, Mishin, and Hamilton [153], FCC copper using a potential developed by Mendelev *et al.* [154], and BCC tantalum using a potential developed by Ravelo *et al.* [155].

Unlike what is observed for HCP materials, the plot of twin interface energy against shear magnitude is much sparser for cubic materials, even though the kinematic framework still suggests a significant number of possible twin modes in both BCC

and FCC materials. Two examples of these plots are shown in Figures 5.3 and 5.4. A cutoff window of $\gamma^{\text{tw}} \leq 1000$ mJ/m^2 is chosen in order to keep the plot window relatively similar to what is shown for magnesium.

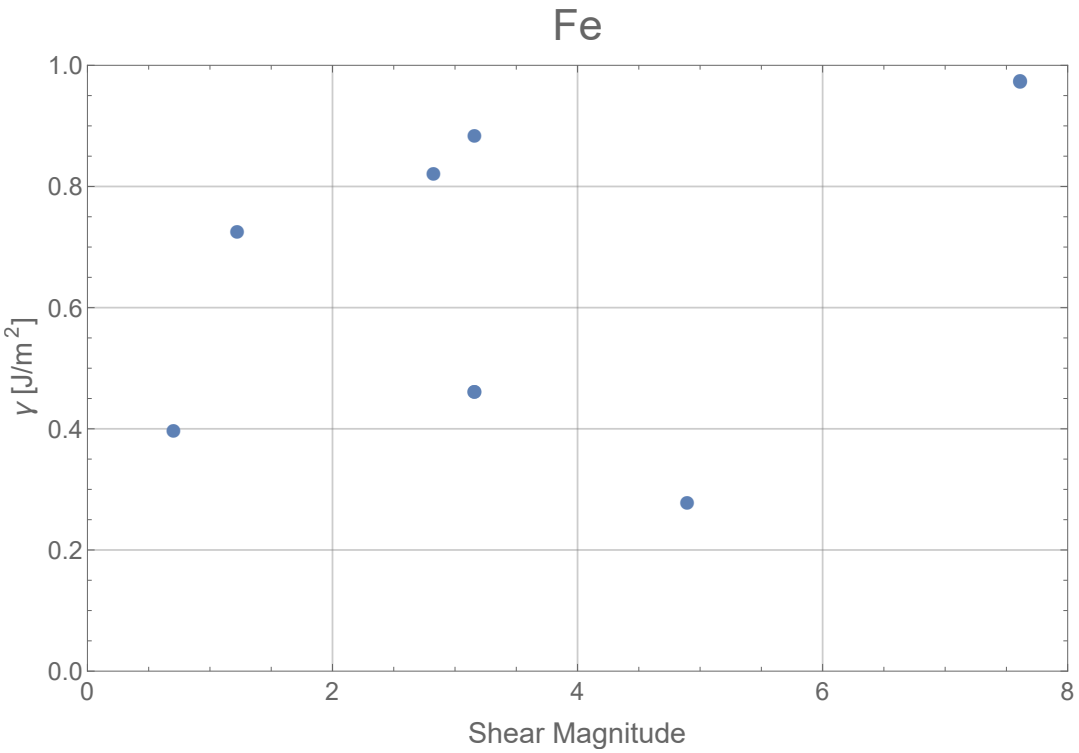

Figure 5.3: Scatterplot of the twin energies for iron (BCC), as detected using the interatomic potential developed in [152]. Cutoffs chosen are $\gamma \leq 1000$ mJ/m^2 and $s \leq 8$ illustrate the sparsity of low-energy twin modes relative to magnesium.

In this case, many of the twin modes for these materials have a very high interface energy (above the cutoff window chosen for the plots), which would them unlikely to be visualized. In the plot window itself, we see very few twin modes. This is an important argument as to why the investigation of the energetics is necessary; like the case for HCP materials, the kinematic framework seems to predict a significant number of potential twin modes in the cubic materials. Unlike in HCP materials, the energetic landscape of these twins is much less diverse, with most twins having significantly higher energy than their HCP counterparts. This, along with the observation in Section 3.4 that shear magnitudes are much more discrete and have a greater magnitude, coincide with the general notion that twinning is much more of a dominant mechanism in HCP materials than in cubic materials.

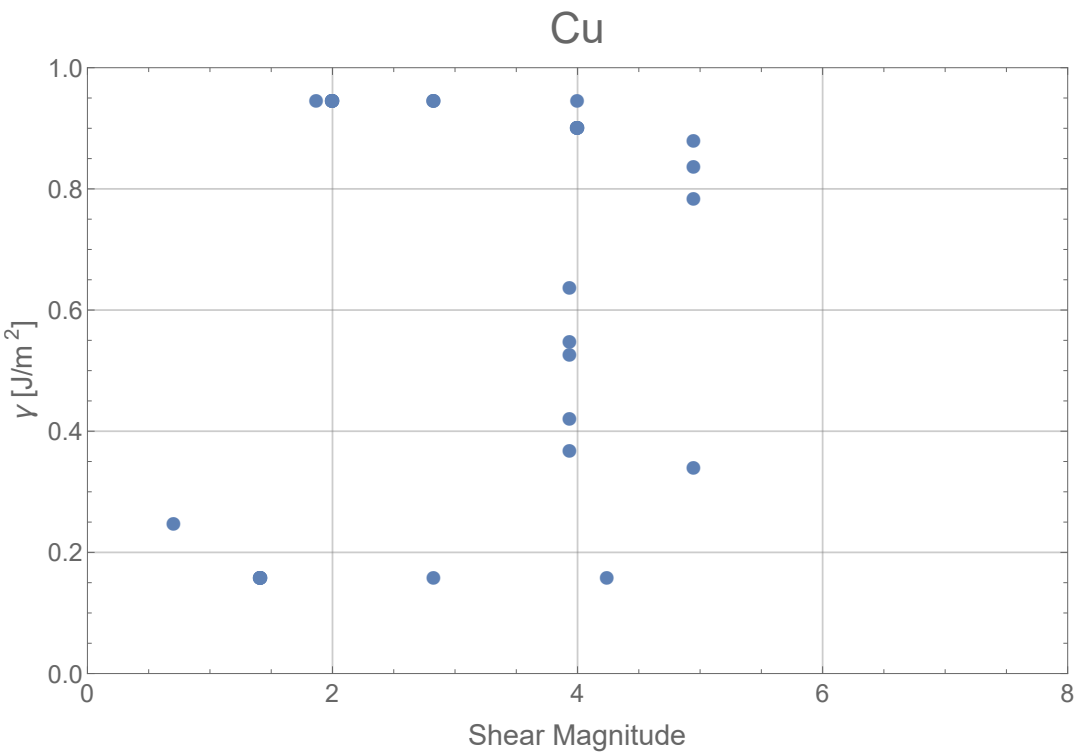

Figure 5.4: Scatterplot of the twin energies for copper (FCC), as detected using the interatomic potential developed in [154]. Cutoffs chosen are $\gamma \leq 1000$ mJ/m^2 and $s \leq 8$ illustrate the sparsity of low-energy twin modes relative to magnesium.

HCP Alloys

Finally, we turn our attention towards HCP alloys. Specifically, we examine magnesium alloyed with an increasing weight percentage of aluminum, as aluminum is a major constituent in many of the magnesium alloys, such as AZ31, that are being considered for applications today. For good measure, we also investigate titanium alloyed with an increasing weight percentage of aluminum. A slight modification to the calculation procedure for alloys is presented in Algorithm 5.1.

Perfect Crystal Calibration

Unlike the previous procedure with perfect crystal calibration presented in Section 5.2, additional measures need to be taken when dealing with solute atoms. Instead of using 32-atom samples as was done with pure magnesium, the randomization and presence of solute atoms can have a drastic effect on the energies depending on their location. Consequently, the perfect crystal calibrations were now done with 2048 atoms to balance speed of calculation against accuracy. With 2048-atom samples, and 100 solute atom locations done per parameter set, it was discovered that the standard

Algorithm 5.1 Modifications suitable for computing twinning energies for alloys.

1: **function** ALLOY MODIFY($\boldsymbol{s}, \hat{\boldsymbol{n}}, \boldsymbol{\sigma}^{\max}$) ▷ Administer changes to introduce solute particles.
2: **for all** Twin modes **do**
3: Identify number of solute elements N_s.
4: Use N_s when creating the simulation `box` to account for element types.
5: Initialize simulation box and lattices otherwise as normal.
6: Compute appropriate volume fraction V_i of atoms to convert based on weights of alloying elements.
7: After the `group` command on regions, convert V_i of elements in the regions to the solute element types.
8: If random solute atom locations are desired, then choose a seed number.
9: Identify the elements when pointing to the directory containing the parameters and coefficients for interatomic potentials.
10: Complete remainder of computations as necessary.
11: **end for**
12: **end function**

deviation of the computed perfect crystal cohesive energies was on the order of 0.001 eV/atom, which is three orders of magnitude less than the actual perfect crystal cohesive energy computed for these alloyed systems. No changes were necessary for the subsequent calculations, as all atomistic simulations for the interface energy and onwards were designed to contain at least 6000 atoms within the sample.

Twin Interface Energy

We make use of the potential for Mg-Al systems developed by Zope and Mishin [156] and execute Algorithm 4.3. We plot γ^{tw} against the s up to 7 wt.% aluminum, in increments of 1 wt.% in Figure 5.5. In Table 5.5, we also tabulate the energies of the classical tension and compression twins as aluminum is added into the system.

For good measure, we also repeat the calculations for Ti-Al systems, also with increasing weight percentage aluminum. Although concepts are also described in [157], we make use of the potential for Ti-Al developed by Mendelev *et al.* [158]. Once again, we plot γ^{tw} against the s up to 7 wt.% aluminum, in increments of 1 wt.% in Figure 5.6. We also tabulate the twin interface energies for the tension and compression twins with changing wt.% aluminum in Table 5.6.

We see that, in both magnesium and titanium, the addition of aluminum eventually causes an increase in the twin interface energy, although it rises much more uniformly in titanium than in magnesium. This suggests that twinning would gradually become

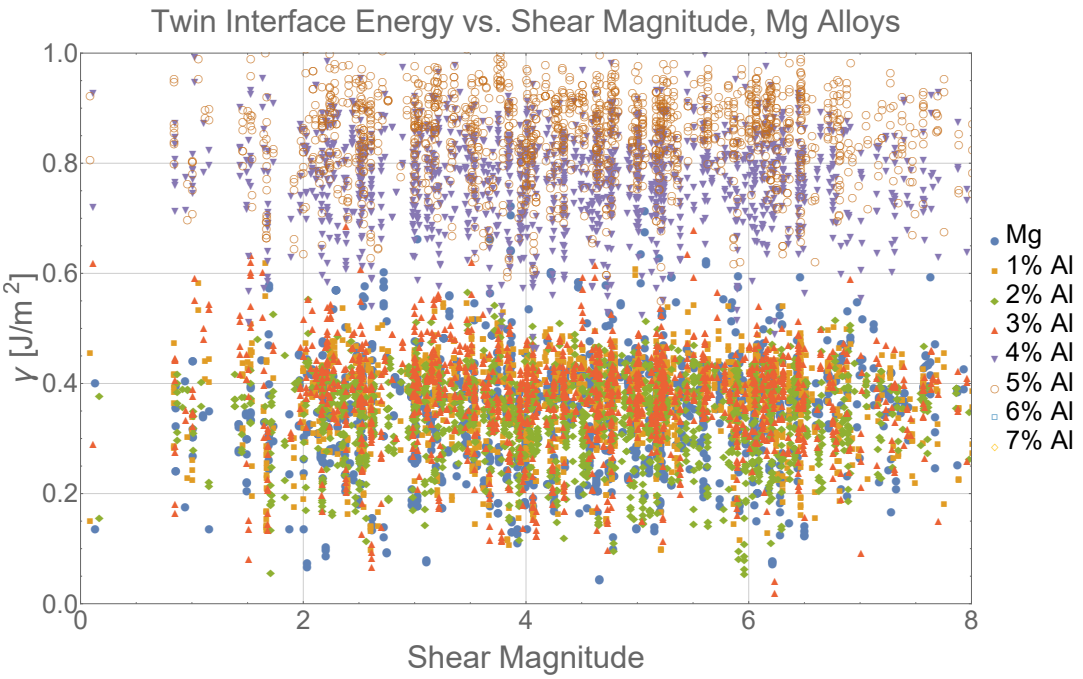

Figure 5.5: Scatterplot of the twin energies for magnesium with n weight percent aluminum, as detected using the EAM potential. Cutoffs chosen are $\gamma \leq 1000\,\mathrm{mJ/m^2}$ and $s \leq 8$ to capture the energies of previously-observed twin modes.

% Al	γ_a [mJ/m^2]	γ_b [mJ/m^2]
0	137.0	222.0
1	150.0	288.7
2	157.2	377.9
3	292.2	409.7
4	721.7	785.8
5	807.7	886.6
6	2411.5	2504.2
7	2733.4	2764.4

Table 5.5: Tabulation of twin interface energy for the tension (a) and compression (b) twins for changing weight percentages of aluminum in magnesium.

energetically unfavorable as the amount of aluminum in the system increases. Before we can really draw any further conclusions, let us briefly examine the stacking fault energies of the materials.

Comparison to Stacking Fault Energies

For the stacking fault energies, we use the values of a and c obtained from training the interatomic potential and induce a $(0001)\langle 11\bar{2}0\rangle$ stacking fault. For a 4096-atom

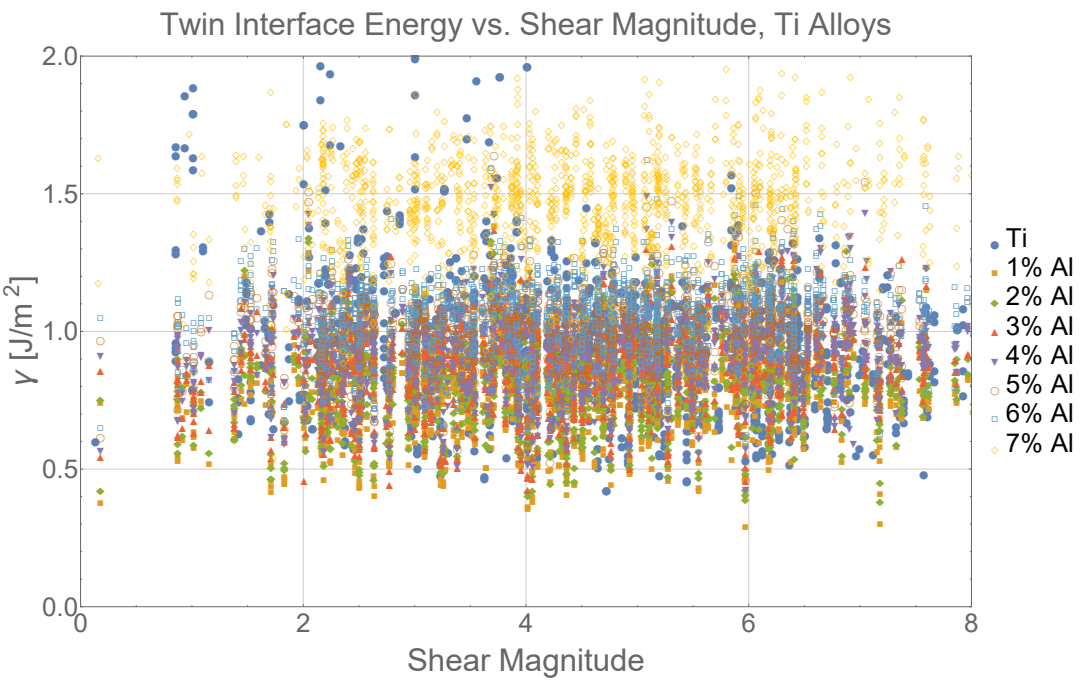

Figure 5.6: Scatterplot of the twin energies for titanium with n weight percent aluminum, as detected using the EAM potential. Cutoffs chosen are $\gamma \leq 1000$ mJ/m^2 and $s \leq 8$ to capture the energies of previously-observed twin modes.

% Al	γ_a [mJ/m^2]	γ_b [mJ/m^2]
0	600.4	677.1
1	377.2	879.0
2	422.4	920.1
3	546.2	667.7
4	568.6	824.9
5	614.7	901.9
6	647.0	927.4
7	1180.4	1220.6

Table 5.6: Tabulation of twin interface energy for the tension (a) and compression (b) twins for changing weight percentages of aluminum in titanium.

sample, we then randomize the location of the solute atoms over 100 iterations in order to ensure that our results account for a variety of solute atom distributions. We then report the mean stacking fault energy over these 100 iterations in Table 5.7.

Interestingly, we see that increasing the weight percentage of aluminum actually decreases the stacking fault energy reported. Intuitively, this would promote twinning; however, also see from Figures 5.5 and 5.6 that the twin interface energies are also increasing with the weight percentage of aluminum introduced into the system. This

wt. % Aluminum	SFE, Mg [mJ/m^2]	SFE, Ti [mJ/m^2]
1	39.0	27.2
2	35.3	23.8
3	31.6	20.9
4	28.0	18.3
5	24.0	16.0
6	20.4	14.0
7	16.8	12.3

Table 5.7: Values of the stacking fault energy for magnesium and titanium with increasing weight-percentage aluminum, using the interatomic potentials developed in [156] for Mg-Al and [158] for Ti-Al.

suggests that, although the lowered stacking fault energy would promote twinning, the twins themselves are becoming more energetically unfavored; at the higher weight percentages of aluminum, there must be some additional mechanisms which are accommodating deformation.

It should be further noted that these results are preliminary and would require a further, thorough investigation — perhaps using verification with density functional theory — before decisive conclusions could be drawn.

5.6 Barriers to Formation: Magnesium

From Figure 5.1, we choose a region of $\gamma \leq 325$ mJ/m^2 and $s \leq 4$ since it encompasses the five previously-observed twin modes. This results in a set of 229 twin modes whose barriers we need to study. We then apply Algorithm 4.4 in order to compute the energetic barriers. The attempt frequencies and consequent Arrhenius relations are captured, and a subset of the results (the 20 systems for which $\gamma \leq 300$ mJ/m^2 and $s \leq 2$) are shown in Arrhenius form in Figure 5.7 over the range of 200 to 1200 K, thus encompassing a region of reasonable use for magnesium up through the melt temperature.

We also tabulate this information in Table 5.8 by updating Table 5.3 with information on the maximum energetic barrier obtained and also the attempt frequency. The results show us that, of the twelve example modes that were selected in the previous part, most have competitive twin barriers and attempt frequencies relative to each other, and especially to the classically-observed modes.

Even though we are only showing results for 20 of the 229 modes for which we performed our nudged elastic band calculation, the general trend holds throughout;

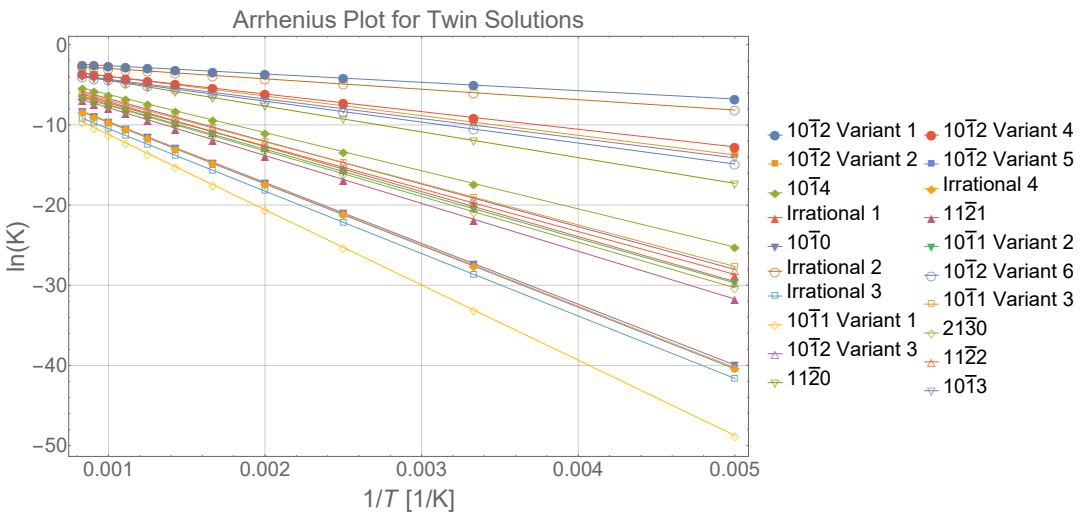

Figure 5.7: Arrhenius plot of up to 1200 K for the 20 modes that are within the region $\gamma \leq 300$ mJ/m^2 and $s \leq 2$.

i	Twin $\{K_1\}\langle\eta_1\rangle$	s	θ	γ^{tw} [mJ/m^2]	ΔE [eV]	ν_0
a	$\{10\bar{1}2\}\langle10\bar{1}1\rangle$	0.1299	180	137.0	0.0896	0.2086
b	$\{10\bar{1}1\}\langle10\bar{1}2\rangle$	1.4919	180	222.0	0.8084	0.1619
c	$\{21\bar{3}0\}\langle10\bar{1}0\rangle$	1.7321	180	297.4	0.4461	0.1689
d	$\{11\bar{2}0\}\langle0001\rangle$	1.8743	180	242.2	0.3221	0.2058
e	$\{21\bar{3}2\}\langle10\bar{1}0\rangle$	2.0343	180	68.8	0.3001	0.2024
f	$\{10\bar{1}3\}_{\text{I}}\langle50\bar{5}4\rangle_{\text{I}}$	2.1568	180	275.4	0.6517	0.2372
g	$\{21\bar{3}0\}\langle10\bar{1}1\rangle$	2.3738	180	271.8	0.3507	0.2103
h	$\{15, 8, \overline{23}, 1\}_{\text{I}}\langle10\bar{1}1\rangle$	2.3773	159.3	290.1	0.6900	0.1226
i	$\{31, 1, \overline{32}, \overline{29}\}_{\text{I}}\langle10\bar{1}1\rangle$	3.0245	159.3	309.6	0.8424	0.1823
j	$\{11\bar{2}1\}_{\text{I}}\langle10\bar{1}1\rangle$	3.1921	159.3	250.6	0.4361	0.1573
k	$\{30\bar{3}4\}_{\text{I}}\langle10\bar{1}3\rangle_{\text{I}}$	3.4703	180	271.4	0.2401	0.2717
l	$\{10\bar{1}2\}_{\text{I}}\langle40\bar{4}5\rangle_{\text{I}}$	3.7584	180	266.2	0.6210	0.1412

Table 5.8: Updated details on twelve example twin systems with $\gamma^{\text{tw}} \leq 325$ mJ/m^2 and $s \leq 4$ from Table 5.3, with information now including the barrier and attempt frequency.

the barriers to formation for all of the twin systems are competitive relative to each other, and especially with respect to the modes that have been previously-observed. There are no curves in Figure 5.7 which have a significantly steeper slope; this indicates that most of the twins have relatively similar energetic barriers to formation.

Volumetric Loads on Samples

We are interested in investigating effects on a sample that has been subjected to a load, and want to study how the barriers to formation are affected. Since it is not the

primary focus of our investigation, we assume that deformations are volumetric in nature for simplicity. That is, we assume a deformation gradient

$$\boldsymbol{F} = (1 + \epsilon)\boldsymbol{\delta} \tag{5.1}$$

and apply this to the lattice vectors at the onset of the formulation. For the Arrhenius plots, due to the costly nature of these calculations and our interest to keep the plots relatively clean, we retain our study of samples under load to the 20 twin modes with $\gamma \leq 300$ mJ/m^2 and $s \leq 2$.

Tension

We first examine the effects of applying a volumetric expansion to the samples, i.e. $\epsilon > 0$ in Equation (5.1). We deform the samples in increments of 0.5% tensile volumetric strain up to 5%, except in the early stages, where we also include 0.1% and 0.2%. For compactness, we only show the results up to 2% tensile volumetric strain in Figures 5.8-5.11.

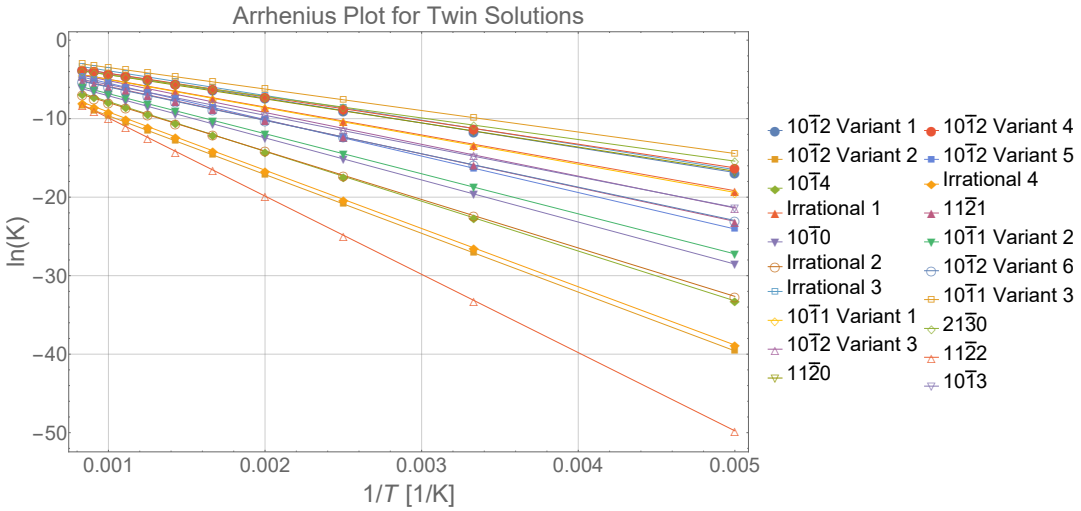

Figure 5.8: Arrhenius plot of up to 1200 K for the 20 modes that are within the region $\gamma \leq 300$ mJ/m^2 and $s \leq 2$, subjected to 0.1% tension.

The Arrhenius plots of samples under tension show that there is quite a bit of shifting of which twin modes have a greater frequency of visualization than others when tensile load is applied. It should also be noted that, as a whole, the barriers to formation generally appear to be lowered with a greater tensile load applied to the sample. This is denoted by the fact that $\ln[K]$ has a generally smaller magnitude at 5% tension compared to the Figure 5.7. Furthermore, most of the barriers are shifted to be closer together, as the curves tend to be more grouped at 5% compared to the no-load case.

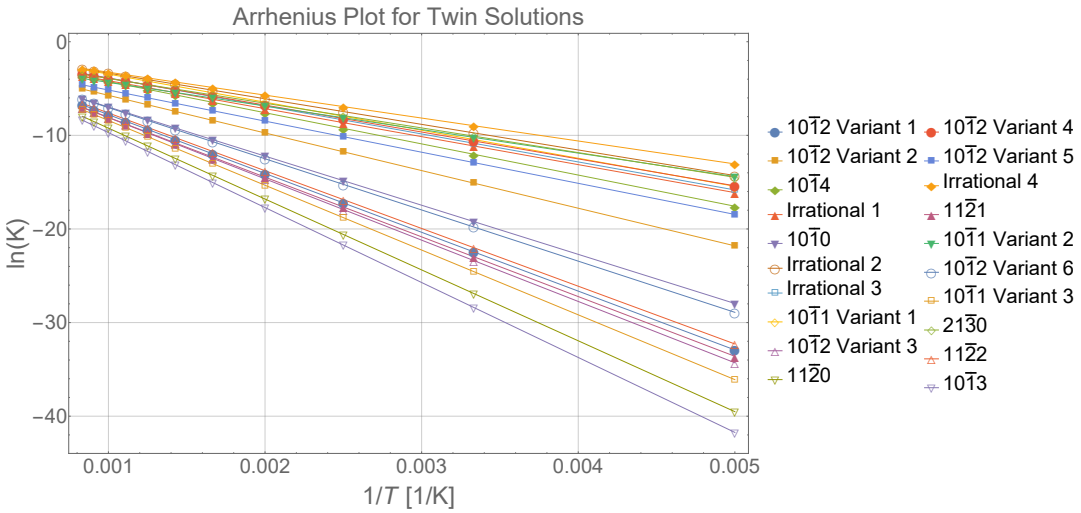

Figure 5.9: Arrhenius plot of up to 1200 K for the 20 modes that are within the region $\gamma \leq 300$ mJ/m^2 and $s \leq 2$, subjected to 0.2% tension.

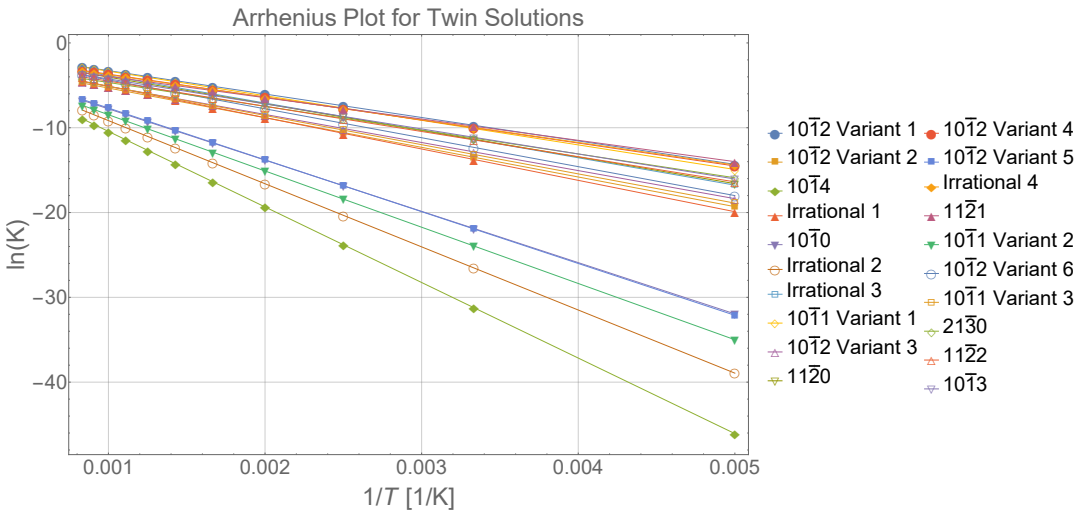

Figure 5.10: Arrhenius plot of up to 1200 K for the 20 modes that are within the region $\gamma \leq 300$ mJ/m^2 and $s \leq 2$, subjected to 0.5% tension.

Compression

We also perform volumetric compression on the sample, i.e. $\epsilon < 0$ in Equation (5.1). We deform the samples in increments of 0.5% compressive volumetric strain up to 5%, except in the early stages, where we also include 0.1% and 0.2%. Again, for compactness, we only show the Arrhenius plots here up to 2% compressive volumetric strain in Figures 5.14-5.17.

The Arrhenius plots of samples under compression also show that there is quite a bit of shifting of which twin modes have a greater frequency of visualization. However,

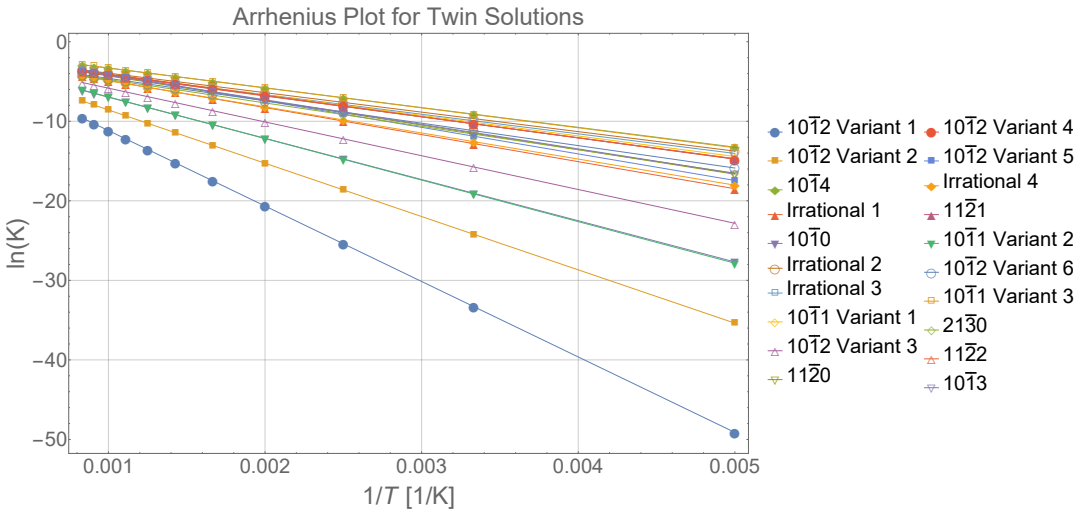

Figure 5.11: Arrhenius plot of up to 1200 K for the 20 modes that are within the region $\gamma \leq 300$ mJ/m^2 and $s \leq 2$, subjected to 1% tension.

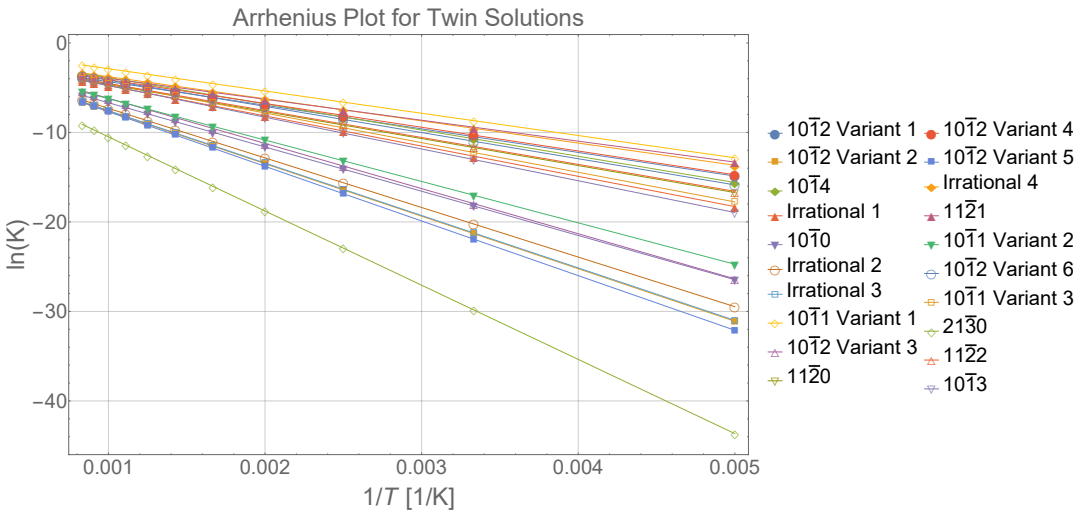

Figure 5.12: Arrhenius plot of up to 1200 K for the 20 modes that are within the region $\gamma \leq 300$ mJ/m^2 and $s \leq 2$, subjected to 1.5% tension.

unlike the case with tensile loads, it appears that compressive loads generally separate out which twins are favored from the others; the highest curves of $\ln[K]$ at 5% compression are not that different from 5% tension (though the modes are), but the curves are generally spread out over a much greater range, the plot window is significantly larger for compression.

In general, we can argue that applying loads to the sample will not only affect the overall barriers to twinning, but will also dictate which modes are more dominant than others. Though the dominant modes change at different loads, what is clear is that the

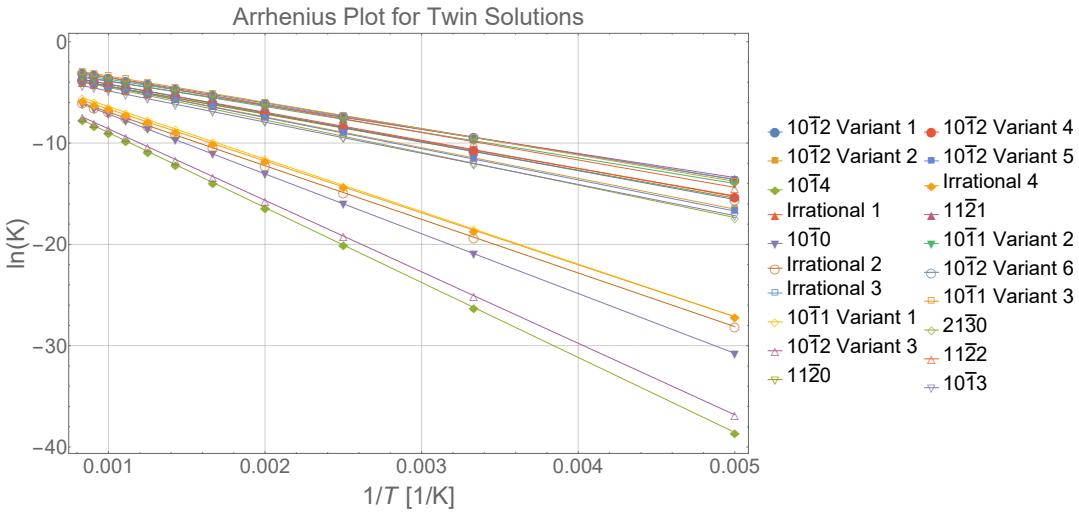

Figure 5.13: Arrhenius plot of up to 1200 K for the 20 modes that are within the region $\gamma \leq 300$ mJ/m^2 and $s \leq 2$, subjected to 2% tension.

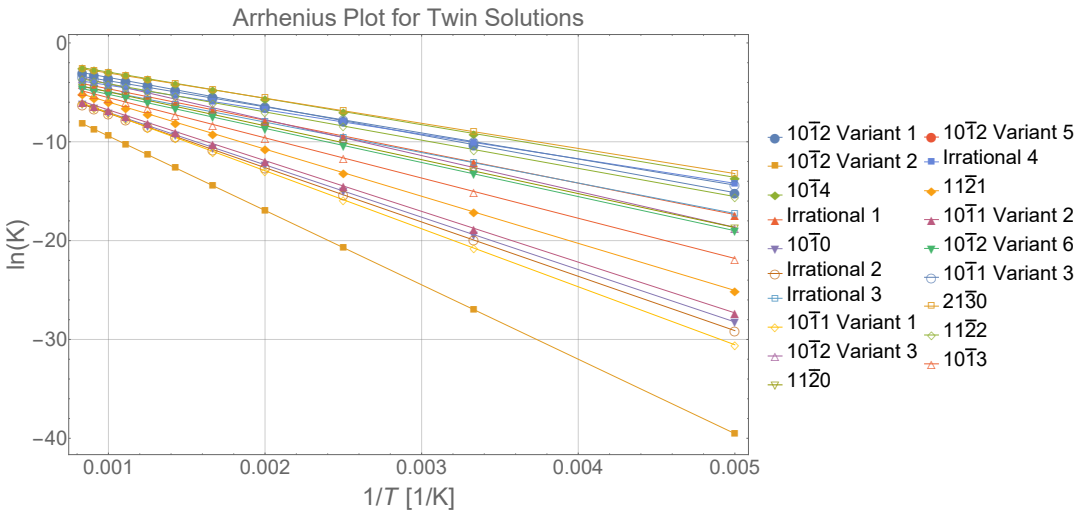

Figure 5.14: Arrhenius plot of up to 1200 K for the 20 modes that are within the region $\gamma \leq 300$ mJ/m^2 and $s \leq 2$, subjected to 0.1% compression.

barriers for different twins respond differently to load. Moreover, our investigation suggests that the overall barriers to twinning are reduced under tension more so than in compression.

5.7 Summary

In this chapter, we studied the energetics of the twins predicted for magnesium. What we saw was that, like the kinematic predictions, the energetic landscape of the twins is also very complicated. From just examining the twin interface energy of bulk magnesium in Figure 5.1, we saw that there are actually a significant number of twin

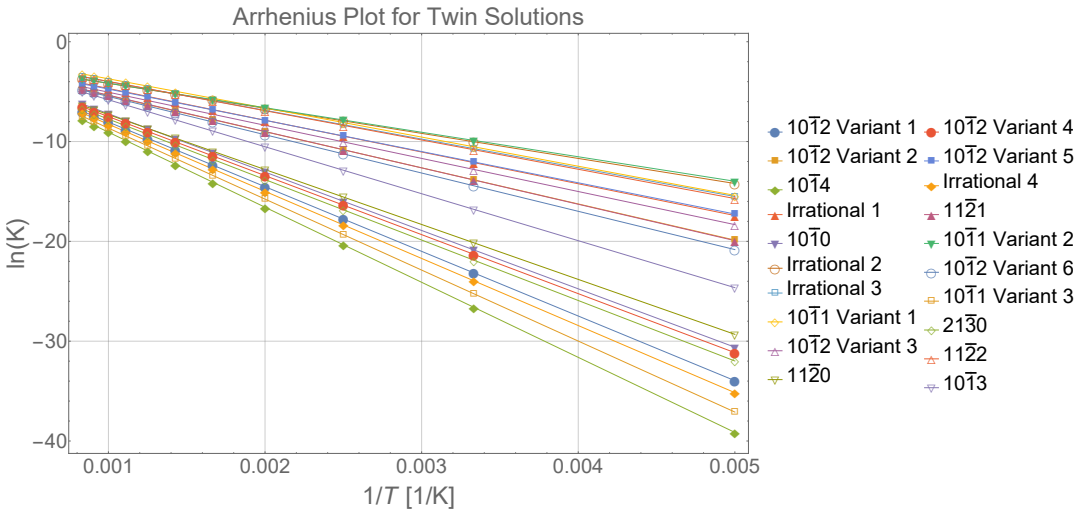

Figure 5.15: Arrhenius plot of up to 1200 K for the 20 modes that are within the region $\gamma \leq 300$ mJ/m^2 and $s \leq 2$, subjected to 0.2% compression.

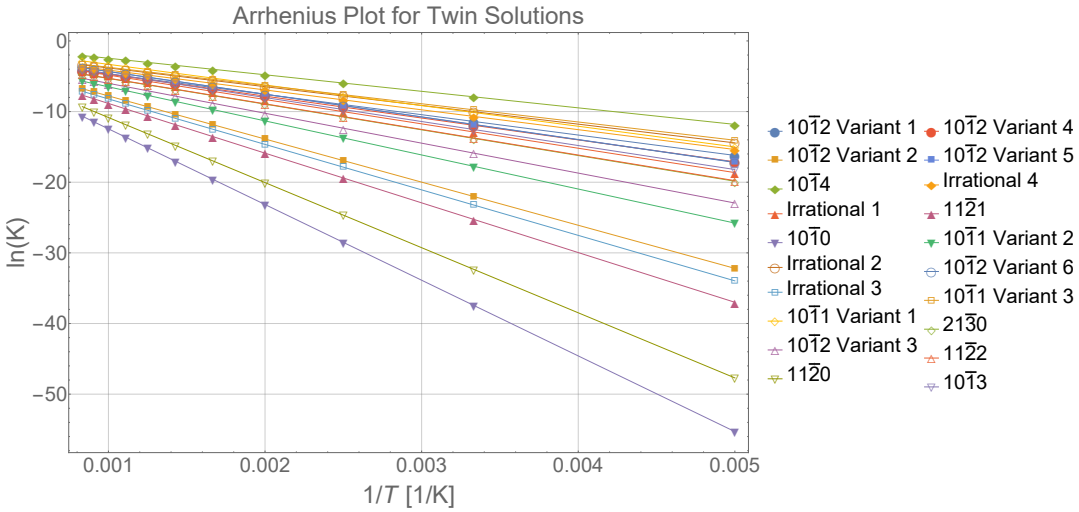

Figure 5.16: Arrhenius plot of up to 1200 K for the 20 modes that are within the region $\gamma \leq 300$ mJ/m^2 and $s \leq 2$, subjected to 0.5% compression.

modes with twin interface energies and twin shear magnitudes comparable to modes that have been previously observed in literature. This suggests that these twins are actually viable and should be kept within consideration. The notion was furthered when we also subjected a large set of these twins with γ^{tw} and s comparable to the previously-observed modes to a nudged elastic band calculation and then found that their barriers are also reasonably competitive.

Along the way, we also considered two additional aspects; loading and solutes. We saw that loading these twin samples and then subjecting them to energetic calculations

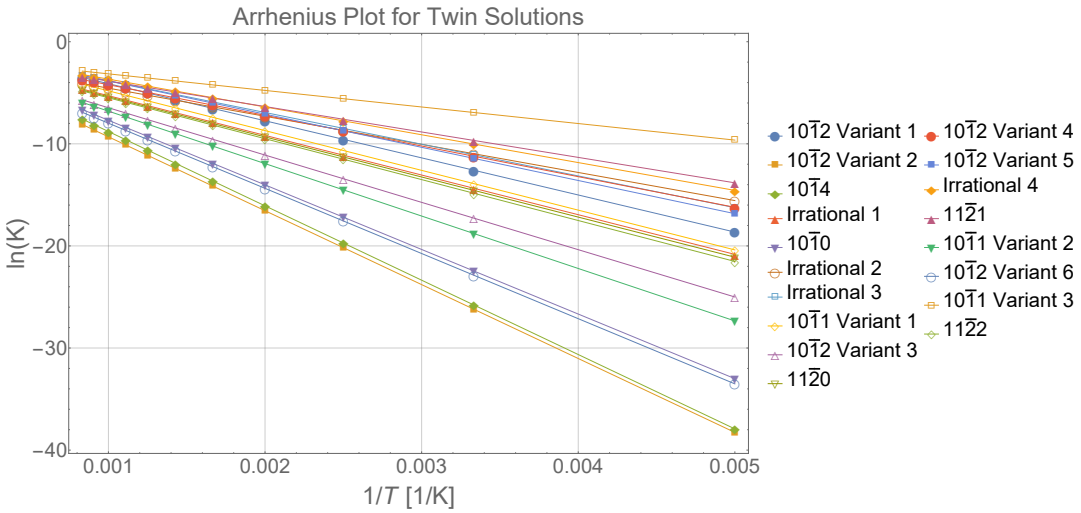

Figure 5.17: Arrhenius plot of up to 1200 K for the 20 modes that are within the region $\gamma \leq 300$ mJ/m^2 and $s \leq 2$, subjected to 1% compression.

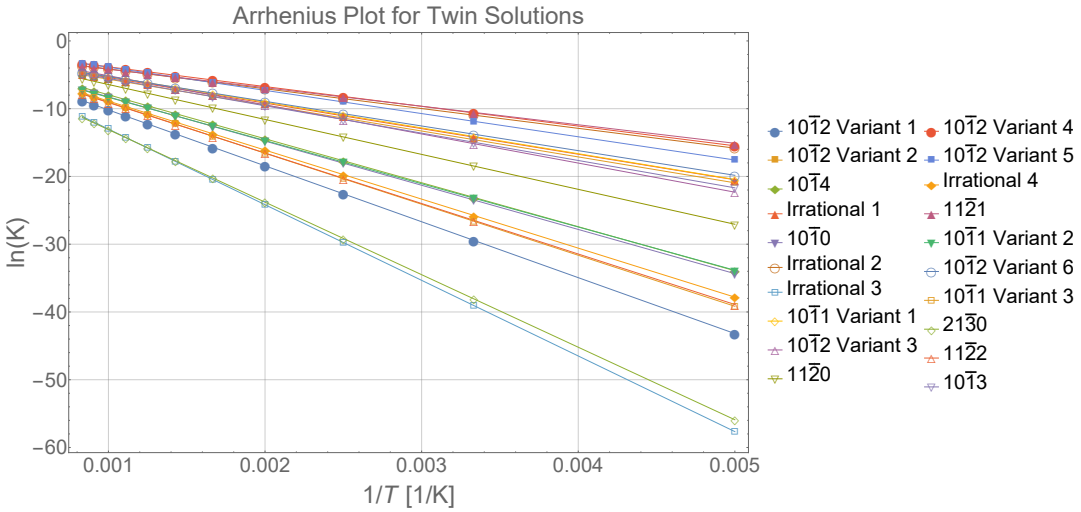

Figure 5.18: Arrhenius plot of up to 1200 K for the 20 modes that are within the region $\gamma \leq 300$ mJ/m^2 and $s \leq 2$, subjected to 1.5% compression.

could drastically change the likeliness to visualize certain modes over others; in this particular case, tension promoted more twins to appear, while compression suppressed certain modes significantly more so than others. Likewise, we also saw that adding solute atoms — in this case, of aluminum — to a bulk material drastically changed the energies of these twins, although more thorough investigations would be necessary in order to draw any definitive conclusions on the effects of alloying.

At the end of this investigation, however, we are still left with the fact that we have a large series of twins that could potentially be considered. Let us now see if there are

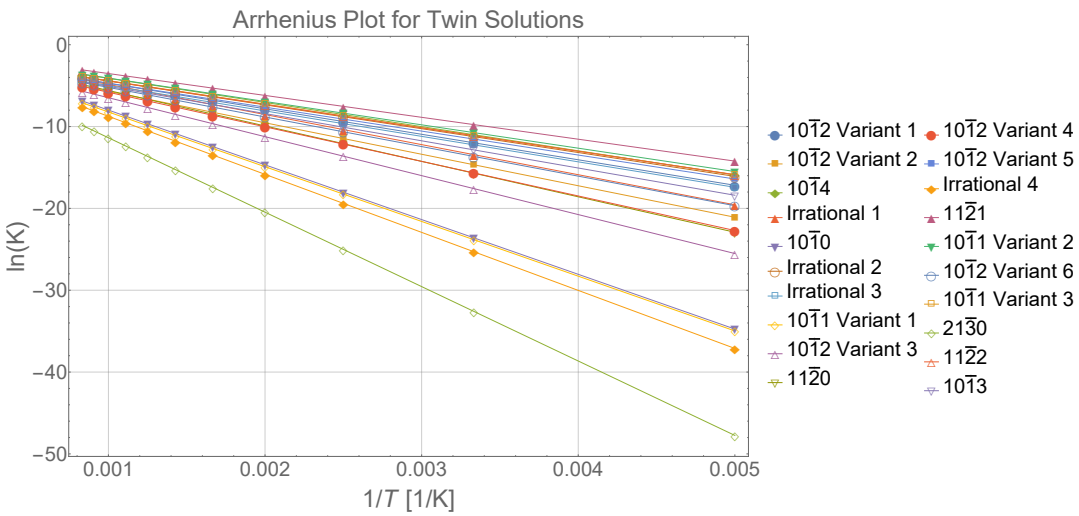

Figure 5.19: Arrhenius plot of up to 1200 K for the 20 modes that are within the region $\gamma \leq 300$ mJ/m^2 and $s \leq 2$, subjected to 2% compression.

any additional metrics which will allow us to eliminate some twin modes and identify the ones which will truly remain pertinent to magnesium.

Chapter 6

YIELD SURFACE CONSTRUCTION

6.1 Goals of the Yield Surface Construction

With the information on twins at the atomistic scale, we now take a final step to close the gap and definitively predict the potential twin modes in magnesium that are relevant to its yield characteristics. We do so by examining the twin modes that are favorable under an applied stress. These favorable modes are then identified as the ones which are most likely to affect magnesium in any given situation of yield.

6.2 Stress and Yield

From the nudged elastic band calculations, we have the energy and stress states of configurations which lie in between the perfect crystal and the final, twinned configuration. Whereas we represented this in Figure 4.1 with the domain being described as the reaction coordinate, we could also sensibly substitute this with the notion of a twinning shear γ, representative of the amount of effective twinning shear that has been applied to the configuration. Then, over the domain of $0 \leq \gamma \leq s$, we have the energy E from the nudged elastic band calculations. However, we also have the state of stress derived from those calculations; let us temporarily represent stress with τ. Since stress can be related to the derivative of energy, we arrive at the schematic illustration of the barrier shown in Figure 6.1.

This notion is important: at the inflection point in curve $\mathsf{E}[\gamma]$, our stress state should peak, and thus we have this notion of the maximum stress experienced by the system as it is attempting to form a particular twin. Consequently, we need to make use of some reasonable notion of stress. At the atomic scale, the primary measure of stress is the *virial stress*, which is given by

$$\sigma_{ij}^{\text{vir}} = \frac{1}{\Omega} = \sum_{k \in \Omega} \left[-m^k (v_i^k - \bar{v}_i)(v_j^k - \bar{v}_j) + \frac{1}{2} \sum_{l \in \Omega} (x_i^l - x_i^k) f_j^{kl} \right], \tag{6.1}$$

where k and l index atoms in the domain of interest, Ω is the volume of the domain of interest, m^k is the mass of the k^{th} atom, v_i^k is the i^{th} component of the velocity of the k^{th} atom, $\bar{u}_j$ is the j^{th} component of the average velocity of atoms in the volume of interest, x_i^k is the i^{th} component of the position of atom k, and f_i^{kl} is the i^{th} component of force applied on atom k by atom l.

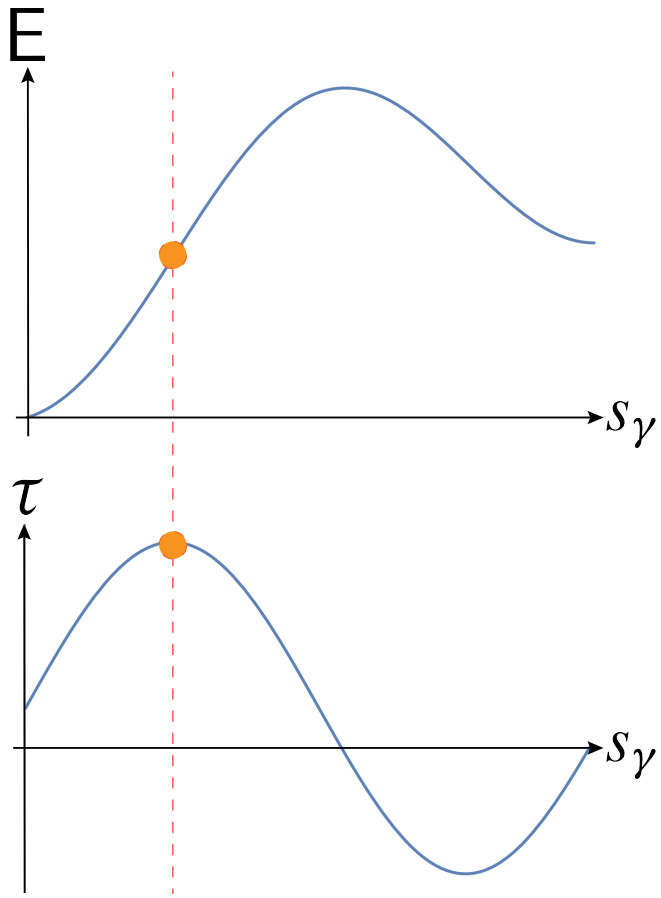

Figure 6.1: Schematic illustration of the maximum barrier state.

With a stress tensor formed, we now wish to consider a measure which would be reasonable in determining when a particular mode would be activated. A stress tensor can be resolved out in directions in order to study its components in a particularly meaningful sense by using the notion of a resolved shear stress, i.e.

$$\tau_{\text{resolved}} = \boldsymbol{d}_1 \cdot \boldsymbol{\sigma} \boldsymbol{d}_2,$$

where $\boldsymbol{d}_1$ and $\boldsymbol{d}_2$ are two directions of interest. Because twinning involves shear, it makes sense to choose the directions of resolution to be the twin plane and the twinning shear, thus giving us the resolved shear stress for twinning as

$$\tau_i^j = \hat{\boldsymbol{s}}^i \cdot \boldsymbol{\sigma}_j^i \hat{\boldsymbol{n}}^i, \tag{6.2}$$

where $\hat{\boldsymbol{s}}$ represents the normalized twinning shear (only normalized here because we only want its direction and do not want to affect the magnitude of the resolved shear stress calculated), and $\hat{\boldsymbol{n}}$ is the twin plane normal. Equation (6.2) is calculated for the i^{th} twin system at the j^{th} replica. Note that the stress tensor $\boldsymbol{\sigma}$ in this case would be the virial stress tensor extracted at each replica from the nudged elastic band calculations.

Although, for any given twin system and replica, we could compute the resolved shear stress, we actually seek a single measure for the barrier to formation. This is represented by finding the maximum barrier state, i.e.

$$\boldsymbol{\sigma}_Y^i = \max_j \boldsymbol{\sigma}_j^i. \tag{6.3}$$

We then suppose that $\boldsymbol{\sigma}_Y^i$ is the state at which the material "yields", after which it forms the twin mode. Supposing that the *yield stress* for any given twin mode is given by the *critical resolved shear stress* of the twin system, i.e.

$$\sigma_Y^i = \hat{\boldsymbol{s}}_i \cdot \boldsymbol{\sigma}_Y^i \hat{\boldsymbol{n}}_i, \tag{6.4}$$

with no sum on the i, we then have a simple, numerical measure by which we can estimate that a twin will have formed.

6.3 Forming the Yield Surface

Since the yield surface exists in $\mathbb{R}^5$[1], presenting it in a reasonable visualization is not a trivial task. For instance, in order to represent it as a series of two-dimensional yield surface contours, the appropriate slices of the $\mathbb{R}^5$ yield surface need to be taken. Manually, this would be a complicated process, since it would involve trial and error with an exceedingly large number of potential combinations of twin systems, and so a more clever approach is needed.

The considerations from above suggest that a twin system will activate when the component $\tau^i = \hat{\boldsymbol{s}}_i \cdot \boldsymbol{\sigma} \hat{\boldsymbol{n}}_i$ of the applied stress $\boldsymbol{\sigma}$ exceeds the critical value σ_Y^i, i.e. that $\tau^i > \sigma_Y^i$. Therefore, the *elastic domain* is given as

$$\mathcal{Y} = \{\boldsymbol{\sigma} : \boldsymbol{\sigma} = \boldsymbol{\sigma}^{\mathrm{T}}, \mathrm{tr}[\boldsymbol{\sigma}] = 0, \hat{\boldsymbol{s}}_i \cdot \boldsymbol{\sigma} \hat{\boldsymbol{n}}_i < \sigma_Y^i \text{ for } i = 1, \ldots, N\} \tag{6.5}$$

for N being the number of systems that were investigated. We then take the convex hull of all systems in $\mathcal{Y}$, written generically as

$$\mathrm{Conv}[\mathcal{S}] = \left\{ \sum_{i=1}^{|\mathcal{S}|} \alpha_i x_i \;\middle|\; (\forall\, i : \alpha_i \geq 0) \cap \sum_{i=1}^{|\mathcal{S}|} \alpha_1 = 1 \right\}, \tag{6.6}$$

and target the systems with the lowest yield stress, as these would be the ones which are most likely to be activated. The set formed by the convex hull then gives us the *yield surface* for magnesium, since these are the modes which are most likely to form

[1] One of the degrees of freedom is eliminated by the fact that only the deviatoric component of the stress, $\boldsymbol{\sigma}_{\mathrm{dev}} = \boldsymbol{\sigma} - \mathrm{tr}[\boldsymbol{\sigma}]\boldsymbol{\delta}/3$, affects yield.

under an applied load. A quick way to implement the calculation of the yield surface comes from the following. Suppose that we can write

$$\hat{\boldsymbol{s}}_i \otimes \hat{\boldsymbol{n}}_i = \sum_j \alpha_j \hat{\boldsymbol{s}}_j \otimes \hat{\boldsymbol{n}}_j .$$

We can divide both sides of this by the critical resolved shear stress, i.e.

$$\frac{\hat{\boldsymbol{s}}_i \otimes \hat{\boldsymbol{n}}_i}{\sigma_Y^i} = \sum_j \alpha_j \frac{\hat{\boldsymbol{s}}_j \otimes \hat{\boldsymbol{n}}_j}{\sigma_Y^i}.$$

Then,

$$\hat{\boldsymbol{s}}_i \cdot \boldsymbol{\sigma} \hat{\boldsymbol{n}}_i = \sum_j \alpha_j \hat{\boldsymbol{s}}_j \cdot \boldsymbol{\sigma} \hat{\boldsymbol{n}}_j .$$

Using the same notion as before of normalizing by the critical resolved shear stress,

$$\frac{\hat{\boldsymbol{s}}_j \cdot \boldsymbol{\sigma} \hat{\boldsymbol{n}}_j}{\sigma_Y^j} \ \forall \ j. \tag{6.7}$$

Since Equation (6.7) must hold for all j, we thus have an expression for which we can calculate the convex hull. Specifically, this says that we can eliminate the i^{th} system and only need to consider the reduced set that constitutes the convex hull.

Relating this back to our investigation of twin modes, not all N systems may participate in determining the elastic domain, since the presence of one system may suppress the presence of some of the others. Therefore, the true elastic domain can be written as

$$\mathcal{Y} = \{\boldsymbol{\sigma} : \boldsymbol{\sigma} = \boldsymbol{\sigma}^T, \text{tr}[\boldsymbol{\sigma}] = 0, \hat{\boldsymbol{s}}_i \cdot \boldsymbol{\sigma} \hat{\boldsymbol{n}}_i < \sigma_Y^i \text{ for } i = 1, \ldots, n\}. \tag{6.8}$$

with $n < N$. As such, only a small number of twin systems from the relatively large calculated set actually affect yield behavior for the material.

6.4 Procedure for Magnesium

For magnesium, to construct the yield surface, we also need to incorporate the magnitudes of the slip systems from Figure 1.7. The magnitudes of the critical resolved shear stress we take are based on values found through literature, which are summarized in Table 6.1.

6.5 Implementation: Yield Surface Construction

We will now summarize the procedure of this chapter in algorithmic form. Once completed, we will have a list of the twin modes which are predicted to affect yield behavior in magnesium.

System	Magnitude [MPa]
Basal	0.52[159]-0.55[160]
Prismatic	39.2[56]
Pyramidal	105[160]

Table 6.1: Values of the critical resolved shear stress of magnesium slip systems

Algorithm 6.1 Procedure for taking stress information and identifying the relevant twin modes.

1: **function** IDENTIFY RELEVANT TWINS($\boldsymbol{s}, \hat{\boldsymbol{n}}, \boldsymbol{\sigma}^{\max}$) ▷ Find twin modes which can be exploited.
2: **for all** Twin modes subjected to nudged elastic band calculation **do**
3: Import the virial stress tensor of the i^{th} at the j^{th} replica, $\boldsymbol{\sigma}_j^{i,\text{vir}}$.
4: Find the maximum stress state following Equation (6.3) and associate it with yield, i.e. $\boldsymbol{\sigma}_Y^i \leftarrow \max_j \boldsymbol{\sigma}_j^i$.
5: Compute the resolved shear stress σ_Y^i using Equation (6.4).
6: **end for**
7: Repeat procedure and set up the slip systems from Table 6.1.
8: Perform convex hull analysis in order to find the systems which bound the elastic domain.
9: Form the elastic domain $\mathcal{Y}$ using Equation (6.5).
10: **Store:** All information about twin modes which lie on the yield surface.
11: **end function**

6.6 Summary

In this chapter, we introduced a methodology to identify which twin modes would be relevant to magnesium under stress. Now that we have developed the tools, let us actually apply the methodology and observe what it says about the twin modes in magnesium.

Chapter 7

RESULTS: YIELD SURFACE CONSTRUCTION

7.1 Goals of this Chapter

Having laid out the fundamental concepts of the yield surface construction, we will now plot out the computed yield surfaces for magnesium, using the 229 twin modes in the region of $\gamma \leq 325$ mJ/m^2 and $s \leq 4$ that was used for the nudged elastic band calculations. Note that, although we explored some concepts of loaded samples in Section 5.6, we will return to the case of no external loading applied to the sample, and make observations on the yield surface behavior based off of that.

7.2 Check: CRSS of the Tension Twin

As a check of our construction, we compute the critical resolved shear stress for the tension twin system. The value of 20.8 MPa that we calculate is in good agreement with the previously-obtained value of 18 MPa from [160]. This agreement instills confidence that our implementation is reasonable, and so we proceed with the construction of the rest of the yield surface for magnesium.

7.3 The Updated Magnesium Yield Surface

We now examine a variety of slices of the magnesium yield surface created for this study by executing Algorithm 6.1. Unlike previous models of magnesium, we are now considering 229 twin modes in order to look at the effects of various twin modes on the yield surface. The yield surface is a set in five-dimensional deviatoric space. To understand this set, plot some interesting two-dimensional slices of the twin yield surface with these new considerations. In each slice, the axes represent a particular component of stress, e.g. $\sigma_a = \hat{\boldsymbol{s}}_a \cdot \boldsymbol{\sigma} \hat{\boldsymbol{n}}_a$, i.e. we are looking at the stress for mode a. The subscript letters are representative of the different modes which are tabulated in Table 7.1. Note that the shaded blue zone will be representative of the elastic domain of the material for a particular slice; the curves that bound it thus form the yield surface.

We first observe a fairly classical-looking slice in Figure 7.1. Figure 7.1 shows what would be consistent with the original picture that existed going into this study of magnesium; the yield surface for magnesium is dominated by basal slip and the tension twin (mode a) in this particular slice. We also observe the relevance of

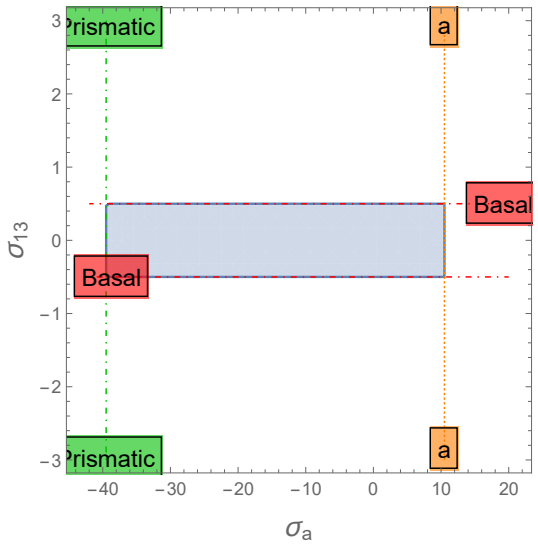

Figure 7.1: Representative slice of the magnesium yield surface which would be more indicative of a classical picture, with the classical tension twin mode dominating the yield surface, alongside traditional slip systems. Exact information on the tension twin is represented in Table 7.1

prismatic slip. Note that all of the additional twin modes do not impinge on the yield surface, as classical views of twinning in magnesium would lead us to believe.

The picture becomes slightly more interesting when we start to delve into additional slices of the magnesium surface. Figure 7.2 shows one such example; here, we now see that the yield surface — though still dominated by basal and prismatic slip — is now limited on one side by mode l, which is representative of one of the irrational twin modes, with several additional modes lying very near the yield surface in a clumped fashion. Combining this with our earlier NEB calculations under stress (Section 5.6) suggest a high possibility that some of these modes which lie very near the yield surface in Figure 7.2 could become the dominant modes under stress, which would be in agreement with what we saw in those NEB calculations.

The most interesting representations of the magnesium yield surface are seen in Figures 7.3; in these slices, we have very non-classical twin modes dominating the yield surface. For instance, in the case of the top left panel, we see two twin modes dominating the yield surface alongside basal slip; mode b is the classical compression twin, while mode c is a non-classical twin. In the other panels, we see the yield surface being entirely governed by prismatic slip and twin modes. In the last panel, we observe one slice which suggests the yield surface being dominated exclusively by twin modes.

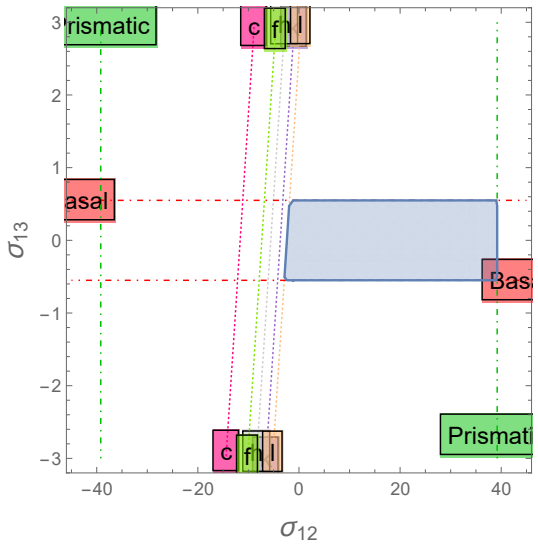

Figure 7.2: A representative slice of the magnesium yield surface in which an irrational twin modes dominates the yield surface. The exact identities of these twins are displayed in Table 7.1

In principle, one could continue to take different slices of the yield surface and tabulate which modes end up participating on the yield surface for magnesium, but this would be an enormously exhausting effort. To expedite the process, we then employ Algorithm 6.1 and then tabulate the twin modes which form the boundary of the elastic domain of magnesium. The results of the tabulation are presented in Table 7.1, whose labels are used to identify the twin modes in Figures 7.1-7.3.

i	Twin $\{K_1\}\langle\eta_1\rangle$	s	θ	γ^{tw} [mJ/m^2]	ΔE [eV]	ν_0	σ_Y [MPa]
a	$\{10\bar{1}2\}\langle10\bar{1}1\rangle$	0.1299	180	137.0	0.0896	0.2086	20.8
b	$\{10\bar{1}1\}\langle10\bar{1}2\rangle$	1.4919	180	222.0	0.8084	0.1619	185.8
c	$\{21\bar{3}0\}\langle10\bar{1}0\rangle$	1.7321	180	297.4	0.4461	0.1689	125.9
d	$\{11\bar{2}0\}\langle0001\rangle$	1.8743	180	242.2	0.3221	0.2058	188.9
e	$\{21\bar{3}2\}\langle10\bar{1}0\rangle$	2.0343	180	68.8	0.3001	0.2024	143.9
f	$\{10\bar{1}3\}_{\text{I}}\langle50\bar{5}4\rangle_{\text{I}}$	2.1568	180	275.4	0.6517	0.2372	63.6
g	$\{21\bar{3}0\}\langle10\bar{1}1\rangle$	2.3738	180	271.8	0.3507	0.2103	186.5
h	$\{15, 8, \overline{23}, 1\}_{\text{I}}\langle10\bar{1}1\rangle$	2.3773	159.3	290.1	0.6900	0.1226	41.8
i	$\{31, 1, \overline{32}, \overline{29}\}_{\text{I}}\langle10\bar{1}1\rangle$	3.0245	159.3	309.6	0.8424	0.1823	355.2
j	$\{11\bar{2}1\}_{\text{I}}\langle10\bar{1}1\rangle$	3.1921	159.3	250.6	0.4361	0.1573	211.6
k	$\{30\bar{3}4\}_{\text{I}}\langle10\bar{1}3\rangle_{\text{I}}$	3.4703	180	271.4	0.2401	0.2717	11.9
l	$\{10\bar{1}2\}_{\text{I}}\langle40\bar{4}5\rangle_{\text{I}}$	3.7584	180	266.2	0.6210	0.1412	11.8

Table 7.1: Details of the twin systems which were found to affect the yield surface of magnesium. The first column is an arbitrary label. System a is the classical tension twin while system b is the classical compression twin. The subscript I denotes an irrational index which has been rounded to a nearby integer.

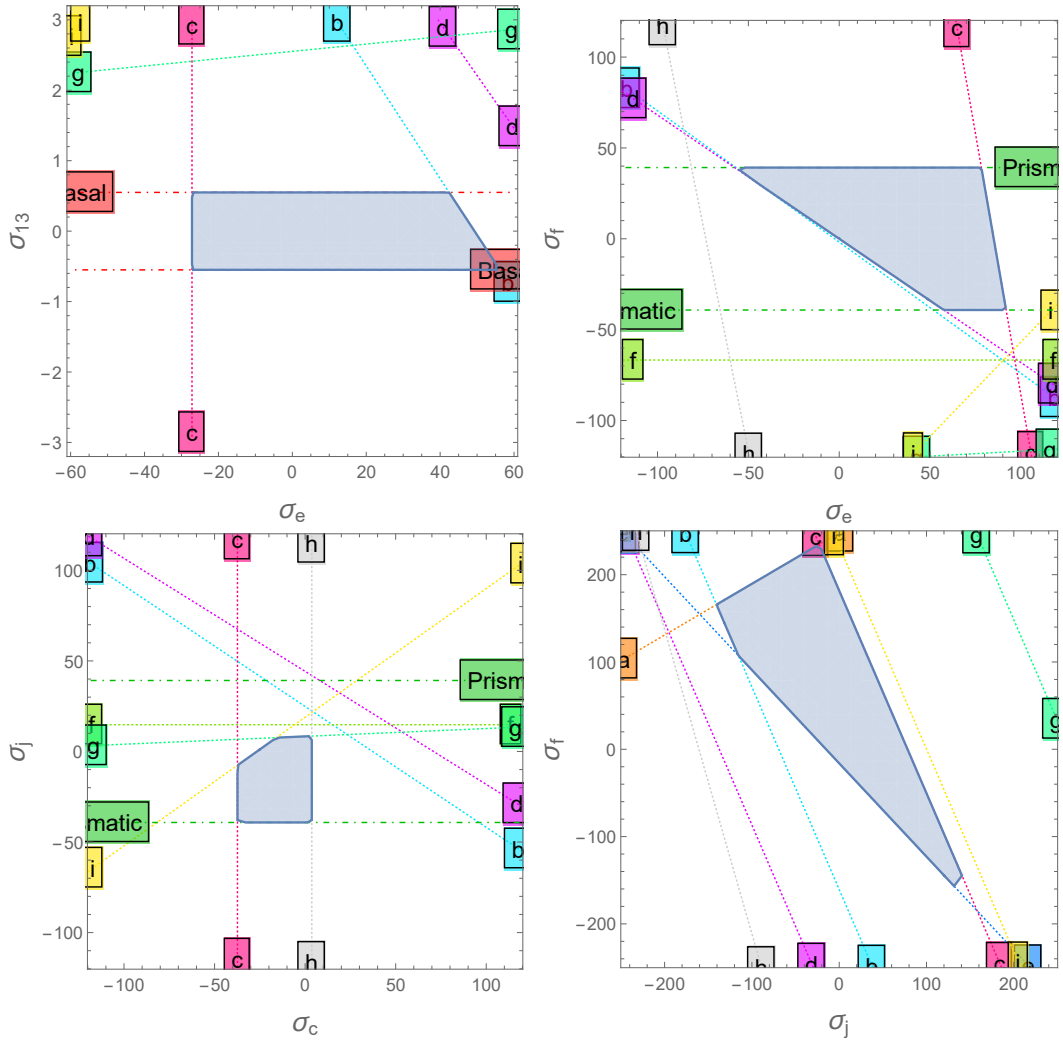

Figure 7.3: Representative slices of the magnesium yield surface in which multiple twin modes now dominate the yield surface. The exact identities of these twins are displayed in Table 7.1

We now see that the twelve modes that we have been following throughout this work were not chosen arbitrarily, but were selected retroactively because they would ultimately become the ones that were calculated to lie on the magnesium yield surface. Table 7.1 shows us that, of the 229 modes that we considered for further analysis in our nudged elastic band and subsequent stress calculations, twelve modes consequently participate on the yield surface for magnesium! As it turns out, these modes include the two classical systems; the classical tension twin is represented as system a, and the classical compression twin is represented as system b. However, there are quite a number of additional twin modes. One immediate observation is that quite a few of these twin modes are irrational in nature, as denoted by the subscript I; many of

these modes are comparable to ones that were previously observed in literature. The locations of these systems on the energy-shear scatterplot are highlighted in orange in Figure 7.4.

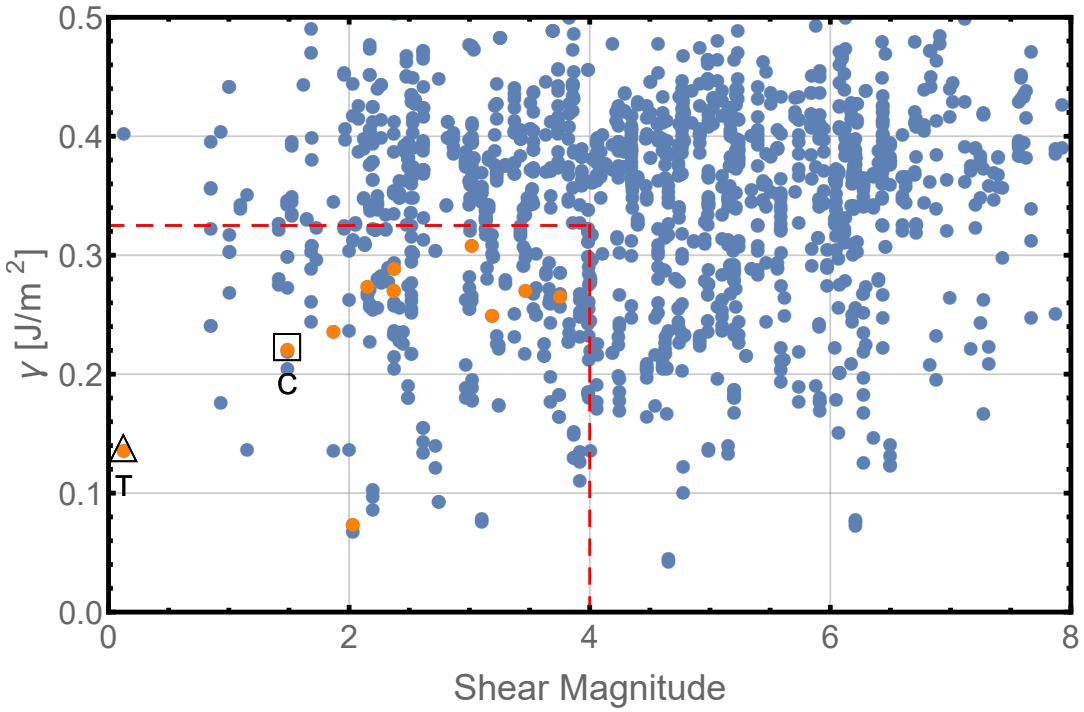

Figure 7.4: Plot of all twin configurations with twin boundary energy γ^{tw} under 500 mJ/m^2 and calculated shear magnitude $s < 8$ using the Modified MEAM potential by Wu *et al.* Red dashed line denotes the boundary of points which were subjected to further nudged elastic band and stress calculation. Orange points denote twin systems which were detected to play a role in the yield surface of magnesium. The tension (T) and compression (C) twins are also highlighted.

Figure 7.4 informs us that even some twin modes with shear magnitudes that were previously-presumed to be too large are also predicted to lie on the yield surface for magnesium. A significant portion of the orange points arise from shear magnitudes in excess of two.

Continuing with our observations of the twin modes that are predicted to lie on the yield surface, we also observe that, unfortunately, not all of the previously-observed modes are exactly predicted as lying on the yield surface of magnesium. However, we do find that there are a few irrational modes whose orientations are reasonably close to these modes which have been previously observed in literature, which leads us to believe that potential discrepancies or limitations in visualization technique may be responsible for the slight mismatches in prior observations and our predictions.

Still, it would be interesting to attempt this calculation again sometime down the line when advancements in computation — in terms of both speed and memory — will make for an easier calculation of all of these quantities. One should remember that the twelve modes which were concluded to lie on the magnesium yield surface only arose from a study of 229 modes; it is entirely within the realm of possibility that enlarging this initial set would result in a potentially different set of twin modes being selected for the yield surface of magnesium, and this new set might better match with prior observations in literature. It would also be interesting to see just how much loading a sample and introducing solute atoms would affect these yield surfaces.

However, it should be stressed that the list of twelve modes may not necessarily reflect the exact modes that will appear on the yield surface of magnesium. Recall that only 229 modes were considered for the yield surface analysis; it is possible that changing which modes are considered can affect which modes are predicted to lie on the yield surface (and indeed, when we changed from the 229 modes to the 20 modes inside $\gamma^{\text{tw}} \leq 300$ mJ/m^2 and $s \leq 2$, we saw a change in some of the twin modes that were predicted to lie on the yield surface, although, comfortingly, the tension and compression twins were still predicted to be relevant). As such, the strongest conclusion we can draw at this point in time is that there are multiple modes which lie on the yield surface, but their identities are, as of yet, not fully confirmed.

Connections to Experiments

While we have completed our investigation of twins in magnesium from an experimental point of view, it is still nice to validate the conclusions against some experimental work. To this end, collaboration with the Ramesh group at Johns Hopkins University provided unique access to information from EBSD measurements of impact experiments conducted at various strain rates[1].

In our particular case, we choose to compare our predicted twin systems against the experimental results conducted at a strain rate of approximately $\dot{\varepsilon} = 10^3$ s^{-1} because their results predict five different twin variants, which gives us much more flexibility to compare to our systems. To do so, we examine EBSD data, which is reproduced with permission in Figure 7.5.

Furthermore, Figure 7.5 reveals that we have a total of seven different interfaces between regions of interest: M-T1, M-T2, M-T3, M-T4, M-T5, T2-T4, and T4-T5. Consequently, there are seven different rotation matrices between regions that we

[1] A summary of the EBSD technique is provided in Section 1.4.

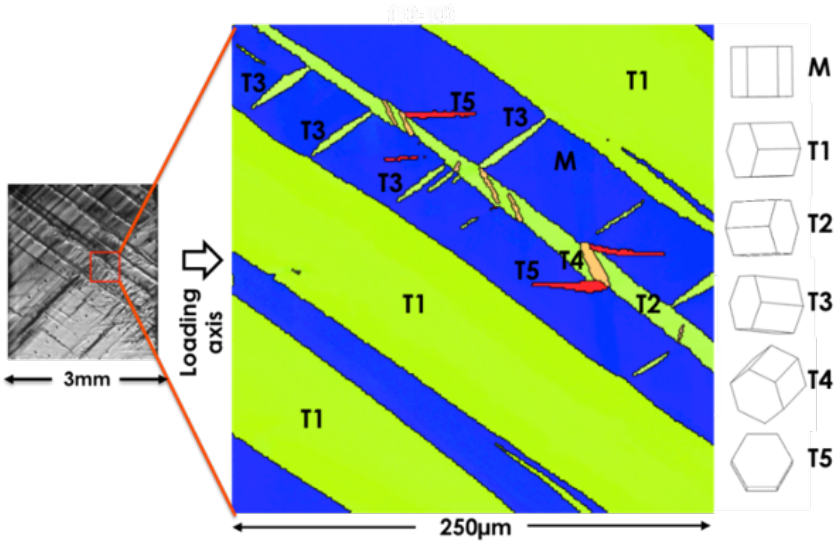

Figure 7.5: EBSD image from sample of magnesium subjected to impact at strain rate of $\dot{\varepsilon} = 10^3\ \mathrm{s}^{-1}$. Image reproduced with permission of Hazeli and Ramesh.

need to compare to our framework. Having acquired the matrix region and each of the twinned regions, we then compute the rotation matrices of the seven different interfaces.

In comparing rotation matrices, we allow for a rotation angle tolerance of 5°. Although this is fairly large, recent discussions have revealed that EBSD measurements for magnesium are slightly more inaccurate than they are for other materials. Consequently, we compare the matching rotation matrix (or, in the case of multiple matching rotation matrices within tolerance, the one with the lowest γ^{tw}). We then highlight these systems in the plot of γ^{tw} against the shear magnitude in Figure 7.6.

We see that the points here are also very diverse, but show a similar picture to what we predicted from our framework that the picture for twinning is considerably more complicated than previously acknowledged. The M-T1 interface represents a twin plane with the $(10\bar{1}1)$ normal, albeit with a higher twin interface energy and is, thus, not the traditional compression twin that is recognized across the community. On the other hand, the M-T3 interface represents the traditional $(10\bar{1}2)$ tension twin system. M-T4, on the other hand, represents a $(11\bar{2}1)$ twin plane, and the remainder of the interface are representative of irrational planes. This last point is particularly interesting; it suggests that there is the possibility that orientations being observed already could potentially be irrational twins. Going forward, we will need to pay particular attention to modes which are nearly rational but are actually computed to be irrational from our framework.

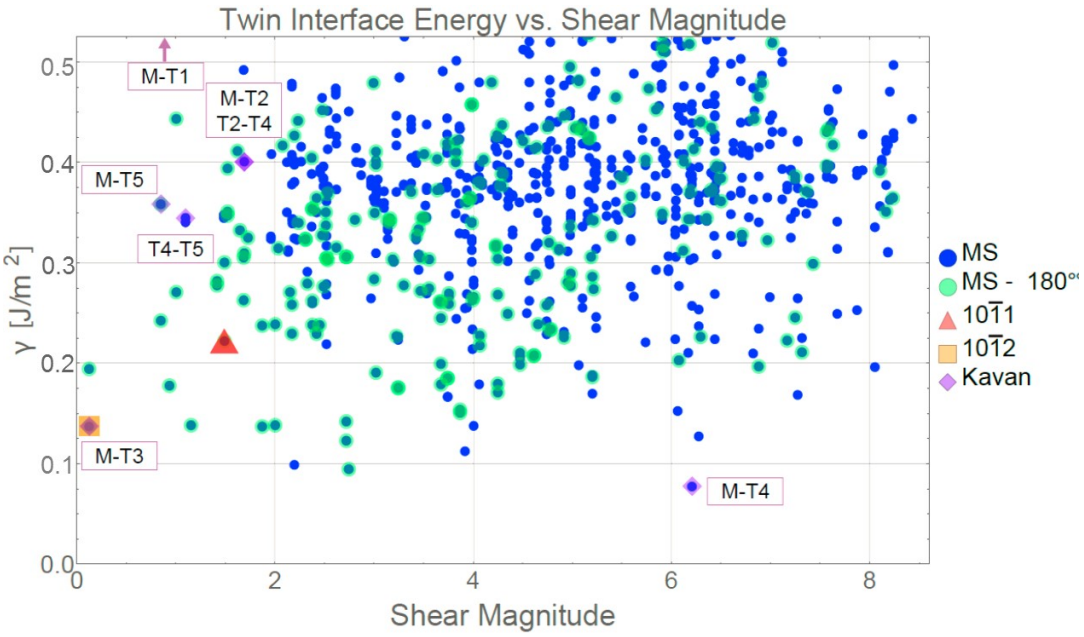

Figure 7.6: Reiterated plot of γ^{tw} vs. shear magnitude, with systems matched against the EBSD data now denoted with purple. The label by these points names the interface whose rotation was identified.

In comparing our results of Table 7.1 to other, prior observations, we see that we attain several modes which are irrational, but have planar indices that are acceptably close to those that have been previously observed in literature. However, there are some discrepancies in the shears that will require additional attention for resolution going forth. Of particular interest are the irrational twin modes that we computed to be relevant to the magnesium yield surface; these modes display faceting which is very similar to what was observed in Liu *et al.* [66], where TEM images revealed that the non-crystallographic twin planes actually displayed step-like behavior, with an overall, average direction that proved to be irrational. In that particular work, the non-crystallographic planes also displayed a step-like nature, which we also observed in some of our irrational systems, as shown in Figure 5.2; this gives us an extra measure of confidence in the results we obtained. The exact geometry along the interface of these irrational systems may prove to be an interesting area for future investigation.

7.4 Summary

We began the chapter with 229 viable twin modes; following our stress analysis, we concluded that a subset of them (although still greater than the two that have been accepted until now) actually participate on the yield surface of magnesium. These points were shown to not necessarily have the lowest γ^{tw} or necessarily have the lowest

shear magnitudes. We also compared our data to EBSD imaging and suspected that some of the more unusual twins we predicted could, in fact, be present in magnesium. Undoubtedly, there will be much room for further research into this area in the coming years.

Chapter 8

CONCLUSIONS AND FUTURE WORK

Having completed the discussion of new content for this thesis, we will now summarize the results and then discuss directions that we plan on pursuing in post-graduate research.

8.1 Conclusions of this Investigation

In our quest to better understand the mechanisms by which magnesium can accommodate deformation and be better designed as the basis for a new generation of lightweight, strong alloys, we sought to develop a more comprehensive understanding of how magnesium undergoes twinning. Though classical formulations of twinning said that only two-fold rotations could form these twins, we took an alternative approach and looked at twins from the point of view that they could also equivalently be regarded as if there was a simple shear being applied to the lattice on one side of a planar discontinuity. From here, we constructed a novel, systematic framework for predicting twinning in materials, focusing primarily on magnesium.

We started off with the kinematic framework for twinning, in which we inserted lattice vectors describing magnesium and then found a very large set of potential twins, many of which would not have been predicted from just classical approaches to twinning. However, we quickly came to the realization that the kinematic framework alone would not tell the whole picture, since a change in the lattice vectors from just the skeletal lattice to the multilattice affected the predicted twinning shear magnitude. Consequently, we realized that the shear magnitude could not act as the sole metric for predicting the likeliness to visualize any particular twin mode.

In response to the variance in the shear magnitudes predicted in the kinematic framework, we worked to understand the energetics of all of these twin modes under the rationale that twin interface energies similar to those of modes that have been visualized and accepted within the community would make for a stronger case for the potential visualization and subsequent exploitation of those newly-predicted twin modes as well. We computed the twin interface energies using primarily molecular statics simulations, verifying for a small subset using density functional theory techniques that the energies of twin systems were competitively low. We also then

examined the energetic barriers to formation for these twins, performing a large set of nudged elastic band calculations which then showed us that many of these twin modes not only have low interface energies, but also reasonably low energetic barriers to formation.

From the nudged elastic band calculations, we then also extracted the stress states at points on the reaction coordinate path between prefect crystal magnesium and the twinned magnesium. Using this information and performing a yield stress analysis of these many systems, we were able to conclude that there were a significant number of twin modes arising from our framework which actually would participate in the governance of yield behavior in magnesium. As expected, the classical tension and compression twins were observed in the final list of twins, but there were also many new twin modes that were predicted to be relevant. Some of these new twins, though not quite matching the modes that had been reported in literature (summarized in Table 1.1), were irrational and only a few degrees off orientation-wise. Similar observations were comparisons between our results and EBSD data from collaborators were made.

The overall conclusion of this research was that the twinning picture in magnesium is only partially complete; there is now strong evidence from our computational framework that there are other modes of twinning in magnesium that have not yet been accounted for and exploited, thus matching conclusions drawn from some earlier works in literature. In our post-graduate research, we will be working to further our understanding of these new twin modes and investigate what steps are necessary in order to exploit them for the future design of lightweight, strong alloys.

8.2 Upcoming Work

Of course, with every investigation, many follow-up questions are raised. This section presents a few of the directions that we intend to pursue post graduation. Some of these are continuations of discussions already introduced in the main body of text.

Alloys and Solutes

We already began a preliminary investigation of the twin systems in materials that are alloyed with aluminum, but were only able to reach as far as the twin interface energy. An obvious extension would be to also perform nudged elastic band calculations and then subsequent stress analysis on these alloyed samples. Such an investigation would bring us closer to twinning analysis of real-world materials, since the goal of our investigation is to design alloys, not just pure magnesium. We anticipate completing this study on alloys first.

Samples Under Load

One of the areas that we only began to examine during this investigation were the effects of applying loads to the sample. Due to limitations of time and computational resources, we were only able to study up to the Arrhenius frequency for the 20 twins in the region of $\gamma \leq 300$ mJ/m^2 and $s \leq 2$. Sometime after the further development of computational resources, it would be interesting to complete the full study for all of the predicted twins, giving us insight on how everything from the interface energy to the Arrhenius frequencies to the yield surface itself would evolve as the samples were loaded. This more exhaustive investigation of twins in loaded samples would help to provide a picture of twinning that would evolve with loads, perhaps shedding even more light on why the tension twin is so dominant and/or whether or not there are twin modes in loaded samples that are not being given the amount of attention they deserve.

Twin Boundary Propagation

One of the areas of our investigation that will be improved is a better understanding the propagation of twin boundaries, which is already an ongoing task. Whereas the NEB calculations and the subsequent stress analysis provided a reasonable estimate of the relevant twin modes, a more definitive investigation would be to examine the propagation of the twin boundaries. We know what the kinematics of the twinned state are, especially the amount of shear that needs to be applied to any given system in order to generate the twins of interest; our task is now to investigate whether a configuration of a known orientation will experience propagation of its twin boundary through the remainder of the sample when the geometrically-known amount of twinning shear is applied. Boundaries whose propagation is impinged would be unlikely to be visualized while boundaries which showed consistent propagation would be confirmed as ones which would participate in yield behavior governance.

Multilattices and Generalities

One of the final directions that could use further future work is the fact that the kinematic framework is somewhat sensitive to the lattice vectors which are used to describe the material. As we saw in Chapter 3, the use of the skeletal lattice vectors would result in a higher twinning shear predicted when compared to the multilattice vectors that were selected for magnesium. In addition to changes in the twinning shear magnitudes that occur when the lattice vectors describing the material are changed, some of the twin modes predicted are actually slightly different. This is somewhat

reflected by the fact that the overall shape of the angular distribution histograms are slightly different between the skeletal lattice and multilattice descriptions.

Consequently, an area that could see further improvement is the formulation of the kinematic framework to be independent of the lattice vectors describing the material. For instance, if we take two different sets of lattice vectors to describe the same exact HCP material, we should ultimately be able to recover the exact same twin modes between both descriptions. Computationally-speaking, after an improved formulation of the kinematic framework, the only factors that should change the twin modes that are observed should be the c/a ratio of the material (in addition to the bounds of μ_i^j that we choose to index the twinning equation).

BIBLIOGRAPHY

[1] G. Design. *Ashby Plot*. 2012. URL: https://www.grantadesign.com/images/ces/Youngs-Density-2012-large.jpg.

[2] G. Design. *Ashby Plot*. 2010. URL: http://www.grantadesign.com/download/pdf/teaching_resource_books/2-Materials-Charts-2010.pdf.

[3] W. Soboyejo. *Mechanical properties of engineered materials*. Vol. 152. CRC press, 2002.

[4] C. University. *Ashby Plots*. 2002. URL: http://www-materials.eng.cam.ac.uk/mpsite/interactive_charts/hardcopy/colour/Photoshop300dpi.

[5] Y. Lü, Q. Wang, W. Ding, X. Zeng, and Y. Zhu. "Fracture behavior of AZ91 magnesium alloy". In: *Materials Letters* 44.5 (2000), pp. 265–268.

[6] Y. Lü, Q. Wang, X. Zeng, W. Ding, C. Zhai, and Y. Zhu. "Effects of rare earths on the microstructure, properties and fracture behavior of Mg–Al alloys". In: *Materials Science and Engineering: A* 278.1 (2000), pp. 66–76.

[7] R. Cahn. "Soviet work on mechanical twinning". In: *Il Nuovo Cimento (1943-1954)* 10 (1953), pp. 350–386.

[8] E. Hall. *Twinning*. 1954.

[9] M. V. Klassen-Neklyudova. *Mechanical twinning of crystals*. Springer Science & Business Media, 2012.

[10] T. Blewitt, R. Coltman, and J. Redman. "Low-Temperature Deformation of Copper Single Crystals". In: *Journal of Applied Physics* 28.6 (1957), pp. 651–660.

[11] H. Suzuki and C. Barrett. "Deformation twinning in silver-gold alloys". In: *Acta metallurgica* 6.3 (1958), pp. 156–165.

[12] P. Haasen. "Plastic deformation of nickel single crystals at low temperatures". In: *Philosophical Magazine* 3.28 (1958), pp. 384–418.

[13] G. Gray. "Deformation twinning in Al-4.8 wt% Mg". In: *Acta Metallurgica* 36.7 (1988), pp. 1745–1754.

[14] J. Christian and D. Laughlin. "Twinning in derivative structures of BCC and FCC". In: *Scripta metallurgica* 21.8 (1987), pp. 1131–1135.

[15] J. Christian and D. Laughlin. "Overview no. 67 The deformation twinning of superlattice structures derived from disordered BCC or FCC solid solutions". In: *Acta Metallurgica* 36.7 (1988), pp. 1617–1642.

[16] A. Paxton and A. Entwisle. "Deformation twinning in the intermetallic compound Cu2Sb". In: *Philosophical Magazine A* 52.4 (1985), pp. 573–579.

[17] P. Pirouz. “Deformation mode in silicon, slip or twinning?” In: *Scripta metallurgica* 21.11 (1987), pp. 1463–1468.

[18] Y. Androussi, G. Vanderschaeve, and A. Lefebvre. “Slip and twinning in high-stress-deformed GaAs and the influence of doping”. In: *Philosophical Magazine A* 59.6 (1989), pp. 1189–1204.

[19] R. Garber. “Formation of Elastic Twins during Calcite Twinning”. In: *Dokl. Akad. Nauk SSSR*. Vol. 21. 1938, pp. 233–235.

[20] R. E. Reed-Hill, J. P. Hirth, and H. C. Rogers. *Deformation twinning: proceedings*. Vol. 25. Gordon and Breach Science Publishers, 1965.

[21] P. Allan, E. Crellin, and M. Bevis. “Stress-induced twinning and phase transformations in polyethylene single crystals”. In: *Philosophical Magazine* 27.1 (1973), pp. 127–145.

[22] H. Kihô. “The crystallographic aspect of the mechanical twinning in metals”. In: *Journal of the Physical Society of Japan* 9.5 (1954), pp. 739–747.

[23] H. Kiho. “The crystallographic aspect of the mechanical twinning in Ti and α-U”. In: *Journal of the Physical Society of Japan* 13.3 (1958), pp. 269–272.

[24] M. Jaswon and D. Dove. “Twinning properties of lattice planes”. In: *Acta Crystallographica* 9.8 (1956), pp. 621–626.

[25] M. Jaswon and D. Dove. “The prediction of twinning modes in metal crystals”. In: *Acta Crystallographica* 10.1 (1957), pp. 14–18.

[26] M. Jaswon and D. Dove. “The crystallography of deformation twinning”. In: *Acta Crystallographica* 13.3 (1960), pp. 232–240.

[27] 9. S. Mahajan and D. Williams. “Deformation twinning in metals and alloys”. In: *International Metallurgical Reviews* 18.2 (1973), pp. 43–61.

[28] J. W. Christian and S. Mahajan. “Deformation twinning”. In: *Progress in materials science* 39.1-2 (1995), pp. 1–157.

[29] P. Partridge. “The crystallography and deformation modes of hexagonal close-packed metals”. In: *Metallurgical reviews* 12.1 (1967), pp. 169–194.

[30] J. Sun, P. Trimby, X. Si, X. Liao, N. Tao, and J. Wang. “Nano twins in ultrafine-grained Ti processed by dynamic plastic deformation”. In: *Scripta Materialia* 68.7 (2013), pp. 475–478.

[31] S. Vaidya and S. Mahajan. “Accommodation and formation of $\{11\bar{2}1\}$ twins in Co single crystals”. In: *Acta Metallurgica* 28.8 (1980), pp. 1123–1131.

[32] M. Yoo. “Slip, twinning, and fracture in hexagonal close-packed metals”. In: *Metallurgical Transactions A* 12.3 (1981), pp. 409–418.

[33] F. Lavrentyev, O. Salita, and Y. Kazarov. In: *Fiz Metal Metalloved* 26.1 (1968), p. 348.

[34] S. Couling, J. Pashak, and L. Sturkey. “Unique deformation and aging characteristics of certain magnesium-base alloys”. In: *American Society for Metals Transactions* 51 (1959), pp. 94–107.

[35] S. Couling and C. Roberts. “New Twinning systems in magnesium”. In: *Acta Crystallographica* 9.11 (1956), pp. 972–973.

[36] R. Reed-Hill. In: *Trans Met. Sot. Amer. Inst. Min. (Metall.) Eng*. 224.70 (1960).

[37] A. Serra, R. Pond, and D. Bacon. “Computer simulation of the structure and mobility of twinning disclocations in HCP Metals”. In: *Acta metallurgica et materialia* 39.7 (1991), pp. 1469–1480.

[38] I. Beyerlein, R. McCabe, and C. Tomé. “Effect of microstructure on the nucleation of deformation twins in polycrystalline high-purity magnesium: a multi-scale modeling study”. In: *Journal of the Mechanics and Physics of Solids* 59.5 (2011), pp. 988–1003.

[39] I. J. Beyerlein, R. McCabe, and C. Tome. “Stochastic processes of {1012} deformation twinning in hexagonal close-packed polycrystalline zirconium and magnesium”. In: *International Journal for Multiscale Computational Engineering* 9.4 (2011).

[40] D. Brown, S. Agnew, M. Bourke, T. Holden, S. Vogel, and C. Tomé. “Internal strain and texture evolution during deformation twinning in magnesium”. In: *Materials Science and Engineering: A* 399.1 (2005), pp. 1–12.

[41] H. El Kadiri, J. Kapil, A. Oppedal, L. Hector, S. R. Agnew, M. Cherkaoui, and S. Vogel. “The effect of twin-twin interactions on the nucleation and propagation of $\{10\bar{1}2\}$ twinning in magnesium”. In: *Acta Materialia* 61.10 (2013), pp. 3549–3563.

[42] L. Jiang, J. J. Jonas, A. A. Luo, A. K. Sachdev, and S. Godet. “Twinning-induced softening in polycrystalline AM30 Mg alloy at moderate temperatures”. In: *Scripta Materialia* 54.5 (2006), pp. 771–775.

[43] B. Li and E. Ma. “Atomic shuffling dominated mechanism for deformation twinning in magnesium”. In: *Physical review letters* 103.3 (2009), p. 035503.

[44] B. Li and E. Ma. “Zonal dislocations mediating $\{10\bar{1}1\}\langle 10\bar{1}\bar{2}\rangle$ twinning in magnesium”. In: *Acta Materialia* 57.6 (2009), pp. 1734–1743.

[45] B. Li and X. Zhang. “Global strain generated by shuffling-dominated $\{10\bar{1}2\}\langle 10\bar{1}\bar{1}\rangle$ twinning”. In: *Scripta Materialia* 71 (2014), pp. 45–48.

[46] J. R. Morris, Y. Ye, and M. H. Yoo. “First-principles examination of the twin boundary in hcp metals”. In: *Philosophical Magazine* 85.2-3 (2005), pp. 233–238.

[47] C. Barrett, H. El Kadiri, and M. Tschopp. "Breakdown of the Schmid law in homogeneous and heterogeneous nucleation events of slip and twinning in magnesium". In: *Journal of the Mechanics and Physics of Solids* 60.12 (2012), pp. 2084–2099.

[48] H. El Kadiri, C. D. Barrett, and M. A. Tschopp. "The candidacy of shuffle and shear during compound twinning in hexagonal close-packed structures". In: *Acta Materialia* 61.20 (2013), pp. 7646–7659.

[49] Y. Wang, L.-Q. Chen, Z.-K. Liu, and S. Mathaudhu. "First-principles calculations of twin-boundary and stacking-fault energies in magnesium". In: *Scripta Materialia* 62.9 (2010), pp. 646–649.

[50] C. Xie, Q. Fang, X. Liu, P. Guo, J. Chen, M. Zhang, Y. Liu, B. Rolfe, and L. Li. "Theoretical study on the $\{\bar{1}012\}$ deformation twinning and cracking in coarse-grained magnesium alloys". In: *International Journal of Plasticity* 82 (2016), pp. 44–61.

[51] M. Yoo, J. Morris, K. Ho, and S. Agnew. "Nonbasal deformation modes of HCP metals and alloys: role of dislocation source and mobility". In: *Metallurgical and Materials Transactions A* 33.3 (2002), pp. 813–822.

[52] Q. Yu, J. Zhang, and Y. Jiang. "Direct observation of twinning–detwinning–retwinning on magnesium single crystal subjected to strain-controlled cyclic tension–compression in [0 0 0 1] direction". In: *Philosophical magazine letters* 91.12 (2011), pp. 757–765.

[53] Q. Yu, L. Qi, K. Chen, R. K. Mishra, J. Li, and A. M. Minor. "The nanostructured origin of deformation twinning". In: *Nano letters* 12.2 (2012), pp. 887–892.

[54] N. E. Paton and W. Backofen. "Plastic deformation of titanium at elevated temperatures". In: *Metallurgical and Materials Transactions B* 1.10 (1970), pp. 2839–2847.

[55] R. Reed-Hill and W. Robertson. "The crystallographic characteristics of fracture in magnesium single crystals". In: *Acta Metallurgica* 5.12 (1957), pp. 728–737.

[56] R. Reed-Hill and W. Robertson. "Additional modes of deformation twinning in magnesium". In: *Acta Metallurgica* 5.12 (1957), pp. 717–727.

[57] J. Wang, I. Beyerlein, J. Hirth, and C. Tomé. "Twinning dislocations on $\{\bar{1}011\}$ and $\{\bar{1}013\}$ planes in hexagonal close-packed crystals". In: *Acta Materialia* 59.10 (2011), pp. 3990–4001.

[58] J. Wang, I. Beyerlein, and J. Hirth. "Nucleation of elementary and twinning dislocations at a twin boundary in hexagonal close-packed crystals". In: *Modelling and Simulation in Materials Science and Engineering* 20.2 (2012), p. 024001.

[59] J. Smith and P. Gaunt. “The martensitic transformations in gold-manganese alloys near the equiatomic composition”. In: *Acta Metallurgica* 9.9 (1961), pp. 819–824.

[60] L. Odinokova. “The Role of Twinning During Plastic Deformation of Titanium”. In: *Russian Metallurgy* 1.1 (1967), pp. 61–64.

[61] R. Reed-Hill and E. Dahlberg. “SOME EFFECTS OF PRESTRAIN AT 77 DEG K ON THE MECHANICAL PROPERTIES OF ZIRCONIUM AT ROOM TEMPERATURE”. In: *Electrochemical Technology (US) Absorbed by J. Electrochem. Soc.* 4 (1966).

[62] R. Reed-Hill, W. Slippy Jr, and L. Buteau. “DETERMINATION OF ALPHA ZIRCONIUM 1121 TWINNING ELEMENTS USING GRAIN BOUNDARY ROTATIONS”. In: *Trans. AIME* 227 (1963).

[63] I. N. Sokurskii and L. Protsenko. “Deformation systems of α-zirconium”. In: *Atomic Energy* 4.5 (1958), pp. 579–582.

[64] D. Westlake. “Twinning in zirconium”. In: *Acta Metallurgica* 9.4 (1961), pp. 327–331.

[65] T. Kitahara, S. Ando, M. Tsushida, H. Kitahara, and H. Tonda. “Deformation behavior of magnesium single crystals in c-axis compression”. In: *Key Engineering Materials*. Vol. 345. Trans Tech Publ. 2007, pp. 129–132.

[66] B.-Y. Liu, J. Wang, B. Li, L. Lu, X.-Y. Zhang, Z.-W. Shan, J. Li, C.-L. Jia, J. Sun, and E. Ma. “Twinning-like lattice reorientation without a crystallographic twinning plane”. In: *Nature communications* 5 (2014).

[67] A. J. Schwartz, M. Kumar, B. L. Adams, and D. P. Field. *Electron backscatter diffraction in materials science*. Vol. 2. Springer, 2009.

[68] J. C. Spence. *Experimental high-resolution electron microscopy*. Oxford University Press, 1988.

[69] B. Fultz and J. M. Howe. *Transmission electron microscopy and diffractometry of materials*. Springer Science & Business Media, 2012.

[70] B. Bilby and A. Crocker. “The theory of the crystallography of deformation twinning”. In: *Proceedings of the Royal Society of London A: Mathematical, Physical and Engineering Sciences*. Vol. 288. 1413. The Royal Society. 1965, pp. 240–255.

[71] M. Bevis and A. Crocker. “Twinning shears in lattices”. In: *Proceedings of the Royal Society of London A: Mathematical, Physical and Engineering Sciences*. Vol. 304. 1476. The Royal Society. 1968, pp. 123–134.

[72] M. Bevis and A. Crocker. “Twinning modes in lattices”. In: *Proceedings of the Royal Society of London A: Mathematical, Physical and Engineering Sciences*. Vol. 313. 1515. The Royal Society. 1969, pp. 509–529.

[73] G. Friedel. *Leçons de cristallographie*. A. Blanchard, 1964.

[74] A. t. Santoro and A. Mighell. "Coincidence-site lattices". In: *Acta Crystallographica Section A: Crystal Physics, Diffraction, Theoretical and General Crystallography* 29.2 (1973), pp. 169–175.

[75] A. Santoro. "Characterization of twinning". In: *Acta Crystallographica Section A: Crystal Physics, Diffraction, Theoretical and General Crystallography* 30.2 (1974), pp. 224–231.

[76] J. Ericksen. "Nonlinear elasticity of diatomic crystals". In: *International Journal of Solids and Structures* 6.7 (1970), pp. 951–957.

[77] J. Ericksen. "Special topics in elastostatics". In: *Advances in applied mechanics* 17 (1977), pp. 189–244.

[78] J. Ericksen. "On the symmetry of deformable crystals". In: *Archive for Rational Mechanics and Analysis* 72.1 (1979), pp. 1–13.

[79] J. Ericksen. "Some phase transitions in crystals". In: *Archive for Rational Mechanics and Analysis* 73.2 (1980), pp. 99–124.

[80] J. Ericksen. "Continuous martensitic transitions in thermoelastic solids". In: *Journal of Thermal Stresses* 4.2 (1981), pp. 107–119.

[81] J. Ericksen. "Crystal lattices and sub-lattices". In: *Rendiconti del Seminario Matematico della Università di Padova* 68 (1982), pp. 1–9.

[82] R. D. James. "Finite deformation by mechanical twinning". In: *Archive for Rational Mechanics and Analysis* 77.2 (1981), pp. 143–176.

[83] M. Pitteri. "On the kinematics of mechanical twinning in crystals". In: *The Breadth and Depth of Continuum Mechanics*. Springer, 1986, pp. 671–703.

[84] M. Pitteri. "On type-2 twins in crystals". In: *International Journal of Plasticity* 2.2 (1986), pp. 99–106.

[85] J. M. Ball and R. D. James. "Fine phase mixtures as minimizers of energy". In: *Archive for Rational Mechanics and Analysis* 100.1 (1987), pp. 13–52.

[86] J. M. Ball and R. D. James. "Proposed experimental tests of a theory of fine microstructure and the two-well problem". In: *Philosophical Transactions of the Royal Society of London A: Mathematical, Physical and Engineering Sciences* 338.1650 (1992), pp. 389–450.

[87] G. Zanzotto. *Twinning in minerals and metals: remarks on the comparison of a thermoelastic theory with some experimental results. Generalities and mechanical twinning*. Accademia Nazionale Dei Lincei. 1988.

[88] G. Zanzotto. *Twinning in minerals and metals: remarks on the comparison of a thermoelastic theory with some experimental results. Mechanical twinning and growth twinning*. Accademia Nazionale Dei Lincei. 1988.

[89] G. Zanzotto. “The Cauchy–Born hypothesis, nonlinear elasticity and mechanical twinning in crystals”. In: *Acta Crystallographica Section A: Foundations of Crystallography* 52.6 (1996), pp. 839–849.

[90] J. Ericksen. “Notes on the X-ray Theory”. In: *Journal of Elasticity* 55 (1999), pp. 201–218.

[91] J. Ericksen. “On correlating two theories of twinning”. In: *Archive for rational mechanics and analysis* 153.4 (2000), pp. 261–289.

[92] J. Ericksen. “Twinning analyses in the X-ray theory”. In: *International Journal of Solids and Structures* 38 (2001), pp. 967–995.

[93] J. Ericksen. “On The X-Ray Theory of Twinning”. In: *Mathematics and Mechanics of Solids* 7 (2002), pp. 331–352.

[94] R. L. Fleischer. “Rapid solution hardening, dislocation mobility, and the flow stress of crystals”. In: *Journal of Applied Physics* 33.12 (1962), pp. 3504–3508.

[95] W. Johnston and J. J. Gilman. “Dislocation velocities, dislocation densities, and plastic flow in lithium fluoride crystals”. In: *Journal of Applied Physics* 30.2 (1959), pp. 129–144.

[96] N. Mott and F. Nabarro. “Report on strength of solids”. In: *Physical Society, London* (1948), pp. 1–19.

[97] A. Cochardt, G. Schoek, and H. Wiedersich. “Interaction between dislocations and interstitial atoms in body-centered cubic metals”. In: *Acta metallurgica* 3.6 (1955), pp. 533–537.

[98] R. Fleischer. “Substitutional solution hardening”. In: *Acta metallurgica* 11.3 (1963), pp. 203–209.

[99] A. Love. *Treatise on the Mathematical Theory of Elasticity*. 1944.

[100] S. Timoshenko, S. Timoshenko, and J. Goodier. *Theory of Elasticity, by S. Timoshenko and JN Goodier,...* McGraw-Hill book Company, 1951.

[101] F. R. Nabarro. “Report of a Conference on the Strength of Solids”. In: *The Physical Society, London* 75 (1948).

[102] A. Cottrell. “Report of a Conference on Strength of Solids”. In: *Physical Society, London* 30 (1948).

[103] R. Fleischer. “The flow stress of body-centered cubic metals: inherent lattice hardening or solution hardening?” In: *Acta Metallurgica* 15.9 (1967), pp. 1513–1519.

[104] R. Peierls. “The size of a dislocation”. In: *Proceedings of the Physical Society* 52.1 (1940), p. 34.

[105] J. E. Dorn and S. Rajnak. “Nucleation of kink pairs and the Peierls mechanism of plastic deformation”. In: *Trans. Aime* 230.8 (1964), pp. 1052–1064.

[106] J. B. Clark. “Age hardening in a Mg-9 wt.% Al alloy”. In: *Acta Metallurgica* 16.2 (1968), pp. 141–152.

[107] G. Nussbaum, P. Sainfort, G. Regazzoni, and H. Gjestland. “Strengthening mechanisms in the rapidly solidified AZ 91 magnesium alloy”. In: *Scripta Metallurgica* 23.7 (1989), pp. 1079–1084.

[108] T. Rzycho and A. Kiebus. “Effect of rare earth elements on the microstructure of Mg-Al alloys”. In: *Journal of Achievements in Materials and Manufacturing Engineering* 17.1-2 (2006), pp. 149–152.

[109] C.-W. Yang. “Tensile Mechanical Properties and Fracture Behaviors of Friction Stir Processing (FSP) Modified Mg-Al-Zn and Dual-Phase Mg-Li-Al-Zn Alloys”. In: *Materials Science - Advanced Topics* (2013).

[110] T. Mukai, M. Yamanoi, H. Watanabe, and K. Higashi. “Ductility enhancement in AZ31 magnesium alloy by controlling its grain structure”. In: *Scripta Materialia* 45.1 (2001), pp. 89–94.

[111] A. Yamashita, Z. Horita, and T. G. Langdon. “Improving the mechanical properties of magnesium and a magnesium alloy through severe plastic deformation”. In: *Materials Science and Engineering: A* 300.1 (2001), pp. 142–147.

[112] S. Agnew, J. Horton, T. Lillo, and D. Brown. “Enhanced ductility in strongly textured magnesium produced by equal channel angular processing”. In: *Scripta Materialia* 50.3 (2004), pp. 377–381.

[113] K. Xia, J. Wang, X. Wu, G. Chen, and M. Gurvan. “Equal channel angular pressing of magnesium alloy AZ31”. In: *Materials Science and Engineering: A* 410 (2005), pp. 324–327.

[114] G. P. M. Leyson, W. A. Curtin, L. G. Hector Jr, and C. F. Woodward. “Quantitative prediction of solute strengthening in aluminium alloys”. In: *Nature materials* 9.9 (2010), pp. 750–755.

[115] S. Shang, W. Wang, B. Zhou, Y. Wang, K. Darling, L. Kecskes, S. Mathaudhu, and Z. Liu. “Generalized stacking fault energy, ideal strength and twinnability of dilute Mg-based alloys: a first-principles study of shear deformation”. In: *Acta Materialia* 67 (2014), pp. 168–180.

[116] A. Fitzner, D. L. Prakash, J. Q. da Fonseca, M. Thomas, S.-Y. Zhang, J. Kelleher, P. Manuel, and M. Preuss. “The effect of aluminium on twinning in binary alpha-titanium”. In: *Acta Materialia* 103 (2016), pp. 341–351.

[117] K. Bhattacharya. *Microstructure of martensite: why it forms and how it gives rise to the shape-memory effect*. Vol. 2. Oxford University Press, 2003.

[118] J. Hirth and J. Lothe. “Theory of Dislocations, 2nd”. In: *Ed.: John Willey & Sons* (1982).

[119] D. Hull and D. J. Bacon. *Introduction to dislocations*. Butterworth-Heinemann, 2001.

[120] E. Fermi, J. Pasta, and S. Ulam. "Studies of nonlinear problems". In: *Los Alamos Report LA-1940* 978 (1955).

[121] B. J. Alder and T. E. Wainwright. "Studies in molecular dynamics. I. General method". In: *The Journal of Chemical Physics* 31.2 (1959), pp. 459–466.

[122] J. Gibson, A. N. Goland, M. Milgram, and G. Vineyard. "Dynamics of radiation damage". In: *Physical Review* 120.4 (1960), p. 1229.

[123] A. Rahman. "Correlations in the motion of atoms in liquid argon". In: *Physical Review* 136.2A (1964), A405.

[124] B. Leimkuhler and C. Matthews. "Numerical Methods for Stochastic Molecular Dynamics". In: *Molecular Dynamics*. Springer, 2015, pp. 261–328.

[125] D. Sun, M. Mendelev, C. Becker, K. Kudin, T. Haxhimali, M. Asta, J. Hoyt, A. Karma, and D. Srolovitz. "Crystal-melt interfacial free energies in hcp metals: A molecular dynamics study of Mg". In: *Physical Review B* 73.2 (2006), p. 024116.

[126] M. Baskes. "Modified embedded-atom potentials for cubic materials and impurities". In: *Physical Review B* 46.5 (1992), p. 2727.

[127] M. S. Daw and M. I. Baskes. "Embedded-atom method: Derivation and application to impurities, surfaces, and other defects in metals". In: *Physical Review B* 29.12 (1984), p. 6443.

[128] G. Henkelman and H. Jónsson. "Improved tangent estimate in the nudged elastic band method for finding minimum energy paths and saddle points". In: *The Journal of chemical physics* 113.22 (2000), pp. 9978–9985.

[129] G. Henkelman, B. P. Uberuaga, and H. Jónsson. "A climbing image nudged elastic band method for finding saddle points and minimum energy paths". In: *The Journal of chemical physics* 113.22 (2000), pp. 9901–9904.

[130] A. Nakano. "A space–time-ensemble parallel nudged elastic band algorithm for molecular kinetics simulation". In: *Computer Physics Communications* 178.4 (2008), pp. 280–289.

[131] J. H. Weiner. *Statistical mechanics of elasticity*. Courier Corporation, 2002.

[132] S. Plimpton. "Fast parallel algorithms for short-range molecular dynamics". In: *Journal of computational physics* 117.1 (1995), pp. 1–19.

[133] L. H. Thomas. "The calculation of atomic fields". In: *Mathematical Proceedings of the Cambridge Philosophical Society*. Vol. 23. 05. Cambridge Univ Press. 1927, pp. 542–548.

[134] E. Fermi. "Un metodo statistico per la determinazione di alcune priorieta dellatome". In: *Rend. Accad. Naz. Lincei* 6.602-607 (1927), p. 32.

[135] P. Hohenberg and W. Kohn. “Inhomogeneous electron gas”. In: *Physical review* 136.3B (1964), B864.

[136] R. G. Parr and Y. Weitao. *Density-functional theory of atoms and molecules*. Vol. 16. Oxford university press, 1994.

[137] W. Kohn and L. J. Sham. “Self-consistent equations including exchange and correlation effects”. In: *Physical review* 140.4A (1965), A1133.

[138] P. Suryanarayana, K. Bhattacharya, and M. Ortiz. “Coarse-graining Kohn–Sham density functional theory”. In: *Journal of the Mechanics and Physics of Solids* 61.1 (2013), pp. 38–60.

[139] M. Ponga, K. Bhattacharya, and M. Ortiz. “A sublinear-scaling approach to density-functional-theory analysis of crystal defects”. In: *Journal of the Mechanics and Physics of Solids* 95 (2016), pp. 530–556.

[140] X.-C. Wang, T. Blesgen, K. Bhattacharya, and M. Ortiz. “A variational framework for spectral approximations of Kohn–Sham Density Functional Theory”. In: *Archive for Rational Mechanics and Analysis* 221.2 (2016), pp. 1035–1075.

[141] M. Gillan. “Calculation of the vacancy formation energy in aluminium”. In: *Journal of Physics: Condensed Matter* 1.4 (1989), p. 689.

[142] G. H. Golub and G. Meurant. *Matrices, moments and quadrature with applications*. Princeton University Press, 2009.

[143] Y.-M. Kim, N. J. Kim, and B.-J. Lee. “Atomistic modeling of pure Mg and Mg–Al systems”. In: *Calphad* 33.4 (2009), pp. 650–657.

[144] Z. Wu, M. Francis, and W. Curtin. “Magnesium interatomic potential for simulating plasticity and fracture phenomena”. In: *Modelling and Simulation in Materials Science and Engineering* 23.1 (2015), p. 015004.

[145] D. Guyoncourt and A. Crocker. “The deformation twinning mode of crystalline Mercury”. In: *Acta Metallurgica* 16.4 (1968), pp. 523–534.

[146] D. Levine and P. J. Steinhardt. “Quasicrystals. I. Definition and structure”. In: *Physical Review B* 34.2 (1986), p. 596.

[147] A. Sutton and V. Vitek. “On the structure of tilt grain boundaries in cubic metals I. Symmetrical tilt boundaries”. In: *Philosophical Transactions of the Royal Society of London A: Mathematical, Physical and Engineering Sciences* 309.1506 (1983), pp. 1–36.

[148] G. Olson and M. Cohen. “Interphase-boundary dislocations and the concept of coherency”. In: *Acta Metallurgica* 27.12 (1979), pp. 1907–1918.

[149] G. Olson. “Fine structure of interphase boundaries”. In: *Acta Metallurgica* 29.8 (1981), pp. 1475–1484.

[150] J. Cahn, G. Kalonji, H. Aaronson, D. Laughlin, R. Sekerka, and C. Wayman. “Solid-solid phase transformations”. In: *New York* (1982), p. 3.

[151] A. Stukowski. “Visualization and analysis of atomistic simulation data with OVITO–the Open Visualization Tool”. In: *Modelling and Simulation in Materials Science and Engineering* 18.1 (2009), p. 015012.

[152] M. Mendelev, S. Han, D. Srolovitz, G. Ackland, D. Sun, and M. Asta. “Development of new interatomic potentials appropriate for crystalline and liquid iron”. In: *Philosophical magazine* 83.35 (2003), pp. 3977–3994.

[153] P. Williams, Y. Mishin, and J. Hamilton. “An embedded-atom potential for the Cu–Ag system”. In: *Modelling and Simulation in Materials Science and Engineering* 14.5 (2006), p. 817.

[154] M. Mendelev, M. Kramer, C. Becker, and M. Asta. “Analysis of semi-empirical interatomic potentials appropriate for simulation of crystalline and liquid Al and Cu”. In: *Philosophical Magazine* 88.12 (2008), pp. 1723–1750.

[155] R. Ravelo, T. Germann, O. Guerrero, Q. An, and B. Holian. “Shock-induced plasticity in tantalum single crystals: Interatomic potentials and large-scale molecular-dynamics simulations”. In: *Physical Review B* 88.13 (2013), p. 134101.

[156] R. R. Zope and Y. Mishin. “Interatomic potentials for atomistic simulations of the Ti-Al system”. In: *Physical Review B* 68.2 (2003), p. 024102.

[157] B. Jelinek, S. Groh, M. F. Horstemeyer, J. Houze, S.-G. Kim, G. J. Wagner, A. Moitra, and M. I. Baskes. “Modified embedded atom method potential for Al, Si, Mg, Cu, and Fe alloys”. In: *Physical Review B* 85.24 (2012), p. 245102.

[158] M. Mendelev, M. Asta, M. Rahman, and J. Hoyt. “Development of interatomic potentials appropriate for simulation of solid–liquid interface properties in Al–Mg alloys”. In: *Philosophical Magazine* 89.34-36 (2009), pp. 3269–3285.

[159] H. Conrad and W. Robertson. “Creep characteristics of magnesium single crystals from 78ř to 364ř K”. In: *Trans. Met. Soc. AIME* 212 (1958).

[160] A. Staroselsky and L. Anand. “A constitutive model for hcp materials deforming by slip and twinning: application to magnesium alloy AZ31B”. In: *International journal of Plasticity* 19.10 (2003), pp. 1843–1864.

[161] M. Pitteri and G. Zanzotto. *Continuum models for phase transitions and twinning in crystals*. CRC Press, 2002.

Appendix A

SUPPLEMENTAL MATERIAL

We now present supplementary calculations which will enhance the development of some of the concepts which were used in the remainder of this work.

A.1 Additional Background: Twin Kinematics

In this section, we will present some supplementary details for those of you who are interested in reading further on the matter.

Crystallographic Indices of Directions and Planes for HCP Materials

Let us consider a set of basis vectors $\boldsymbol{e}_1, \boldsymbol{e}_2$, and $\boldsymbol{e}_3$. A direction $\boldsymbol{d}$ can be written in terms of these basis vectors by using the set of indices $\{I_1, I_2, I_3\}$ as

$$\boldsymbol{d} = I_1\boldsymbol{e}_1 + I_2\boldsymbol{e}_2 + I_3\boldsymbol{e}_3. \tag{A.1}$$

Typically, for HCP materials, a four-index system is used; supposing that these new indices are described by $\{i_1, i_2, i_R, i_3\}$, then we can write out the direction equivalently as

$$\boldsymbol{d} = i_1\boldsymbol{e}_1 + i_2\boldsymbol{e}_3 + i_R\boldsymbol{e}_R + i_3\boldsymbol{e}_3, \tag{A.2}$$

where $\boldsymbol{e}_R$ is a redundant vector, since, for HCP materials,

$$\boldsymbol{e}_3 = -(\boldsymbol{e}_1 + \boldsymbol{e}_2). \tag{A.3}$$

Consequently, a common feature of the four-index formulation of directions is that

$$i_1 + i_2 + i_3 = 0. \tag{A.4}$$

Note that both the three- and four-index formulations of directions should yield the exact same direction vector at the end of the day. Thus, we may convert

$$\begin{cases} I_1 = i_1 - i_R \\ I_2 = i_2 - i_R \\ I_3 = i_3 \end{cases} \Leftrightarrow \begin{cases} i_1 = \dfrac{1}{3}(2I_1 - I_2) \\ i_2 = \dfrac{1}{3}(2I_2 - I_1) \\ i_R = -(i_1 + i_2) \\ i_3 = I_3 \end{cases}. \tag{A.5}$$

When reducing for the indices in directions, one should take note of and account for the reciprocal basis vector according to Equation (A.2).

Let us now turn our attention over towards planes. Let us assume that we have a vector $\boldsymbol{n}$ which lies normal to a plane of interest. For some set of indices $[n_1, n_2, n_3]$, the vector normal to the plane can then be described using the reciprocal lattice vectors,

$$\boldsymbol{n} = n_1\boldsymbol{e}^1 + n_2\boldsymbol{e}^2 + n_3\boldsymbol{e}^3, \tag{A.6}$$

where $\boldsymbol{e}^1, \boldsymbol{e}^2$, and $\boldsymbol{e}^3$ are the reciprocal lattice vectors, which can be computed using Equation (2.4). This is significantly more convenient and formulaic than the traditional approach of attempting to find axis intercepts, and our formulation of the planar normals will adopt this approach.

Twinning as Simple Shear

One of the fundamental tenements of the kinematic framework was that the lattice description of the twinned material, $\boldsymbol{g}_i$, could be related to the reference material, with lattice vectors $\boldsymbol{e}_i$, through a simple shear, as presented in Equation (2.11), with $\boldsymbol{s} \cdot \hat{\boldsymbol{n}} = 0$.

The normal of the twin boundary, which is denoted by $\hat{\boldsymbol{n}}$, can be written in terms of the lattice vectors on both sides of it,

$$\hat{\boldsymbol{n}} = \nu_i \boldsymbol{e}^i = \nu_i \boldsymbol{g}^i, \tag{A.7}$$

which takes advantage of the fact that, since the same plane is being examined, it is permissible to maintain the same indices in describing the plane whilst changing the lattice vectors being used. We may then take the inner product of $\hat{\boldsymbol{n}}$ with $\boldsymbol{e}_i$ in order to get that

$$\hat{\boldsymbol{n}} \cdot \boldsymbol{e}_i = \nu_i \boldsymbol{e}^i \cdot \boldsymbol{e}_i = \nu_i.$$

In a similar vein,

$$\hat{\boldsymbol{n}} \cdot \boldsymbol{g}_i = \nu_i \boldsymbol{g}^i \cdot \boldsymbol{g}_i = \nu_i,$$

illustrating the validity of maintaining the indices.

With that said, let us now focus on manipulating $\boldsymbol{g}_i$ by adding and subtracting by a particular value, i.e.

$$\boldsymbol{g}_i = \boldsymbol{g}_i - \nu_i\hat{\boldsymbol{n}} + \nu_i\hat{\boldsymbol{n}} = \boldsymbol{g}_i - (\boldsymbol{g}_i \cdot \hat{\boldsymbol{n}})\hat{\boldsymbol{n}} + (\boldsymbol{g}_i \cdot \hat{\boldsymbol{n}})\hat{\boldsymbol{n}}.$$

Let us now define some α_i^j by

$$\alpha_i^j = (\boldsymbol{g}_i - \nu_i\hat{\boldsymbol{n}}) \cdot \boldsymbol{g}^j = (\delta_i^j - \nu_i(\boldsymbol{n} \cdot \boldsymbol{g}^j)),$$

where we have exploited the property between covariant and contravariant vectors, $\boldsymbol{e}_i \cdot \boldsymbol{e}^j = \delta_i^j$. Note that α_i^j has been defined so that

$$\begin{aligned}\alpha_i^j \boldsymbol{g}_j &= (\delta_i^j - \nu_i(\hat{\boldsymbol{n}} \cdot \boldsymbol{g}^j))\boldsymbol{g}_j \\ &= \boldsymbol{g}_i - \nu_i(\hat{\boldsymbol{n}} \cdot \boldsymbol{g}^j)\boldsymbol{g}_j \\ &= \boldsymbol{g}_i - \nu_i \hat{\boldsymbol{n}}.\end{aligned}$$

Reorganizing, we can see that

$$\boldsymbol{g}_i = \alpha_i^j \boldsymbol{g}_j - \nu_i \hat{\boldsymbol{n}}.$$

We now want to try and manipulate $\alpha_i^j \boldsymbol{g}_j$ so that we may replace the $\boldsymbol{g}_j$ with some $\boldsymbol{e}_j$ to relate back to the reference lattice. To do this, we must show that $\alpha_i^j \boldsymbol{g}_j = \alpha_i^j \boldsymbol{e}_j$. Fortunately, this actually turns out to be nothing more than an expansion for α_i^j and a substitution for $\hat{\boldsymbol{n}}$ as follows:

$$\begin{aligned}\alpha_i^j \boldsymbol{g}_j &\stackrel{?}{=} \alpha_i^j \boldsymbol{e}_j \\ (\delta_i^j - \nu_i(\hat{\boldsymbol{n}} \cdot \boldsymbol{g}^j))\boldsymbol{g}_j &= (\delta_i^j - \nu_i(\hat{\boldsymbol{n}} \cdot \boldsymbol{g}^j))\boldsymbol{e}_j \\ \boldsymbol{g}_i - \nu_i(\hat{\boldsymbol{n}} \cdot \boldsymbol{g}^j)\boldsymbol{g}_j &= \boldsymbol{e}_i - \nu_i(\boldsymbol{n} \cdot \boldsymbol{g}^j)\boldsymbol{e}_i.\end{aligned}$$

It is at this point that we invoke Equation (A.7) and find that

$$\boldsymbol{g}_i - \nu_i(\nu_k \boldsymbol{e}^k \cdot \boldsymbol{g}^j)\boldsymbol{g}_j = \boldsymbol{e}_i - \nu_i(\nu_k \boldsymbol{g}^k \cdot \boldsymbol{g}^j)\boldsymbol{e}_j.$$

Having shown that we can write $\alpha_i^j \boldsymbol{g}_j = \alpha_i^j \boldsymbol{e}_j$, we then see that the twinned lattice vectors are

$$\begin{aligned}\boldsymbol{g}_i &= \alpha_i^j \boldsymbol{g}_j + \nu_i \hat{\boldsymbol{n}} = \alpha_i^j \boldsymbol{e}_j + \nu_i \hat{\boldsymbol{n}} \\ &= (\delta_i^j - \nu_i(\hat{\boldsymbol{n}} \cdot \boldsymbol{g}_j))\boldsymbol{e}_j + \nu_i \hat{\boldsymbol{n}} \\ &= \boldsymbol{e}_i - \nu_i(\hat{\boldsymbol{n}} \cdot \boldsymbol{g}^j)\boldsymbol{e}_j + \nu_i \hat{\boldsymbol{n}} \\ &= \boldsymbol{e}_i + \nu_i(-(\hat{\boldsymbol{n}} \cdot \boldsymbol{g}^j)\boldsymbol{e}_j + \hat{\boldsymbol{n}}).\end{aligned}$$

Setting the twinning shear $\boldsymbol{s} = \hat{\boldsymbol{n}} - (\hat{\boldsymbol{n}} \cdot \boldsymbol{g}^j)\boldsymbol{e}_j$ and utilizing that $\nu_i = \hat{\boldsymbol{n}} \cdot \boldsymbol{e}_i$,

$$\begin{aligned}\boldsymbol{g}_i &= \boldsymbol{e}_i + \nu_i \boldsymbol{s} \\ &= \boldsymbol{e}_i + (\hat{\boldsymbol{n}} \cdot \boldsymbol{e}_i)\boldsymbol{s} \\ &= \boldsymbol{e}_i + (\boldsymbol{s} \otimes \boldsymbol{n})\boldsymbol{e}_i \\ &= (\boldsymbol{\delta} + \boldsymbol{s} \otimes \hat{\boldsymbol{n}})\boldsymbol{e}_i,\end{aligned}$$

thus returning us to the simple shear relation.

We conclude this proof by demonstrating that the shear and the normal are perpendicular as per expectation. Expanding on our earlier definition of the twinning shear,

$$\begin{aligned} \boldsymbol{s}\cdot\hat{\boldsymbol{n}} &= (\hat{\boldsymbol{n}} - (\hat{\boldsymbol{n}}\cdot\boldsymbol{g}_j)\boldsymbol{e}_j)\cdot\hat{\boldsymbol{n}} \\ &= -(\hat{\boldsymbol{n}}\cdot\boldsymbol{g}^j)(\boldsymbol{e}_j\cdot\hat{\boldsymbol{n}}) + \hat{\boldsymbol{n}}\cdot\hat{\boldsymbol{n}} \\ &= -(\hat{\boldsymbol{n}}\cdot\boldsymbol{e}^j)(\boldsymbol{e}_j\cdot\hat{\boldsymbol{n}}) + \hat{\boldsymbol{n}}\cdot\hat{\boldsymbol{n}} \\ &= -\hat{\boldsymbol{n}}\cdot\hat{\boldsymbol{n}} + \hat{\boldsymbol{n}}\cdot\hat{\boldsymbol{n}} \\ &= 0, \end{aligned}$$

which is exactly as expected. This result is crucial, as it shows that the shearing of the atoms will never deform the sample such that atoms which were originally on the twinned side of the lattice would be deformed through the twin plane. This property of the twin deformation allows us to exploit the geometry to efficiently construct computational cells in subsequent portions of this work.

Right Cauchy-Green Tensor

The formal statement of Ball and James is that, given some $\boldsymbol{F}, \boldsymbol{G}$ with positive determinant, there exists some rotation $\boldsymbol{Q}$, vectors $\boldsymbol{s} \neq \boldsymbol{0}$ and $\|\hat{\boldsymbol{n}}\| = 1$ such that

$$\boldsymbol{QF} - \boldsymbol{G} = \boldsymbol{s}\otimes\hat{\boldsymbol{n}}$$

if, and only if, the following conditions hold:

1. The right Cauchy-Green deformation tensor for the lattice has the form $\boldsymbol{C} = \boldsymbol{G}^{-\mathrm{T}}\boldsymbol{F}^{\mathrm{T}}\boldsymbol{F}\boldsymbol{G}^{-1} \neq \boldsymbol{\delta}$.

2. The eigenvalues of $\boldsymbol{C}$ are such that $\lambda_1 \leq \lambda_2 = 1 \leq \lambda_3$.

If these conditions hold, then the normal and shear of the twin may be written according to Equations (2.16a) and (2.16b).

Consider a modification of Equation (2.11),

$$\boldsymbol{QFG}^{-1} = \boldsymbol{\delta} + \boldsymbol{s}\otimes\boldsymbol{G}^{-\mathrm{T}}\hat{\boldsymbol{n}}.$$

The consequent right Cauchy-Green tensor is then

$$\begin{aligned} \boldsymbol{C} &= (\boldsymbol{QFG}^{-1})^{\mathrm{T}}(\boldsymbol{QFG}^{-1}) \\ &= (\boldsymbol{\delta} + \boldsymbol{G}^{-\mathrm{T}}\hat{\boldsymbol{n}}\otimes\boldsymbol{s})(\boldsymbol{\delta} + \boldsymbol{s}\otimes\boldsymbol{G}^{-\mathrm{T}}\hat{\boldsymbol{n}}) \\ &= \boldsymbol{\delta} + \boldsymbol{G}^{-\mathrm{T}}\hat{\boldsymbol{n}}\otimes\boldsymbol{s} + \boldsymbol{s}\otimes\boldsymbol{G}^{-\mathrm{T}}\hat{\boldsymbol{n}} + \|\boldsymbol{s}\|^2\boldsymbol{G}^{-\mathrm{T}}\hat{\boldsymbol{n}}\otimes\boldsymbol{G}^{-\mathrm{T}}\hat{\boldsymbol{n}}. \end{aligned}$$

We can reorganize this by splitting the contribution of the $\|\boldsymbol{s}\|^2$ term into two components, thus giving us

$$\boldsymbol{C} = \boldsymbol{\delta} + \left(\boldsymbol{s} + \frac{1}{2}\|\boldsymbol{s}\|^2\boldsymbol{G}^{-\mathrm{T}}\hat{\boldsymbol{n}}\right) \otimes \boldsymbol{G}^{-\mathrm{T}}\hat{\boldsymbol{n}} + \boldsymbol{G}^{-\mathrm{T}}\hat{\boldsymbol{n}} \otimes \left(\boldsymbol{s} + \frac{1}{2}\|\boldsymbol{s}\|^2\boldsymbol{G}^{-\mathrm{T}}\hat{\boldsymbol{n}}\right).$$

Taking $\boldsymbol{b} = \boldsymbol{G}^{-\mathrm{T}}\hat{\boldsymbol{n}}$ and $\boldsymbol{d} = \boldsymbol{a} + \|\boldsymbol{s}\|^2\boldsymbol{G}^{-\mathrm{T}}\hat{\boldsymbol{n}}/2$, we can rewrite $\boldsymbol{C}$ more compactly as

$$\boldsymbol{C} = \boldsymbol{\delta} + \boldsymbol{d} \otimes \boldsymbol{b} + \boldsymbol{b} \otimes \boldsymbol{d}.$$

We note that we can directly write

$$\hat{\boldsymbol{v}} \cdot (\boldsymbol{C} - \boldsymbol{\delta})\hat{\boldsymbol{v}} = 2(\boldsymbol{b} \cdot \hat{\boldsymbol{v}})(\boldsymbol{d} \cdot \hat{\boldsymbol{v}}).$$

From this, we can write out the eigenvalues of $\boldsymbol{C} - \boldsymbol{\delta}$ according to the condition

$$\lambda_1 - 1 = \mu_1 \equiv \min_{\hat{\boldsymbol{v}}}[\hat{\boldsymbol{v}} \cdot (\boldsymbol{C} - \boldsymbol{\delta})\hat{\boldsymbol{v}}] \leq 0 \leq \max_{\hat{\boldsymbol{v}}}[\hat{\boldsymbol{v}} \cdot (\boldsymbol{C} - \boldsymbol{\delta})\hat{\boldsymbol{v}}] \equiv \mu_3 = \lambda_3 - 1.$$

This returns us to the claim about the eigenvalues which drove the earlier calculations.

Mallard's Law

Mallard's law states that, for a given $\boldsymbol{F}, \boldsymbol{G}$ such that

$$\boldsymbol{F} = \boldsymbol{Q}'\boldsymbol{G}\boldsymbol{R}$$

for some rotation $\boldsymbol{Q}'$ and some two-fold rotation $\boldsymbol{R}$, with the condition that

$$\boldsymbol{F}^{\mathrm{T}}\boldsymbol{F} \neq \boldsymbol{G}^{\mathrm{T}}\boldsymbol{G}$$

so that we avoid the trivial solution, then there exists some $\boldsymbol{Q}, \boldsymbol{s} \neq \boldsymbol{0}, \|\hat{\boldsymbol{n}}\|1$ such that

$$\boldsymbol{Q}\boldsymbol{F} - \boldsymbol{G} = \boldsymbol{s} \otimes \hat{\boldsymbol{n}}.$$

From this, the following results can be obtained:

$$\begin{cases} \boldsymbol{s} = 2\left(\dfrac{\boldsymbol{G}^{-\mathrm{T}}\hat{\boldsymbol{e}}}{\|\boldsymbol{G}^{-\mathrm{T}}\hat{\boldsymbol{e}}\|} - \boldsymbol{G}\hat{\boldsymbol{e}}\right) \\ \hat{\boldsymbol{n}} = \hat{\boldsymbol{e}} \end{cases} \tag{A.8a}$$

$$\begin{cases} \boldsymbol{s} = \rho\boldsymbol{G}\hat{\boldsymbol{e}} \\ \hat{\boldsymbol{n}} = \dfrac{2}{\rho}\left(\hat{\boldsymbol{e}} - \dfrac{\boldsymbol{G}^{\mathrm{T}}\boldsymbol{G}\hat{\boldsymbol{e}}}{\|\boldsymbol{G}\hat{\boldsymbol{e}}\|^2}\right). \end{cases} \tag{A.8b}$$

In the interest of space, we will only illustrate the process of arriving at Equation (A.8a), as the approach for Equation (A.8b) is very similar. We start with the two-fold rotation,

$$\boldsymbol{R} = -\boldsymbol{\delta} + 2\hat{\boldsymbol{e}} \otimes \hat{\boldsymbol{e}}.$$

If we use the rank-one connection together with what we have for $\boldsymbol{F}$ and $\boldsymbol{R}$, then

$$\boldsymbol{Q}\boldsymbol{Q}'\boldsymbol{G}\boldsymbol{R} - \boldsymbol{G} = \boldsymbol{s} \otimes \hat{\boldsymbol{n}}.$$

For the sake of compactness of notation, let us then use $\tilde{\boldsymbol{Q}} = \boldsymbol{Q}\boldsymbol{Q}'$. The right Cauchy-Green tensor in this case is nothing but

$$\boldsymbol{C} = \boldsymbol{G}^{-\mathrm{T}}\boldsymbol{F}^{\mathrm{T}}\boldsymbol{F}\boldsymbol{G}^{-1} = \boldsymbol{G}^{-\mathrm{T}}\boldsymbol{R}^{\mathrm{T}}\boldsymbol{G}^{\mathrm{T}}\boldsymbol{G}\boldsymbol{R}\boldsymbol{G}^{-1},$$

with $\det[\boldsymbol{C}] = 1$.

The results of the previous proof on the right Cauchy-Green tensor tell us that there are two solutions of interest to us. We choose to "guess" $\hat{\boldsymbol{n}} = \hat{\boldsymbol{e}}$. With this guess and reorganizing, we have

$$\tilde{\boldsymbol{Q}}(\boldsymbol{G}\boldsymbol{e}^{\perp}) = -\boldsymbol{G}\boldsymbol{e}^{\perp},$$

which holds for all $\boldsymbol{e}^{\perp}\hat{\boldsymbol{e}} = 0$. This implies that we can write out

$$\boldsymbol{G}\boldsymbol{e}^{\perp} = \boldsymbol{0} = \boldsymbol{G}^{-\mathrm{T}}\hat{\boldsymbol{e}},$$

which, in turn, implies that

$$\tilde{\boldsymbol{Q}} = -\boldsymbol{\delta} + 2\frac{\boldsymbol{G}^{-\mathrm{T}}\hat{\boldsymbol{e}} \otimes \boldsymbol{G}^{-\mathrm{T}}\hat{\boldsymbol{e}}}{\|\boldsymbol{G}^{-\mathrm{T}}\hat{\boldsymbol{e}}\|^{\boldsymbol{2}}}.$$

From this, we can conclude that

$$\boldsymbol{s} = \tilde{\boldsymbol{Q}}\boldsymbol{G}\hat{\boldsymbol{e}} - \boldsymbol{G}\hat{\boldsymbol{e}} = -\boldsymbol{G}\hat{\boldsymbol{e}} + 2\frac{\boldsymbol{G}^{-\mathrm{T}}\hat{\boldsymbol{e}}}{\|\boldsymbol{G}^{-\mathrm{T}}\hat{\boldsymbol{e}}\|^2} - \boldsymbol{G}\hat{\boldsymbol{e}} = 2\left(\frac{\boldsymbol{G}^{-\mathrm{T}}\hat{\boldsymbol{e}}}{\|\boldsymbol{G}^{-\mathrm{T}}\hat{\boldsymbol{e}}\|} - \boldsymbol{G}\hat{\boldsymbol{e}}\right),$$

which is exactly the result we sought. The procedure here could be repeated for Equation (A.8b) to give the desired results.

A.2 Twin Interface Change of Basis

In this section, we will show a quick calculation that was used for the purposes of rotating the twin simulation box to be compatible with the Cartesian formulation required in LAMMPS. We begin by considering the arbitrary normal vector $\hat{\boldsymbol{n}} =$

$[n_1, n_2, n_3]$, which observes the property that $\|\hat{\boldsymbol{n}}\| = 1$. We also suppose the existence of a shear vector $\boldsymbol{s} = [s_1, s_2, s_3]$, but orthogonality conditions require that

$$\boldsymbol{s} \cdot \hat{\boldsymbol{n}} = 0,$$

thereby placing a constraint, which we suppose to be

$$s_3 = \frac{-n_1 s_1 - n_2 s_2}{n_3}. \tag{A.9}$$

To now fully construct an orthogonal basis, we introduce a third direction

$$\boldsymbol{t} = \hat{\boldsymbol{n}} \times \boldsymbol{s}.$$

We may now then introduce the basis matrix

$$\boldsymbol{B} = \begin{bmatrix} n_1 & n_2 & n_3 \\ s_1 & s_2 & s_3 \\ t_1 & t_2 & t_3 \end{bmatrix}, \tag{A.10}$$

with s_3 being prescribed in Equation (A.9) and t_i being prescribed in Equations (A.11a)-(A.11c):

$$t_1 = -\frac{n_1 n_2 s_1}{n_3} - \frac{n_2^2 s_2}{n_3} - n_3 s_2 \tag{A.11a}$$

$$t_2 = \frac{n_1^2 s_1}{n_3} + \frac{n_1 n_s s_2}{n_3} + n_3 s_1 \tag{A.11b}$$

$$t_3 = n_1 s_2 - n_2 s_1. \tag{A.11c}$$

One can then go through and verify that

$$\begin{aligned} \boldsymbol{B} \cdot \hat{\boldsymbol{n}} &= [\mathscr{X}, 0, 0] \\ \boldsymbol{B} \cdot \boldsymbol{s} &= [0, \mathscr{Y}, 0] \\ \boldsymbol{B} \cdot \boldsymbol{t} &= [0, 0, \mathscr{Z}], \end{aligned}$$

respectively, giving us the Cartesian directions that are needed in LAMMPS, with

$$\begin{aligned} \mathscr{X} &= \|\hat{\boldsymbol{n}}\|^2 \\ \mathscr{Y} &= \frac{(n_1 s_1 + n_2 s_2)^2}{n_3^2} + s_1^2 + s_2^2 \\ \mathscr{Z} &= \frac{\|\hat{\boldsymbol{n}}\|^2 (s_1^2 (n_1^2 + n_3^2) + 2 n_1 n_2 s_1 s_2 + s_2^2 (n_2^2 + n_3^2))}{n_3^2}. \end{aligned}$$

Additional simplifications may be administered, but the idea is that use here allows for the decomposition into directions amenable for use within LAMMPS.

A.3 Treatment of Multilattices

Let us suppose now that we wish to formally discuss a multilattice. Suppose that the lattice on one side of the crystal is defined by a set of lattice vectors $\boldsymbol{e}_i$ and a shift vector $\boldsymbol{p}$, while the lattice on the other side is defined by lattice vectors $\boldsymbol{f}_i$ and a shift vector $\boldsymbol{q}$. We now need to define an expanded lattice metric

$$m_c^d = \left[\begin{array}{ccc|ccc} & \mu_a^b & & l_1^b & \cdots & l_v^b \\ \hline 0 & \cdots & 0 & & & \\ \vdots & \ddots & \vdots & & \alpha_i^j & \\ 0 & \cdots & 0 & & & \end{array}\right], \tag{A.12}$$

with

- $\mu_a^b \in \mathrm{GL}[3, \mathbb{Z}]$ being the equivalence metric from the previous formulation.
- $l_i^b \in \mathbb{Z}^3$ describing the new shift vectors.
- α_i^j being either a modification of the identity matrix with one row being replaced entirely by -1 or a regular permutation matrix.

This gives us a new set of lattice vector descriptors for the material,

$$\bar{\boldsymbol{e}}_a = \boldsymbol{f}_a = \mu_a^b \boldsymbol{e}_b \tag{A.13a}$$

$$\bar{\boldsymbol{p}}_i = \boldsymbol{q}_i = \alpha_i^j \boldsymbol{p}_j + l_i^a \boldsymbol{e}_a. \tag{A.13b}$$

Note that this m_c^d must be invertible. Recall that a matrix can be block-inverted through use of

$$\begin{bmatrix} A & B \\ C & D \end{bmatrix}^{-1} = \begin{bmatrix} \boldsymbol{A}^{-1} + \boldsymbol{A}^{-1}\boldsymbol{B}(\boldsymbol{D} - \boldsymbol{C}\boldsymbol{A}^{-1}\boldsymbol{B})^{-1}\boldsymbol{C}\boldsymbol{A}^{-1} & -\boldsymbol{A}^{-1}\boldsymbol{B}(\boldsymbol{D} - \boldsymbol{C}\boldsymbol{A}^{-1}\boldsymbol{B})^{-1} \\ -(\boldsymbol{D} - \boldsymbol{C}\boldsymbol{A}^{-1}\boldsymbol{B})^{-1}\boldsymbol{C}\boldsymbol{A}^{-1} & (\boldsymbol{D} - \boldsymbol{C}\boldsymbol{A}^{-1}\boldsymbol{B})^{-1} \end{bmatrix},$$

with $\boldsymbol{A}$ and $\boldsymbol{D} - \boldsymbol{C}\boldsymbol{A}^{-1}\boldsymbol{B}$ being nonsingular. An example of this modified equivalence metric (Equation (A.12)) for a material with lattice vectors $\boldsymbol{e}_1, \ldots, \boldsymbol{e}_3$ with one shift vector $\boldsymbol{p}$ is

$$\boldsymbol{m} = \left[\begin{array}{ccc|c} \mu_1^1 & \mu_2^1 & \mu_3^1 & l^1 \\ \mu_1^2 & \mu_2^2 & \mu_3^2 & l^2 \\ \mu_1^3 & \mu_2^3 & \mu_3^3 & l^3 \\ \hline 0 & 0 & 0 & \alpha \end{array}\right],$$

where, since we only have one shift, $\alpha = \pm 1$. Additional details can be found in Pitteri and Zanzotto [161].

A.4 Additional Background: Molecular Statics and Molecular Dynamics

The fundamental starting point for describing problems at the atomistic scale is Schrödinger's equation,

$$\mathscr{H}\psi = \mathrm{i}\hbar\frac{\partial\psi}{\partial t}, \tag{A.14}$$

with the *Hamiltonian operator*

$$\mathscr{H} = -\frac{\hbar^2}{2m}\nabla^2 + \mathsf{V}[\boldsymbol{x}], \tag{A.15}$$

m being a mass of a quantity of interest, V being an *interatomic potential*, and $\hbar$ being the normalized Planck's constant, $\hbar = \mathrm{h}/2\pi$. A typical assumption for these problem is that solutions to Equation (A.14) are separable and in an exponential form

$$\psi[\boldsymbol{x}, t] = \sum_{n=1}^{\infty}\psi_n[\boldsymbol{x}]\exp\left[-\frac{\mathrm{i}\mathsf{E}_n t}{\hbar}\right].$$

This results in the reduction of Equation (A.14) to

$$\mathscr{H}\psi_n = \mathsf{E}\psi_n, \tag{A.16}$$

with E_n being the energy levels of a system.

In a realistic system with many atoms, we have atomic nuclei located at $\boldsymbol{q}^{\mathrm{n}} = \{\boldsymbol{q}_1^{\mathrm{n}}, \ldots, \boldsymbol{q}_n^{\mathrm{n}}\}$ and corresponding electrons located at $\boldsymbol{q}^{\mathrm{e}} = \{\boldsymbol{q}_1^{\mathrm{e}}, \ldots, \boldsymbol{q}_n^{\mathrm{e}}\}$[1]. The momenta of these particles, which will enter shortly, will be denoted with $\boldsymbol{p} = m_i\dot{\boldsymbol{q}}_i$. Schrodinger's equation would then feature wavefunctions which are a function of both nuclei and electron positions, $\psi := \psi[\boldsymbol{q}^{\mathrm{e}}, \boldsymbol{q}^{\mathrm{n}}]$. We apply the *Born-Oppenheimer approximation* — which assumes that we have a separation of length scales since electrons are significantly lighter than atomic nuclei and thus move considerably faster — and separate the wavefunction into the form

$$\psi[\boldsymbol{q}^{\mathrm{e}}, \boldsymbol{q}^{\mathrm{n}}] = \psi^{\mathrm{e}}[\boldsymbol{q}^{\mathrm{e}}, \boldsymbol{q}^{\mathrm{n}}]\psi^{\mathrm{n}}[\boldsymbol{q}^{\mathrm{e}}, \boldsymbol{q}^{\mathrm{n}}]. \tag{A.17}$$

Insertion of Equation (A.17) into Equation (A.16) gives us

$$\begin{cases} \mathscr{H}^{\mathrm{e}}\psi^{\mathrm{e}}[\boldsymbol{q}^{\mathrm{e}}, \boldsymbol{q}^{\mathrm{n}}] = \mathsf{V}[\boldsymbol{q}^{\mathrm{n}}]\psi^{\mathrm{e}}[\boldsymbol{q}^{\mathrm{e}}, \boldsymbol{q}^{\mathrm{n}}] \\ \mathscr{H}^{\mathrm{e}} = \displaystyle\sum_i \frac{\|\boldsymbol{p}_i\|^2}{2m^{\mathrm{e}}} + \sum_{\alpha\neq\beta}\mathsf{V}_{\alpha\beta} + \sum_{i,j}\mathsf{V}_{ij} + \sum_{\alpha,i}\mathsf{V}_{\alpha,i} \end{cases} \tag{A.18a}$$

$$\begin{cases} \mathscr{H}^{\mathrm{n}}\psi^{\mathrm{n}}[\boldsymbol{q}^{\mathrm{n}}] = \mathsf{E}\psi_n \\ \mathscr{H}^{\mathrm{n}} = \displaystyle\sum_\alpha \frac{\|\boldsymbol{p}_\alpha\|^2}{2m_\alpha} + \mathsf{V}[\boldsymbol{q}^{\mathrm{n}}] \end{cases}. \tag{A.18b}$$

[1] For this section, we will use the superscript e to denote quantities for electrons and superscript n to denote quantities for nuclei.

We now have two separate problems at different length scales; Equation (A.18a), which describes problems at the electronic scale, is one that must then be solved using quantum mechanical techniques (e.g. density functional theory), but Equation (A.18b), which is at the scale of the nuclei, is one that can be solved using Hamiltonian mechanics.

A.5 Additional Concepts: MacroDFT

There are many additional concepts within the formulation of MacroDFT itself that one could read on. In this section, we will briefly highlight some of the key points in the formulation. You are welcome to consult any of the additional cited works — particularly [138, 139] — if you are interested in acquiring further details on the matter.

Electrostatic Energy

The electrostatic energy, Equation (4.30), leads directly to Poisson's equation, Equation (4.31). Poisson's equation arises as a direct result of finding the stationary point of this energy term. That is, if we define

$$\mathsf{E}_c[\phi] = -\frac{1}{8\pi}\int_{\mathbb{R}^3} \|\nabla\phi[\boldsymbol{x},\boldsymbol{R}]\|^2\,\mathrm{d}\boldsymbol{x} + \int_{\mathbb{R}^3}(\rho[\boldsymbol{x}]+b[\boldsymbol{x},\boldsymbol{R}])\phi[V\boldsymbol{x},\boldsymbol{R}]\,\mathrm{d}\boldsymbol{x}\,.$$

Stationarity requires that

$$\frac{\mathrm{d}}{\mathrm{d}\epsilon}[\mathsf{E}_c[\phi+\epsilon\eta]]\bigg|_{\epsilon=0} = 0$$

for some perturbation parameter ϵ and test function η. Carrying this out in indicial notation,

$$\begin{aligned}
0 &= \frac{\mathrm{d}}{\mathrm{d}\epsilon}\left[-\frac{1}{8\pi}\int_{\mathbb{R}^3}\|\nabla[\phi+\epsilon\eta]\|^2\,\mathrm{d}\boldsymbol{x} + \int_{\mathbb{R}^3}(\phi+\epsilon\eta)(\rho+b)\,\mathrm{d}\boldsymbol{x}\right]\bigg|_{\epsilon=0}\\
&= \frac{\mathrm{d}}{\mathrm{d}\epsilon}\left[-\frac{1}{8\pi}\int_{\mathbb{R}^3}\left(\frac{\partial}{\partial x_i}[\phi+\epsilon\eta]\right)^2\mathrm{d}\boldsymbol{x} + \int_{\mathbb{R}^3}(\phi+\epsilon\eta)(\rho+b)\,\mathrm{d}\boldsymbol{x}\right]\bigg|_{\epsilon=0}\\
&= -\frac{1}{8\pi}\int_{\mathbb{R}^3}\left[2\frac{\partial\phi}{\partial x_i}\frac{\partial\eta}{\partial x_i} + 2\epsilon\frac{\partial\eta}{\partial x_i}\frac{\partial\eta}{\partial x_i}\right]\mathrm{d}\boldsymbol{x} + \int_{\mathbb{R}^3}\eta(\rho+b)\,\mathrm{d}\boldsymbol{x}\,\bigg|_{\epsilon=0}.\\
&= -\frac{1}{4\pi}\int_{\mathbb{R}^3}\frac{\partial\phi}{\partial x_i}\frac{\partial\eta}{\partial x_i}\,\mathrm{d}\boldsymbol{x} + \int_{\mathbb{R}^3}\eta(\rho+b)\,\mathrm{d}\boldsymbol{x}\,.
\end{aligned}$$

We then make use of everyone's favorite theorem — divergence theorem — to rewrite

$$\begin{aligned}
\int_\Omega \frac{\partial\phi}{\partial x_i}\frac{\partial\eta}{\partial x_i}\,\mathrm{d}V &= \int_\Omega \frac{\partial}{\partial x_i}\left[\frac{\partial\phi}{\partial x_i}\eta\right]\mathrm{d}V - \int_\Omega \frac{\partial^2\phi}{\partial x_i\partial x_i}\,\mathrm{d}V\\
&= \oint_{\partial\Omega}\frac{\partial\phi}{\partial x_i}\eta\,\mathrm{d}A - \int_\Omega\frac{\partial^2\phi}{\partial x_i\partial x_i}\,\mathrm{d}V\,.
\end{aligned}$$

Picking our test function η to vanish on the boundary, we then have that

$$0 = \int_{\mathbb{R}^3} \eta \left(\frac{1}{4\pi} \frac{\partial^2 \phi}{\partial x_i \partial x_i} + \rho + b \right) \mathrm{d}\boldsymbol{x} \, .$$

Since this must hold everywhere, we thus have the result that

$$-\frac{1}{4\pi} \nabla^2 \phi = \rho + b,$$

thus recovering Poisson's equation.

Coarse Graining

One of the ways by which MacroDFT is able to represent enormous systems is through the use of coarse graining. The concept behind this is that an entire sample does not need to be fully resolved if a defect is localized. This is the case with many of the studies to which MacroDFT is applied, as defects tend to be localized with respect to the remainder of the sample; most of the rest of the sample is just the reference, perfect crystal whose solution is well known a priori. Consequently, distribution of the atomic and electronic mesh so that a full resolution is achieved near the defect of interest — whether it is a vacancy or, in our case, a twin plane — and then reducing the committed resources further away from the defect allows for the representative simulation of enormous systems.

A.6 MacroDFT Size Effects

As a final step, an investigation is conducted on the effect of changing the cell size for one particular twin - the tension twin. In this case, the $(10\bar{1}2)$ twin is chosen for study. Both the number of unit cells of width in the simulation and the thickness of the twin region are varied; for each of the changes, $E^{\mathrm{tw}}/\mathrm{atom}$ is calculated. This value is then plotted against the thickness of the twin simulation in Figure A.1. Different curves representing the varying width of the simulation in the twin plane are also shown. Figure A.1 confirms that our implementation for the energy in MacroDFT is converging reasonably accurately.

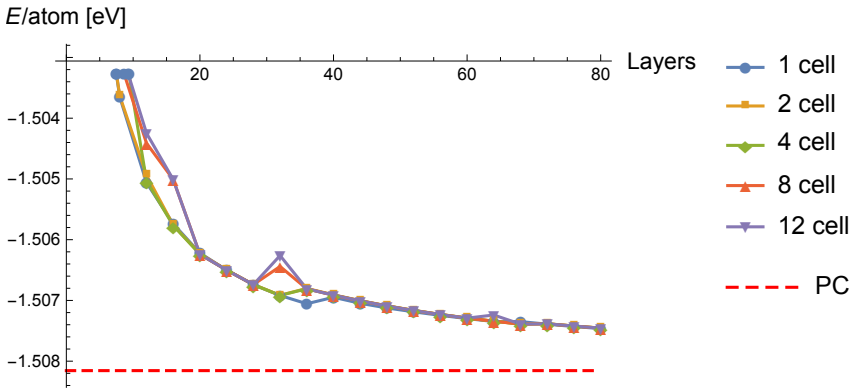

Figure A.1: Plot of the energy per atom in eV as a function of the thickness of the twin region for the $(10\bar{1}2)$ classical variant. The different curves show energy results as the width of the computational cell is increased. The dashed line represents the cohesive energy E_0^{pc}.

INDEX

A
alloys, 11
attempt frequency, 55

B
BCC, 17
body-centered cubic, 17
Born-Oppenheimer approximation, 124
Bravais lattice, 17

C
cohesive energy, 51
compound twin, 22
compression twin, 7
critical resolved shear stress, 89

D
deformation gradient, 18
density functional theory, 59
    Kohn-Sham, 60
ductility, 4

E
EAM potential, 49
EBSD, 8
elastic domain, 89
electron backscatter diffraction, 8
embedded atom method potential, 49
embedding function, 49

F
face-centered cubic, 17
FCC, 17

H
Hamilton's equations of motion, 48
Hamiltonian operator, 124

HCP, 18
hexagonal close-packed, 18

I
interatomic potential, 48, 124

K
Kohn-Sham density functional theory, 60

L
lattice equivalence metric, 20

M
MEAM, 50
modified embedded atom method, 50
molecular dynamics, 48
molecular statics, 48
multilattice, 17

N
NEB, 52
non-Bravais lattice, 17
nudged elastic band, 52

P
perfect crystal, 22
plastic deformation, 5

R
reciprocal lattice, 19
replicas, 52

S
shifts, 18
shuffling, 25

T
TEM, 9
tension twin, 7
transmission electron microscopy, 9

twin, 6, 21
    compound, 22
    type I, 22
    type II, 22
twin plane, 22
twinned crystal, 22
twinning equation, 23
twinning shear, 22
type I twin, 22
type II twin, 22

V
virial stress, 87

Y
yield stress, 89
yield surface, 89